Study of Baryon Number Transport using different LHC Energies and Assembly of 2S Module for the CMS Tracker Phase-2 Upgrade

by

Hafiz Inamullah

A thesis submitted in partial fulfillment of the requirements for the degree of

Master of Science

Department of Physics

Quaid-i-Azam Univeristy

Study of Baryon Number Transport using different LHC Energies and Assembly of 2S Module for the CMS Tracker Phase-2 Upgrade

by

Hafiz Inamullah

Department of Physics

Quaid-i-Azam University Islamabad, Pakistan

(2021-2023)

Study of Baryon Number Transport using different LHC Energies and Assembly of 2S Module for the CMS Tracker Phase-2 Upgrade

by

Hafiz Inamullah

Department of Physics

Quaid-i-Azam University Islamabad, Pakistan

(2021-2023)

A THESIS SUBMITTED IN PARTIAL FULFILLMENT OF THE REQUIREMENTS
FOR THE DEGREE OF MASTERS OF PHILOSOPHY IN PHYSICS AT THE
QUAID-I-AZAM UNIVERSITY, ISLAMABAD 45320, PAKISTAN. SEPTEMBER,2023.

RESEARCH COMPLETION CERTIFICATE

Certified that the research work contained in the thesis titled Study of Baryon Number Transport using different LHC Energies and Assembly of 2S Module for has been carried out and completed by Mr. Hafiz Inamullah Roll No. 02182113032 under my supervision.

Supervised by:

_____

Dr.Shamona Fawad Qazi
Department of Physics
Quaid-i-Azam University Islamabad

Submitted through:

_____

Prof. Dr. Kashif Sabeeh
Chairperson
Department of Physics
Quaid-i-Azam University Islamabad

DEDICATION

To my all Respected Teachers,
Especially
My 1st and foremost Teachers
My Mother
and
My Father.

Contents

List of Figures

Abstract

In the months of November and December 2009, the Large Hadron Collider (LHC) produced the first p-p collisions. Since then, all LHC experiments have collected a sizable data sample. An increasing number of unusual particles and events can be examined thanks to this event collection. Despite being mainly intended to examine heavy ion collisions, the **ALICE experiment** contains a robust program for studying proton-proton interactions.

In this dissertation, through the findings from the examination of p-p collisions at various LHC energies ($\sqrt{s}$ = 900 GeV, 200 GeV, 2.76 TeV, 7 TeV and 13 TeV) are given. Focus is on the antibaryon-to-baryon ratio research because it is crucial for understanding how baryon numbers are transported and because it can both reveal the baryon number's carrier and provide details about the structure of the baryon itself. Specifically, the $\frac{\overline{p}}{p}$, $\frac{\overline{\Lambda}}{\Lambda}$ and $\frac{\overline{\Xi}^+}{\Xi}$ rapidity, and transverse momentum dependency. Results from simulations using the DPMJET-III, Pythia8, EPOS1.99, and EPOS-LHC models on the excitation function of anti-baryon to baryon ratios ($\frac{\overline{p}}{p}$, $\frac{\overline{\Lambda}}{\Lambda}$ and $\frac{\overline{\Xi}^+}{\Xi}$) in pp collisions at $\sqrt{s}$= 0.9 TeV, 2.76 TeV, and 7 TeV. Model simulation results are then compared to **ALICE** experimental results. These ratios were also computed at 13 TeV, at which LHC is taking high luminosity Run-II data in pp collisions, to study their predictions.

One of the largest accelerators in the world is the Large Hadron Collider(LHC). Hadrons are accelerated toward the speed of light. The whole **CMS** outer tracker will be replaced as part of phase-2 upgrade for LHC high luminosity. The silicon-based strip detector is the outside component of the **CMS** outer-tracker, while the silicon-based pixel detector is the inside part. With a 200 m^2 active area, it is the biggest silicon tracker yet constructed. Over 13,000 components will make up the new silicon outer tracker, comprising 7608 2S modules (two silicon strip sensors) and 5592 PS modules (one pixel and one strip sensor).

The replacement of the whole tracker is part of the CMS Phase-2 upgrade. This research examines the 2S module, a key component of high-energy physics investigations. Front-end Application-Specific Integrated Circuits (ASICs) with correlation logic read two strip sensors in the 2S module. A cooling structure supports and integrates 10×10 cm^2 sensors with 5 cm long strips and a 90 μm spacing. Wire bonding links sensors to readout hybrids with eight CMS Binary Chips (CBCs) and a data concentrator chip that uses less than 2 watts. This research contributes to the understanding and optimization of 2S modules in the context of high-energy physics experiments.

Acknowledgments

I have no words to express my gratitude to Allah Almighty, the Greatest of All, who is the ultimate keeper of knowledge riches. He bestowed upon me sufficient understanding, opened my eyes, and directed me to a point where I did something substantial. From the bottom of our hearts, we honour and adore the Holy Prophet Muhammad (PBUH), who brought humanity out of the darkness of ignorance, emphasised the need of pursuing knowledge, and instilled in his Ummah a strong desire to study.

I'd want to express my heartfelt gratitude to my mentor and supervisor Dr.Shamona Fawad Qazi for their valuable time, professional assistance and advice in my research effort. He was the one who encouraged me to pursue a career in Experimental particle physics. Additionally, I would like to express my gratitude to Dr Ishfaq Ahmad, Mr. Imran Malik at **NCP**, who greatly assisted me with my research.

I owe a big debt of appreciation to my parents especially my mother, who supported me in doing this despite the fact that he had no knowledge of my degree and could support me and pray for me everywhere. My father, who is no longer alive. Allah bestows upon him a high position in janah and he also supports me in my becheler degree which is devoted to my father. I'd want to express my gratitude to my siblings and friends for their spiritual support and positive motivation.

I also appreciate the constructive debates, recommendations, and critiques from my coworkers. I'd like to thank my university buddy M.Irfan,M.Arsalan for his research-related recommendations and great chats. Finally, a particular thanks to my closest friends M.Awais, Shakir, and others who assisted me in my research work, either directly or indirectly.

Contents

List of Figures

List of Tables

Chapter 1

Introduction

A theoretical framework developed to explain the universe at its most fundamental level is the Standard Model (SM) of particle physics [1, 2, 3]. Since the 1960s, we have gained a greater understanding of the subatomic world. Scientists discovered that nucleons (protons and neutrons) contain additional tiny particles known as quarks. There are three generations having six different types of quarks, each one consisting of two quarks. These quarks are up (u), down (d), charm (c), strange (s), top (t), and bottom (t) . There are also six types of leptons, divided into three generations, each one having two leptons. The electron, muon, tau, and their corresponding neutrinos make up the six leptons. While leptons(e, μ, τ) are charged, neutrinos (ν) are chargeless. Nature has four primary forces. The existence of gravity is well known. However ,it is not clear how gravitational force works at the quantum level. Therefore, it is not included in SM. Also, there are three other forces: electromagnetic force, weak force, and strong force. A gauge boson acts as a mediating particle for each of these forces. Strong and electromagnetic forces are mediated by gluons (g) and photons (Υ), respectively. Weak force is mediated by $W^{\pm}$ and Z boson. There is a difference between particles with integral spins (gauge bosons) and particles with half integral spins (quarks and leptons).

The fundamental characteristics of matter and their composition are analysed by particle physics. In particle physics, the tiniest particles are usually investigated along with the fundamental interactions that explain their behavior. There are three types of irreducible particles: leptons, quarks, and bosons (including gauge bosons and the higgs boson). There is currently a dominant theory that explains the general framework of fundamental particles and their interactions. It is called the Standard Model.

In chapter 3, we will discuss about a Baryon number, carrier of Baryon number and annhilation of Baryon number. In Chapter 4, using simulations from the DPMJET-III, Pythia 8, and EPOS-LHC models, we present information on the excitation function of anti-

baryon to baryon ratios ($\frac{\bar{p}}{p}$, $\frac{\bar{\Lambda}}{\Lambda}$ and $\frac{\bar{\Xi}}{\Xi}$) in pp collisions at $\sqrt{s}$ = 0.9 TeV, 2.76 TeV,7 TeV and 200 GeV. Next, the calculated ratios from model simulations are contrasted with the experimental data provided by the ALICE experiment. We also computed these ratios at $\sqrt{s}$ = 13 TeV, the energy at which the LHC is collecting high luminosity Run-III data in pp collisions, to explore the predictions of these theories. The anti-baryon to baryon ratio plays a significant role in analyzing baryon number transfer methods. By using these ratios, it is possible to identify baryon number carriers as well as extract information about the baryon number structure information. This ratio is independent of both p_T and rapidity (y). However, the ratios extracted from DPMJET-III model closely match the data at all energies, showing good agreement between model simulations and data. DPMJET-III ratios closely match the data at all energies. The ratios converge to unity for various model predictions between 0.9 and 13 TeV. The convergence also indicates that the anti-baryon to baryon ratio follows the mass hierarchy, meaning that the specie in which more strange quarks $\left(\frac{\bar{\Lambda}}{\Lambda} and \frac{\bar{\Xi}}{\Xi}\right)$ are present approaches unity faster than specie with fewer strange quarks ($\frac{\bar{p}}{p}$). By increasing the strangeness content, the $\frac{\bar{B}}{B}$ ratio increases. As energy increases, the $\frac{\bar{B}}{B}$ ratio approaches unity more rapidly. Using model simulations, we additionally compute the asymmetry $A \equiv \frac{N_P - N_{\bar{P}}}{N_P + N_{\bar{P}}}$ for protons. Asymmetry decreases with increasing energy from 0.9 to 7 TeV for all energies.Asymmetry predictions at $\sqrt{s}$= 13 TeV are consistent with this asymmetry trend and will help to constrain model calculations once Run-III data for LHC are available.

Accelerators with extremely high efficiency are used for most experiments. The researchers study the interactions between known particles and search for unknown particles (new particles) that may exist. One of the world's most effective particle accelerators, the Large Hadron Collider (LHC) is the largest and the most powerful one in the world. Particles are accelerated in opposite directions close to light's speed. The first proton-proton collisions were produced by the Large Hadron Collider (LHC) between November and December 2009. All LHC experiments have since collected a sizable data sample. With the help of this event sample, we can learn more and investigate unusual particles and occurrences. With flexibility in mind, the CMS (Compact Muon Solenoid) experiment has a robust proton-proton physics program in addition to its principal purpose in high-energy physics research. The amazing capabilities of CMS in vertexing and particle identification (PID) procedures, as well as its excellent precision in momentum measurement, are noteworthy features.

In Chapter 5, we will discuss LHC and CMS experiments, the Alice experiment and LHC detector magnetic system along with LHC physics. The ALICE experiment at the LHC contributes to proton–proton physics in several ways.

The CMS experiment, along with the ATLAS experiment, led to the discovery of the

Higgs boson in 2012. The CMS consists of a number of subdetectors. In CMS, the tracking detector, also known as the tracker, plays an important role. Around 15,000 silicon modules allow it to accurately measure charged particles' paths near the interaction point. Most of the information about the LHC and CMS experiment can be found in Chapter 3. The Alice experiment can also be found in Chapter 3. There are significant details about silicon pixel and strip trackers, tracker layout after upgrading, radiation environment, and outer tracker 2S modules assembly for the CMS tracker phase-2 upgrade in chapter 7.

Over the last ten years, the accelerator chain at CERN's Large Hadron Collider (LHC) has experienced constant development. The whole tracker detector will be changed as part of the CMS experiment Phase-2 Upgrade to make it ready for the High Luminosity LHC. In front of it, something will be completed. The new Outer Tracker will consist of around 13,000 silicon sensor units Of these, 7608 will be "2S modules" made up of two silicon strip sensors installed in tandem while 5592 will be "PS modules" made up of a single module including a strip sensor and a pixel. Chapter 5 gives , there is a brief discussion about the assembly of the 2S module.

The goal of chapter 7 is to introduce the assembly of the 2S module. The construction of the 2S module at the National Center for Physics (NCP) is thoroughly explained. Following that, the 2S module an essential part of high-energy physics studies, is the focus of this study. Two strip sensors in the 2S module are read by front-end ASICs equipped with correlation logic. 10×10 cm^2 sensors with 5 cm long strips and 90 μm spacing are supported and integrated into a cooling framework. Connecting sensors to low-power readout hybrids through wire bonding, the latter comprises eight CMS Binary Chips (CBCs) and a Data Concentrator chip. This study aids in the elucidation and improvement of 2S modules for use in high-energy physics studies. In Chapter 8, you'll get a conclusion.

Chapter 2

The Standard Model

The Standard Model (SM) of particle physics describes the basic building blocks of matter and the fundamental forces that determine their interactions, as well as their interactions with each other. In addition to the leptons and quarks that make up the SM particles. There are gauge bosons that mediate the fundamental forces, as our discussion below will show.

2.1 Theoretical Aspects of Particle Physics

This chapter begins with the brief overview of fundamental particles in nature and interactions between them through a short description of the Standard Model [3], followed by information about the LHC. As the understanding of the particle physics progresses with the discovery of the Higgs boson in 2012 [2], there are still unanswered questions. The Standard Model has shortcomings, for example it does not describe the gravity or masses of neutrinos. Another problem with the Standard Model is that it represents only about 15% of the matter. Furthermore, if we look at the energy content of the universe, the Standard Model explains about 4% of that the rest being dark matter(24%) and dark energy (72%). HGTD (High-Granularity Timing Detector) is a subdetector within the ATLAS experiment designed to precisely measure the timing of particles produced in high-energy proton-proton collisions and LGAD (Low Gain Avalanche Diode) are a type of silicon photodetector with a unique design that allows them to provide extremely fast timing resolution. To further test the Standard Model and to look for the solutions to its problems, the ATLAS experiment and motivation of why HGTD is required. For this purpose, the detail information of HGTD and silicon LGAD sensors will also be presented looking for new solutions in physics.
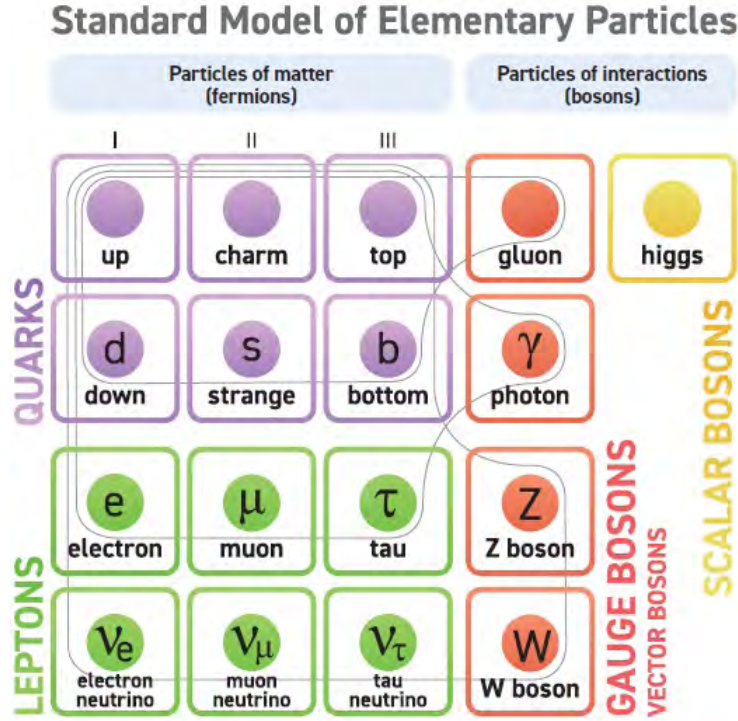
Figure 2.1.1: Elementary particles in standard model containing three genera- tions of fermions, gauge bosons and on the top right corner Higgs Boson[2].

As Figure 2.1.1 shows, the elementary particles in standard model can be divided into two groups; the fermions and bosons. All matter consists of fermions. The bosons are the force carriers. These particles interact with each other and built up everything that now exits in our universe including stars and planets.

2.1.1 Fermions

The Standard Model of particle physics includes six types of quarks and six types of leptons. Leptons and fermions are spin half particles and are referred to as flavours, which are therefore called fermions. According to spin-statistical theorem, fermions obey pauli's exclusion principle. Every fermion has an antiparticle with the same mass but opposite charge. These elementary particles with electromagnetic charges and masses can be seen in Figure 2.1.1. Each fermion belongs to one of the three generations that differ from each other only by mass which increases in each generation. The lightest flavours being in the first generation. Each of these generations contains one up-type quark having positive charge, one down type quark with negative charge, one charged lepton and a neutrino. If no law of conservation forbid then the heavier particles i.e, second and third generation particles will tend to decay to lighter ones (first generation). Therefore, any stable material is generally composed of first

5

generation particles; up quarks(u), down quarks(d), and electron(e). Just as particles can have electromagnetic charge, quarks also carry a color charge. Although the quark can have color charge of red, green or blue, only colorless combination may exist freely. A colorless particle could be created by the combination of three quarks with each one of these colors. This colorless combination is called baryon, or combination of a quark with anti-quark each with one of these three colors and anticolors called meson. Baryons and mesons together are called hadrons, for example protons and neutrons are included in the family of baryons which are composed of (uud) and (udd) quarks respectively. In meson family, pions are the lightest one containing a quark and an anti-quark. They can be neutral ($u\bar{u}$,$d\bar{d}$) ,negatively charge($d\bar{u}$) or a positively charge $u\bar{d}$[4].

2.1.2 Bosons

The Standard Model comprises gauge bosons, which serve as intermediaries or carriers of the fundamental forces, facilitating interactions between particles. These gauge bosons play a crucial role in mediating three of the four fundamental forces: electromagnetism, the weak force, and the strong force. Photons, for instance, act as the mediators of the electromagnetic force, allowing for interactions among electrically charged particles. This force is responsible for the existence of phenomena like light, electric fields, and magnetic fields. The weak force, which affects all fermions, is responsible for altering the flavor of quarks. This force is mediated by $W^{\pm}$ and Z bosons. The strong force, on the other hand, governs interactions between particles with color charges and is mediated by gluons. Gluons play a pivotal role in binding these particles together to form color-neutral particles called hadrons. It's worth noting that gluons themselves carry color charges, enabling them to interact with each other. The most recent addition to the Standard Model is the Higgs boson. Unlike other gauge bosons, the Higgs boson lacks electric or color charges and is not associated with any of the fundamental forces. Instead, the Higgs boson is a manifestation of the Higgs field, which is responsible for imparting mass to other particles through the Brout-Englert-Higgs mechanism [5].

2.2 Fundamental Interactions

The electromagnetic, weak, strong, and gravitational forces are nature's four basic forces. Strong, electromagnetic, weak, and gravitational interactions all have relative strengths of , 10^{-2}, 10^{-13}, and 10^{-42}, respectively. The main characteristics of four basic forces are summarized in Table 1.1.

Force	Strength	Theory	Mediator
Strong	10	Chromodynamics	Gluon (g)
Electromagnetic	10^{-2}	Electrodynamics	Photon (γ)
Weak	10^{-13}	Flavordynamics	W^+, W^-, Z^0
Gravitational	10^{-42}	Geometrodynamics	Gravitons (G)

Table 2.2.1: Four fundamental forces of nature[6].

The physics concept known as geometrodynamics explains gravitational force in terms of geometry and space time gravitational force. A graviton is the gravitational force mediator. Most individuals believe that gravity is too weak to clearly illustrate its function in the elementary particle physics.

The QED theory provides an explanation for electromagnetic interactions. The photon serves as a mediator in QED. Figure 2.2.1 shows that, when an electron goes through electromagnetic interaction, it emits or
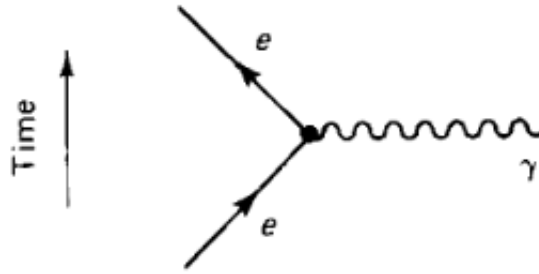
Figure 2.2.1: QED interaction

absorbs the photon and then leaves. Figure 2.2.2's top left graphic depicts the photon exchange mediated coulomb repulsion of two electrons. This process is known as Moller scattering.

$$e^- + e^- \rightarrow e^- + e^-$$

Figure 2.2.2's top right graphic illustrates how the exchange of photons mediates the Coulomb attraction of electrons and positrons. This process is known as Bhabha scattering.

$$e^+ + e^- \rightarrow e^- + e^+$$

In Figure 2.2.2 , the bottom diagrams show the Compton scattering, which is the scattering of a photon with an electron by losing some parts of its energy.

$$e^+ + \gamma \rightarrow \gamma + e^+$$

7

Quantum chromodynamics is the name of the physics theory that explains strong interactions. In strong interaction, a gluon serves as the intermediary between two quarks. Bicolor, sometimes known as color and anticolor, is carried by gluon. Throughout the process of $q \to q + g$ the quark's color may change. For instance, through conversion, a blue up quark may become a red up quark. As seen in Figure 2.2.3(left), color (like charge) is always preserved, therefore the gluon must take away the difference, in this instance, one unit of blueness and minus one unit of redness.

Quarks can only exist in three colors: "red" (r), "blue" (b), and "green" (g). There are $3 \times \bar{3} = 9$ options available, however only 8 possible gluon types can exist due to symmetry rules.
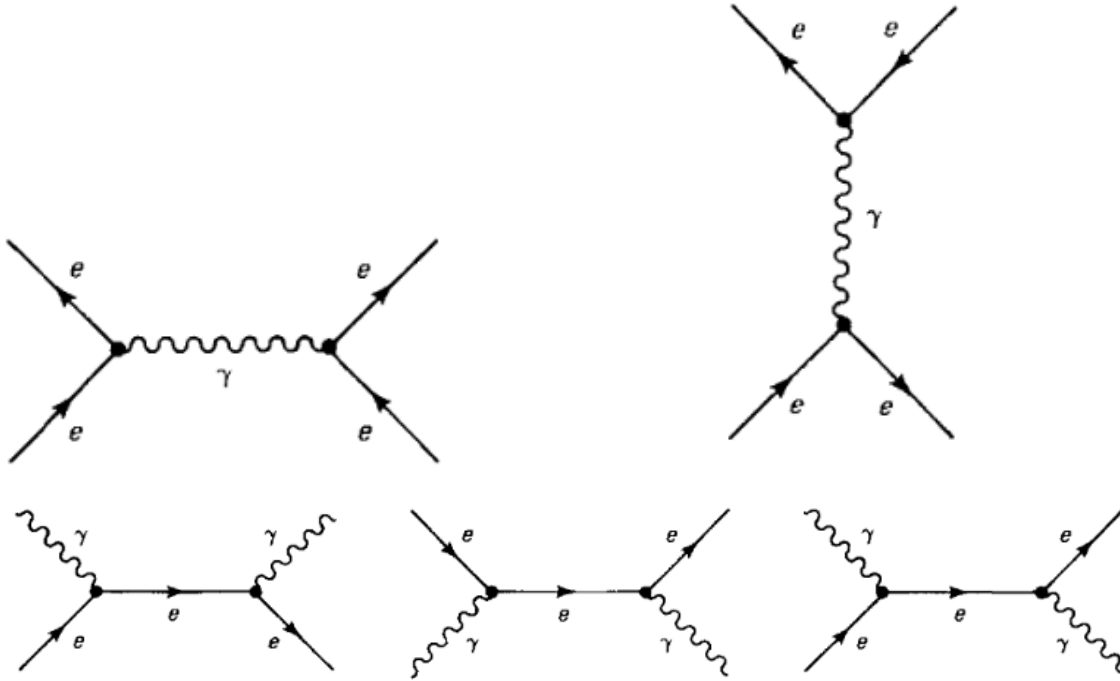
Figure 2.2.2: The upper left diagram shows Bhabha scattering, upper right diagram show Bhabba scattering and below ones shows Compton scattering.

Gluons can link with other gluons because, unlike photons, gluons have a color component. Gluon gluon interaction is seen in the center and right side diagrams of Figure 2.2.3.

The critical parameter "a" in the context is an important aspect in understanding the behaviour of the strong force, as described by Quantum Chromodynamics (QCD). The value of "a" is given by,

a = 2f -11n

where f is number of flavour and n is colour, f and n are fixed so a is also fixed. Since f=6

and n=3 in the Standard Model, a=-21. The decline in QCD coupling at a close distance is the cause of asymptotic freedom.

Flavourdynamics is the name of the physics theory that explains weak nuclear interaction. In a weak interaction, CP, Parity, and Strangeness are not preserved. There are two kinds of weak interactions: charged mediated by W bosons and neutral mediated by Z bosons. Weak interactions involve all quarks and leptons.

The left Feynman diagram in Figure 2.2.4 illustrates how the emission of the W^+ boson transforms a negative lepton into a matching neutrino.
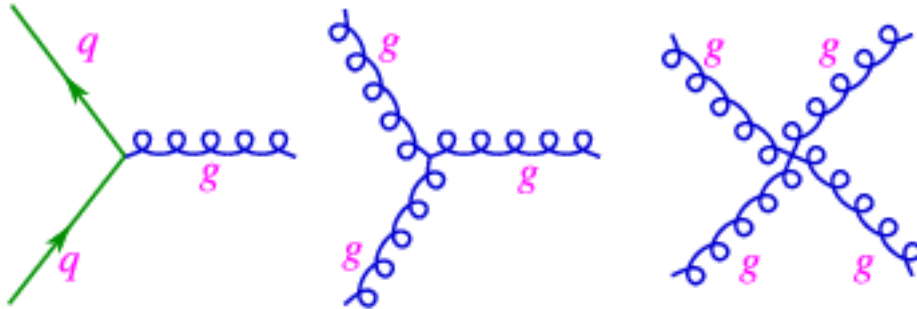
Figure 2.2.3: The left diagram shows the interaction of quarks in QCD , middle and right diagrams show gluon gluon interaction[7].

$\ell^- + W^+ \to \nu_\ell$

The right Feynman diagram in Figure 2.2.4 is shown for $e^- + \nu_e \to e^- + v_e$
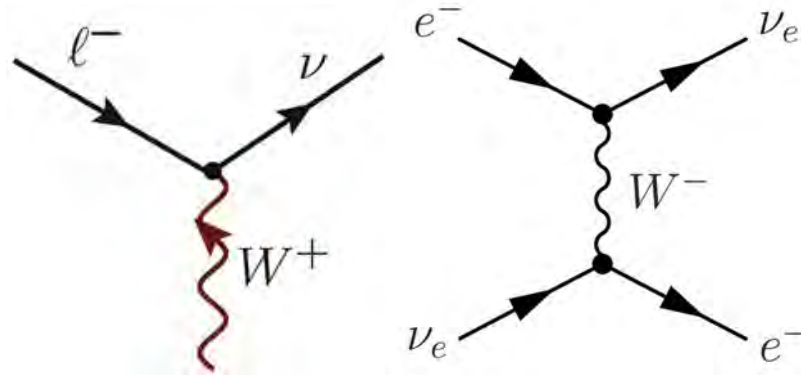
Figure 2.2.4: Feynmann diagrams for weak interaction through W^- boson[8].

The left side graph in Figure 2.2.5 illustrates how a lepton and anti-lepton combine to form a Z-boson.

$\nu_\mu + e^- \longrightarrow \nu_\mu + e^+$

The right-side schematic in Figure 2.2.5 shows the following procedure:

9

$(\nu_\mu + \overline{\nu_\mu} \longrightarrow e^- + e^+)$

Weak interactions are another way through which quarks may interact. The Feynmann diagram of the basic charged vetex is shown in Figure 2.2.6.

Figure 2.2.6 shows how the emission of a W^-boson changes a $\frac{-1}{3}$ charged quark into a $\frac{+2}{3}$ charged quark.
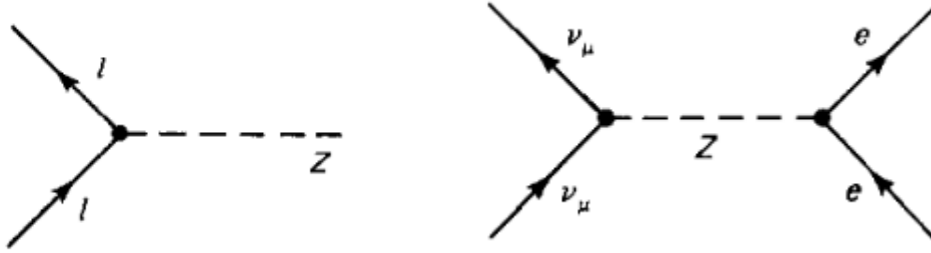
Figure 2.2.5: Feynmann diagrams for weak interaction involving Z boson.

The Feyman diagram for the semileptonic process ($d + \nu_e \longrightarrow u + e$),
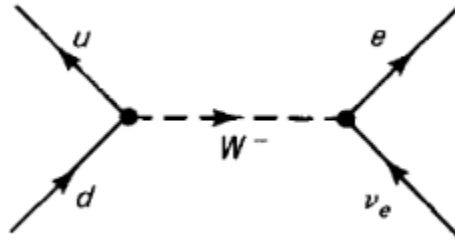
Figure 2.2.6: Semileptonic process for W^-mediater.

The Feyman daigram for the process ($\nu_\mu + p \longrightarrow \nu_\mu + p$) as shown in Figure 2.2.7.
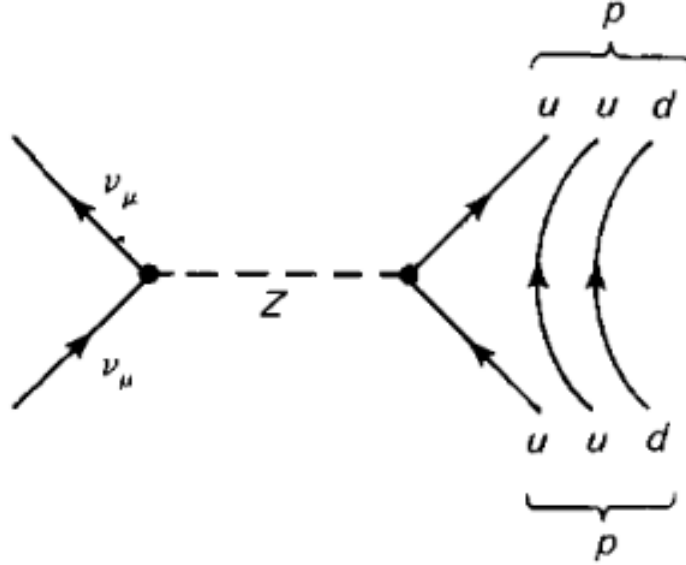
Figure 2.2.7: Semileptonic process for Z mediator.

2.2.1 Unification of Forces

To combine the four fundamental forces into a single, universal force that existed at least in the universe's early stages has been a goal of physicists for many years. The reason for this is that four forces are too many for a universal theory. The forces we see now are only outward representations of one fundamental force in the primordial picture. However, the presence of all these many forces today is essential. Instead of galaxies, stars, and planets, there may just be one huge black hole if gravity were stronger. Atoms would dissolve and there wouldn't be any atoms, molecules, matter, chemistry or life, if electromagnetic forces and the strong nuclear force were out of equilibrium. The gradual burning of stars like our sun and supernova explosions, which produce all elements heavier than iron and rely on the intensity of neutrino interaction, would not be feasible without nuclear forces.

The four basic forces are explained by four separate ideas, which is not entirely adequate. Quantum Electrodynamics (QED), a well-known quantum field theory, explains the electromagnetic interaction quite effectively. Quantum Chromo dynamics (QCD) is one such theory that focuses on strong interactions. Quantum Flavour dynamics explains the weak interaction. Einstein's general theory of relativity serves as the definition of the gravitational interaction since it lacks a well-established field theory. Glashow, Weinberg, and Salam succeeded in combining weak and electromagnetic forces into one fundamental phenomenon. Maxwell demonstrated that electricity and magnetism were manifestations of the same, single basic phenomenon [9]. Figure 2.2.8 shows the variation of strength of each of the four

force with energy.
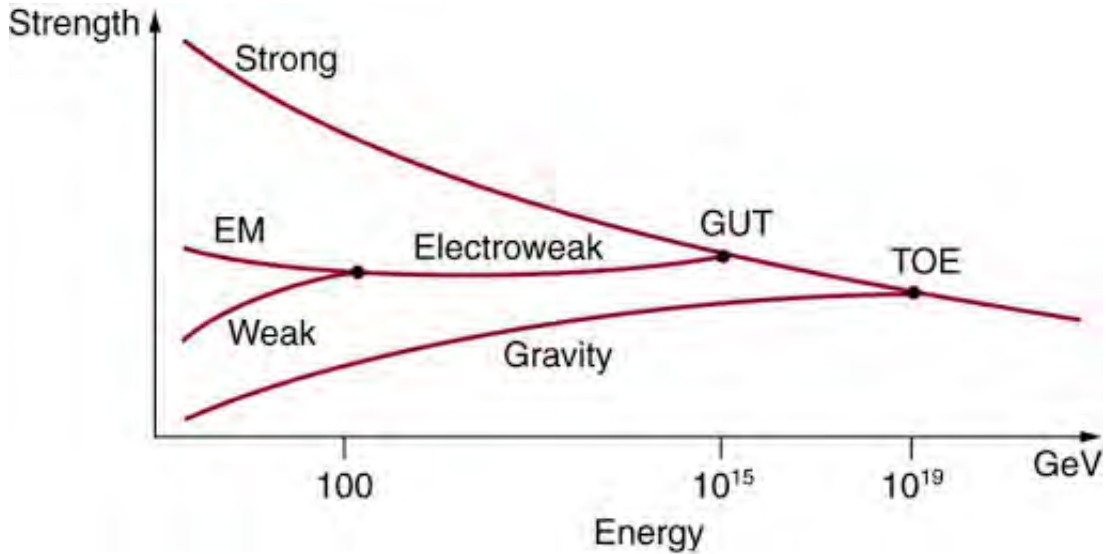
Figure 2.2.8: Unification of the fundamental forces [9].

These strengths are quite different at the standard energy level or temperature ($\frac{1}{40}$ GeV or 300 K, respectively). The weak force becomes just as strong as the electromagnetic force during high energy particle collisions. The fundamental equations controlling the two interactions are symmetric in the manner in which they take place, and all mediating particles really have masses of zero. However, if the energy level decreases or the temperature decreases, the symmetry is broken and the exchange particles or field quanta break into four distinct gauge bosons, including the heavy $W^{\pm}$ and Z^0 (each weighing 91 GeV) and the massless photon (γ). Spontaneous symmetry breakdown is what this is [10]. The $W^{\pm}$ and Z^0 bosons are ineffective at ambient temperature or at typical energy levels. However, at high energies of around 3000 GeV or more, the distinction between the massless γ, $W^{\pm}$ and Z^0 bosons vanishes, and they all behave similarly [10].

2.2.2   The Higgs Mechanism

Electroweak theory is insufficient to describe the process by which a W or Z boson gains mass. The fact that weak bosons gain mass while photon does not implies the existence of at least one additional virtual particle that bears the force, that violates this symmetry at low energies. The Higgs boson is this hypothetical particle and the whole process is referred to as the Higgs mechanism [11].

We need to remember that mass is an expression of inertia in order to understand how particles acquire mass. If the higgs field permeates the whole universe as it cools, it will

serve as a pull on every particle that travels through it. The drag is influenced by a particle's ability to interact with the Higgs field. Because of the drag's resemblance to inertia, formerly massless particles now seem to have some amount of mass. All of this happens as a result of what is known as spontaneous symmetry breakdown [11]. When a system that is subject to global symmetrical rules transitions to its lowest energy state, spontaneous symmetry breakdown happens. This is shown in Figure 2.2.9 by the example of a ball in a bowl that rises in the middle until it must fall in one of two directions.The lowest energy state of the higgs field, which occupies all of space like all other fields but does not give the photon its mass, falls in the same direction as the W and Z bosons.
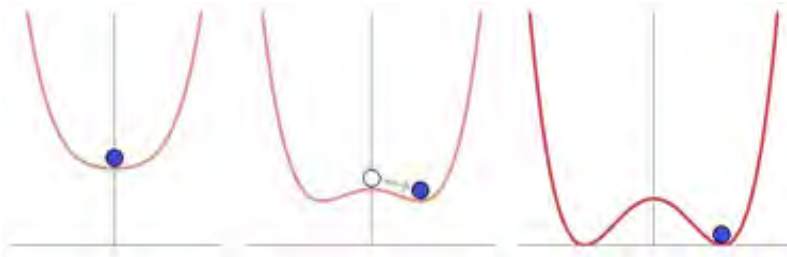
Figure 2.2.9: Illustration of spontaneous symmetry breaking [9].

The bound states of quarks are called hadrons. Given that the strong force is what binds the quarks together, the word "hadrons" refers to strongly interacting or bonded particles. Hadrons fall within one of two kinds;

- Mesons

- Baryons

Mesons

Mesons are middle weighted particles because they are heavier than leptons but lighter than baryons. A quark and an antiquark $(q\bar{q})$ pair make up a meson. Pions $(\pi^{\pm}, \pi^0)$, kaons (K^0), and other particles are examples of mesons.

Baryons

Since baryons are heavier than leptons and mesons, their name implies "heavy weighted." A baryon is made up of three quarks (qqq). Protons (uud), neutrons (udd), and other elementary particles are examples of baryons.

2.3 Units in Elementary Particle Physics

Due to their tiny size, elementary particles are difficult to measure using conventional mechanical units like grams, centimetres, joules, ergs, etc.
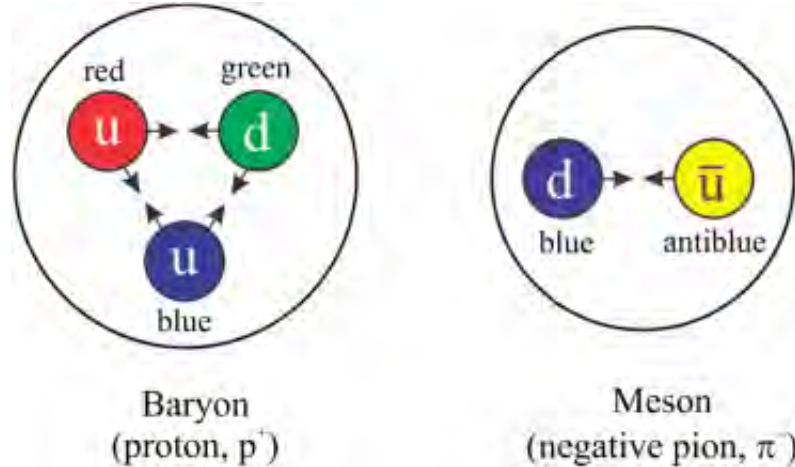
Figure 2.3.1: Quarks composition of baryons and mesons.

Additionally, special theory of relativity and quantum mechanics are all we have in fundamental particle physics. The decreased Plank's constant ($\hbar$= 1.05457 10^{-34} js), which occurs in almost all equations of quantum physics, and the speed of light (c), both appear in virtually all equations of relativity. Thus, we use relativistic quantum mechanics to experiment with particle interactions. More symbols are introduced to us, and the c's and $\hbar's$ start to annoy us. Therefore, we just set them to unity and disregard writing them, i.e., c = $\hbar$= 1. The term "system of natural units" refers to this mathematical framework. Following completion of the computations and discovery of the findings, the c's and $\hbar's$ are once again used to compute the numerical values.

The electron-volt (eV) is the standard unit of energy in basic particle physics. A free electron gains one electron-volt of energy as it accelerates across a one volt potential difference. Kilo electronvolts (1 KeV = 10^3 eV), Mega electronvolts (1 M eV = 10^6 eV), Tera electronvolts (1 T eV = 10^6eV), and Giga electronvolts (1 GeV = 10^{12} eV) are higher units. Using the energy-momentum relationship proposed by Einstein, we have,

$$E^2 = p^2c^2 + m^2c^4 \tag{2.3.1}$$

When the particle is at rest, we have p= 0. The above equation then becomes,

$$E = mc^2$$

$$m = \frac{E}{c^2} \tag{2.3.2}$$

and when the body is moving with the speed of light which implies that $m = 0$, and the momentum then becomes,

$$mc = \frac{E}{c} \tag{2.3.3}$$

thus mass and momentum can be measured in the units of energy. Also from the displacement-momentum uncertainty relation,

$$\Delta x \Delta p \geq \hbar$$

$$\Delta x \geq \frac{\hbar}{\Delta P} = \frac{\hbar}{mc}$$

$$\Delta x = \frac{\hbar c}{mc^2} \tag{2.3.4}$$

And from the energy-momentum uncertainty relation,

$$\Delta E . \Delta t \geq \hbar$$

$$\Delta t \geq \frac{\hbar}{E} = \frac{\hbar}{mc^2}$$

$$\Delta t \approx \frac{\hbar}{mc^2} \tag{2.3.5}$$

Taking the unit of energy as GeV, we specify, Unit of mass:

$$\frac{mc^2}{c^2} = \frac{GeV}{c^2} = GeV$$

Unit of momentum:

$$\frac{mc^2}{c} = \frac{GeV}{c} = GeV$$

Unit of length:

$$\frac{\hbar c}{mc^2} = \left(\frac{GeV}{\hbar c}\right)^{-1} = GeV^{-1}$$

Unit of time:

$$\frac{\hbar}{mc^2} = \left(\frac{GeV}{\hbar}\right)^{-1} = GeV^{-1}$$

Using the energy-mass equivalence relation (2.3.2) we can express the mass of electron in units of energy as,

$$m_e = \frac{E}{c^2} = \frac{m_e c^2}{c^2} = \left(9.11 \times 10^{-31}\right)\left(\frac{(3 \times 10^8)^2}{c^2}\right)$$

$$8.199 \times 10^{-14}\frac{J}{c^2} = 5.11 \times 10^5 \frac{eV}{c^2} = 0.511\frac{MeV}{c^2}$$

and the mass of Proton as,

$$m_p = 1.5048 \times 10^{-10}\frac{J}{c^2} = 9.38 \times 10^8 \frac{eV}{c^2} = 938\frac{MeV}{c^2}$$

and the mass of neutron as,

$$m_n = 1.5066 \times 10^{-10}\frac{J}{c^2} = 9.40 \times 10^8 \frac{eV}{c^2} = 940\frac{MeV}{c^2}$$

2.4 Limitations of Standard Model (SM)

There are many successful predictions made by the SM, including the Higgs boson prediction,bosons in the gauge system (W and Z bosons), top quarks, and charm quarks, which are now being experimentally observed. Below we describe some limitations of the system despite its success.

- **Gravity**

Gravity, one of nature's basic forces, is excluded from the standard model, making it one of its biggest weaknesses. Furthermore, this theory does not explain why gravity is so much weaker than electromagnetic and nuclear forces. There is no explanation for the gravitational interaction and its mediator graviton, which is supposed to be a spin-2 boson.

- **Neutrinos oscillation**

Neutrinos are considered massless particles in the Standard Model. Although neutrinos are massive particles, they oscillate in accelerators and also change flavor during flight, demonstrating they are oscillating[12].

- **Matter-antimatter asymmetry and Dark matter**

The big bang may have created equal amounts of matter and antimatter. But the universe at that time seemed dominated by matter. This is known as the matter-antimatter asymmetry. It is neither explained nor generated in the SM.

The standard model covers only about 5% of the universe's matter, according to astronomical studies. Dark matter comprises 26% of the universe's mass, with dark energy accounting for 69 percent of its energy. Beyond the Standard Model, both dark matter and dark energy exist. SM also fails to describe the asymmetry spot in creation between matter and antimatter [13].

2.5 Rapidity (y)

The non linearity of classical velocity addition makes it less straightforward to transform between inertial frames of reference in the theory of relativity [13]. This difficulty can be overcome by introducing the concept of rapidity, y defined as

$$y = \frac{1}{2} ln \left(\frac{1 + \beta}{1 - \beta} \right) \tag{2.5.1}$$

where $\beta = \frac{\nu}{c}$ Using natural units it simplifies to

$$y = \frac{1}{2} ln \left(\frac{1 + \nu}{1 - \nu} \right) \tag{2.5.2}$$

The formula for rapidity addition, which is linear like the classical velocity addition formula but not like the relativistic velocity addition formula, is as follows,

$$y_{\nu'} = y_\nu + y_\mu \tag{2.5.3}$$

The speed may be described in terms of energy and momentum of the object rather than velocity if we multiply both the numerator and denominator within the logarithm of 2.5.2 by a factor of γm.

$$y = \frac{1}{2} ln \left(\frac{E + p_z}{E - p_z} \right) \tag{2.5.4}$$

where $E = \gamma m$ and $p = \gamma m \nu$

The offspring particles created in collision experiments are propelled in the direction of the beam axis (in the z direction). The speed distribution [13] is a better way to represent the angular distribution. The expelled particle's rapidity (y) and azimuthal angle (ϕ) are often coupled(y,ϕ). By doing this, the angle between two events, $(y_2 - y_1, \phi_2 - \phi_1)$, is maintained as a function of boost along the beam axis (z-axis).

2.6 Pseudorapidity (η)

Rapidity only has one drawback: it is more difficult to quantify for extremely relativistic particles (such as in hadron colliders). In these situations, we need both energy and total momentum, but it is often exceedingly challenging to measure the total momentum vector of a relativistic particle, particularly at high values of the speed (i.e., when approaches to c), when the z component of the total momentum is too big. This challenge may be overcome, however, by defining a relativistic kinematic variable, the pseudorapidity, which is virtually identical to particle rapidity but considerably simpler to measure than rapidities for extremely energetic particles since it just requires the angle [13]. Starting from the definition of y,

$$y = \frac{1}{2} ln \left(\frac{E + p_z}{E - p_z} \right) \tag{2.6.1}$$

Using the energy-momentum-mass relation,

$$y = \frac{1}{2} ln \left(\frac{(p^2 c^2 + m^2 c^4)^{\frac{1}{2}} + p_z c}{(p^2 c^2 + m^2 c^4)^{\frac{1}{2}} - p_z c} \right)$$

and after doing some mathematical calculation, we can show that,

$$y = \frac{1}{2} ln \tan \frac{\theta}{2}$$

And we define the pseudorapidity as,

$$\eta = -ln \tan \frac{\theta}{2} \tag{2.6.2}$$

Therefore, the rapidity and pseudorapidity for extremely relativistic particles are equal. Figure 2.6.1 makes it clear that η has a value of 0 for particle trajectories parallel to the beam axis ($\theta = 90°$), but non zero values for trajectories aligned with the beam axis.

Pseudorapidity is a crucial metric widely employed in colliding beam studies to represent the particle angular distributions with respect to the beam axis. The majority of particles leaving the detectors go perpendicular to the beam axis, which corresponds to $\eta = 0$. While big values are associated with particles that travel in directions near to the beam line. The middle region of the detector is the area with $|\eta| < 1.4$, and the forward region is the area with high η values (near the beam line). The direction of an outgoing particle in a detector can be represented nicely in the $\eta - \varphi$ space. Since the difference in η $(\Delta\eta)$ and φ $(\Delta\varphi)$ is independent of the Lorentz boost, hence the directions of two outgoing particles can be distinguished in terms of a third Lorentz invariant variable, ΔR in the $\eta - \varphi$ space as,

$$\Delta R = \sqrt{\Delta\eta^2 + \Delta\varphi^2} \qquad (2.6.3)$$

Particles that move parallel to one another lay near one another in the $\eta - \varphi$ space, or have a short ΔR separation distance.
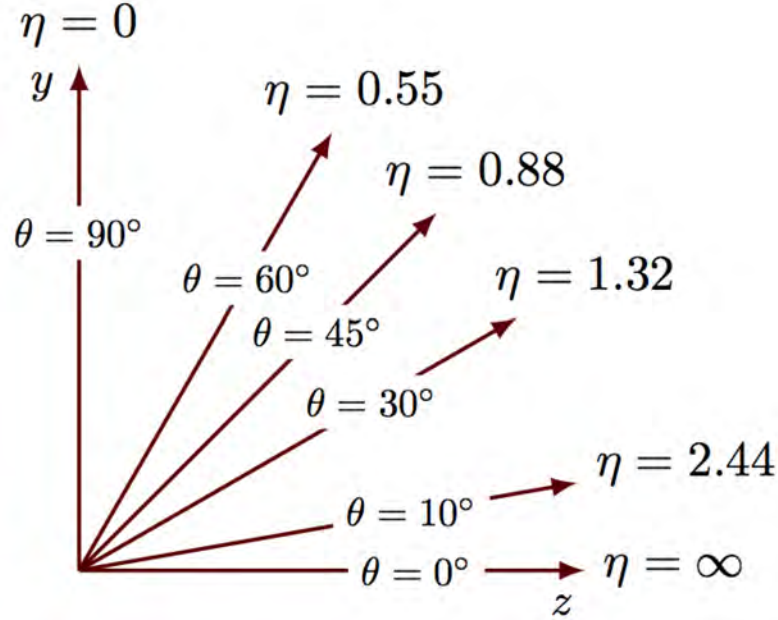
Figure 2.6.1: θ dependence of η [14].

2.7   Centre of mass energy E_{cm}

The energy measured in a system of particles' centres of mass, centres of momentum, or E_{cm} is referred to as the system's centre of mass energy. The threshold energy level for the formation of new particles is also known as this because it is the maximum energy that may result from colliding particles and is all the energy that is available to do so. Because the energy of the motion of the centre of mass itself remains with the centre of mass and does not affect the internal characteristics of the system, the centre of mass energy of a system remains invariant and can be detected by any inertial observer.

Mandelstam Variable, s which is invariant and is given by

$$s = (p_1 + p_2)^2 c^2$$

$$t = (p_1 - p_3)^2 c^2$$

$$u = (p_1 - p_4)^2 c^2 \qquad (2.7.1)$$

where p_1 and p_2 are the entering particles four-momenta and p_3 and p_4 are the departing particles four-momenta. The square of the center-of-mass energy (invariant mass) is s, while the square of the four-momentum transfer is t.

2.8 Transverse momentum P_T and Energy E

Secondary particles are accelerated along the beam axis of high energy particle collisions. The particles' rest mass and transverse momentum are the only quantities that are not Lorentz boosted. The three momentum components that are perpendicular to the beam axis are referred to together as the transverse momentum. They are given by the mathematical relation,

$$p_T = \sqrt{p_x^2 + p_y^2} \qquad (2.8.1)$$

or from the geometry of the detector,

$$p_T = p \sin \theta \qquad (2.8.2)$$

The energy determined when the boosted component of the three momenta (p_z) is identically zero, i.e. $E_T = E$(when $p_z = 0$), is the transverse energy of the secondary or daughter particles.

Mathematically,

$$E_t^2 = E^2 = p_x^2 + p_y^2 + m_0^2 \qquad (2.8.3)$$

$$E_t^2 = p_T + m_0^2$$

or from the relation of energy-momentum four vector

$$E_t^2 = E^2 - p_z^2 \qquad (2.8.4)$$

The particles produced in collider experiments are often enhanced along the beam axis. An invariant quantity is the momentum components that are perpendicular to the beam axis (p_T). Transverse momentum is significant in collider physics because longitudinal momentum p_z may only be a byproduct of beam particles, but transverse momentum is always linked to newly created particles.

Chapter 3

Baryon Number

In particle physics, the baryon number is a key idea that clarifies how matter behaves. Protons and neutrons are examples of baryons, which are crucial for the existence of matter. A system's baryon count is represented by the preserved baryon number. The importance of baryon number and its relationship to other conservation rules will be discussed in this chapter. We'll talk about the experimental proof for the conservation of baryon number and how it affects our comprehension of particle interactions.

We'll also discuss the fascinating subject of baryon number violation, in which specific conditions permit changes in baryon number. However, the Large Hadron Collider (LHC)'s baryon number transfer at various energies will be our major emphasis.

3.1   Carrier of Baryon Number

The baryon itself serves as the bearer of the baryon number. Three quarks are linked together by the strong nuclear interaction to form the baryon class of particles. The proton and neutron, which are made up of up and down quarks, are the two most well known baryons. A baryon carriers a baryon number of $+1$, signifying that there is one baryon present in the system. The antiproton is an example of an anti-baryon, which has a baryon number of -1. The total baryon number before and after a reaction is guaranteed to stay constant by the conservation of baryon number in particle interactions. This conservation law is essential to our comprehension of the stability and behavior of matter. Although it appears to be very clear and correct, let's examine the reaction,

$$\pi^- + p \longrightarrow \Omega^- + K^+ + 2K^\circ \tag{3.1.1}$$

It is evident that the reaction conserves baryon number. In the reaction's quark diagram, no valence quarks from the first proton show up as valence quarks, as can be seen in Figure 3.1.1.
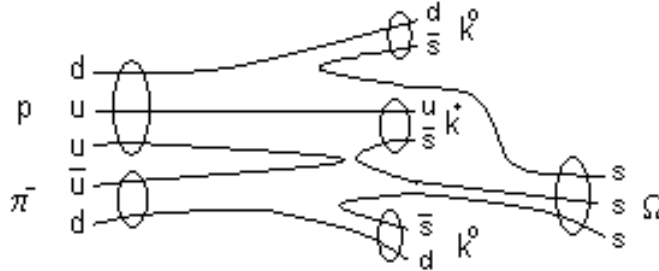
Figure 3.1.1: Diagram of the quark for process given in 6.1.1. None of incident quarks are seen in the final baryon.

Therefore, the other partons in the proton, the gluons, must carry the baryon number. The Central collision of heavy ions is another instance that creates doubt on the idea that valence quarks carry baryon number. What transpires as a result of the collision? The valence quarks store a sizable fraction of the energy from colliding nuclei. We are aware that the energy loss experienced by quarks as they go to across a large nucleus is minimum and independent of energy. The value of approximately $\triangle E \approx 10 GeV$ for the energy loss of valence quarks as they traverse a large nucleus primarily comes from experimental observations and theoretical calculations in the field of high-energy nuclear physics [51]. Therefore, soft contact cannot stop high energy quarks. Soft collisions cause the valence quarks to lose a relatively tiny amount of energy on gluon radiation as they go through the collision zone. As a result, valence quarks will carry the baryon number to the region of fragmentation if they are baryon number carriers. Numerous gluons and softer quark-antiquark pairs are left behind. The original valence quarks totally loose their identities as nucleon constituents after propagation via a hefty nucleus. Fragmentation jets, largely made up of mesons, are produced as a result of the process and relatively few baryon-antibaryon couples. As a result, When nuclei collide, the baryon number they carry becomes immobilised in the collision zone and cannot be found in the beam fragmentation region. As you can see there is a problem.

3.2   Nature of Baryon Number

Understanding the nature of baryon number, its conservation and any potential violations or transport mechanisms connected to it offer important new perspectives on the dynamics of the early cosmos as well as the fundamental rules of physics as shown in Figure 3.2.1. We

are making great strides in our understanding of the basic building blocks of matter, thanks to research done at particle accelerators like the Large Hadron Collider (LHC) and others.

Symbol	Name	Quark content	Electric charge	Mass GeV/c²	Spin
p	proton	uud	1	0.938	1/2
p̄	anti-proton	ūūd̄	−1	0.938	1/2
n	neutron	udd	0	0.940	1/2
Λ	lambda	uds	0	1.116	1/2
Ω⁻	omega	sss	−1	1.672	3/2

Figure 3.2.1: The baryon number is the total number of baryons in a system minus the total number of antibaryons.

3.2.1 Hadrons' color fields' string configurations

The color fields in mesons and baryons have quite distinct string configurations. A quark antiquark pair coupled by a colour flux tube resembles a meson as shown in Figure 3.2.2 [35]. Color algebra provides the configuration's ultimate color state,

$$\{3\} \otimes \{3^-\} = \{1\} \oplus \{8\} \tag{3.2.1}$$

where nature fully expresses the color singlet. Quark confinement in hadrons is the term for this reality.
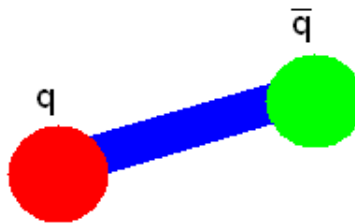
Figure 3.2.2: String configuration of a meson.

The baryon was initially described as a quark-diquark pair in the Constituent Quark Model as shown in Figure 3.2.3 [36]. The baryon number (BN) is carried by the valence

23

quarks in this scenario; each of them has BN=$\frac{1}{3}$. Baryon numbers are absent from gluons. In this concept, the diquark has a solid structure and cannot split apart upon a collision.
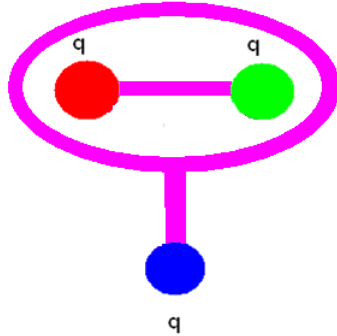
Figure 3.2.3: In the component quark model, a baryon's string configuration is a quark-diquark pair.

3.2.2 Baryon Number Annihilation

In 1970, experiments on baryon number annihilation by pp^- were conducted. Important conclusions include the fact that the $\frac{\bar{p}}{p}$ annihilation cross section will remain visible at high energies and that its speed distribution will be rather uniform if the baryon number is related to the gluonic configuration. The claim that the $\frac{\bar{p}}{p}$ annihilation cross section is energy independent at high energies was first made by Gotsman and Nussinov[37]. The overlap of a string antijunction and gluonic string junction, followed by a rearrangement of the gluonic strings, as shown in Figure 3.2.4 is what they claimed caused annihilation using a string junction model. According to the assumption that the size of the string junction is on par with the transverse dimension of the strings, or between 0.2 and 0.3 fm, the annihilation cross section was calculated.
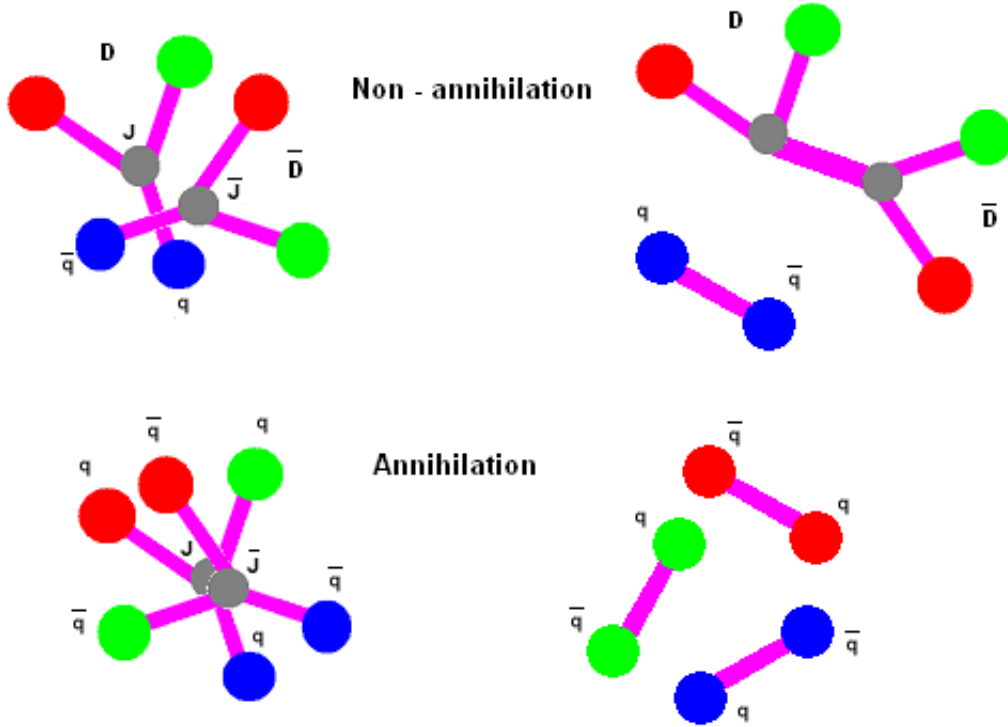
Figure 3.2.4: The image depicts the interaction of an antibaryon with a baryon made up of a diquark (D) and a quark. The non-annihilation final state with two strings results from the crossing of the strings in the plane responsible for impact. When the string junction (J) and string antijunction (J̄) overlap, three strings are produced.

3.3 Baryon Number Transport

The incoming projectile splits into numerous hadrons in an inelastic non-diffractive proton-proton collision at a very high energy. Typically, these hadrons appear after the collision at tiny angles parallel to the initial beam path. The term "baryon-number transport" is frequently used to describe the arriving proton's slowdown, or more precisely, the beam particles' connection to the conservation of the baryon number.

In baryon-antibaryon pair formation, the majority of antibaryons are produced at moderate speed, indicating similar yields. Any excess of baryons over antibaryons is connected with this because of the baryon-number transfer from the incoming beam. When the mid-rapidity antibaryon-to-baryon asymmetry is measured, it is possible to look at baryon transport over extremely large rapidity intervals. The asymmetry is given by,

$$A_{BN}(y) = \frac{N_{BN} - N_{\overline{BN}}}{N_{BN} + N_{\overline{BN}}} \tag{3.3.1}$$

where $N_{BN}, N_{\overline{BN}}$ is a function of $y's$ and represents the density of generated baryons and antibaryons.

3.4 Baryon Number Transport at Various LHC Energies

3.4.1 Low energy regime

- **Experimental Observation**

LHC experiments examine baryon number conservation at relatively lower energies. Using collision data, they track baryons and antibaryons' synthesis, decay, and interactions. Experiments such as particle identification and event reconstruction are used to determine the characteristics and attributes of the particles involved.

- **Theoretical interpretations**

A comparison is made between theoretical models and forecasts in the low energy zone in order to make sense of the experimental results and understand the behavior of baryons and antibaryons. In order to explain baryogenesis and matter-antimatter asymmetry theoretically, one must examine the forces and particles involved in the baryon number transmission process.

3.4.2 High energy regime

- **Experimental observations**

In the regime of high energy, baryon number transfer is being investigated. At the LHC, they provide conditions for generating large particles and investigating quark gluon plasma (QGP) at the highest possible energy. The analysis of collision data allows us to investigate the production rates, decay pathways, and interactions of baryons and antibaryons[47].

- **Exploration of transport mechanisms**

Observations in the high-energy zone provide a useful framework for understanding baryon number transport methods. QGP is being studied in relation to baryon number transfer and how it impacts the imbalance between matter and antimatter. In order to understand how QGP affects the conservation or violation of baryon number, they research its characteristic and behavior, including its viscosity, temperature, and longevity [47].

3.5 Transverse momentum and dependency

It is possible to determine the difficulty of a collision by measuring transverse momentum. Violent collisions produce particles with a higher transverse momentum. In many collisions, harder collisions result in more particles generated, which is why transverse momentum and multiplicity are related variables.

In earlier sections, we noted that the overall multiplicity resulting from an event involving a separate baryon number transport method is inversely related to the number of broken strings involved in the event. The string junction itself conveys baryon numbers, so high multiplicity samples are more likely to give rise to events with baryon numbers. The transverse momentum can be explained similarly. In general, the antibaryon to baryon ratio will decrease with multiplicity or as a function of transverse momentum. Antibaryon to baryon ratios have been evaluated in numerous experiments, but there was no drop at mid-rapidity. Proton proton collisions' most recent finding is from the STAR experiment [38] at $\sqrt{s} = 200 Gev$.
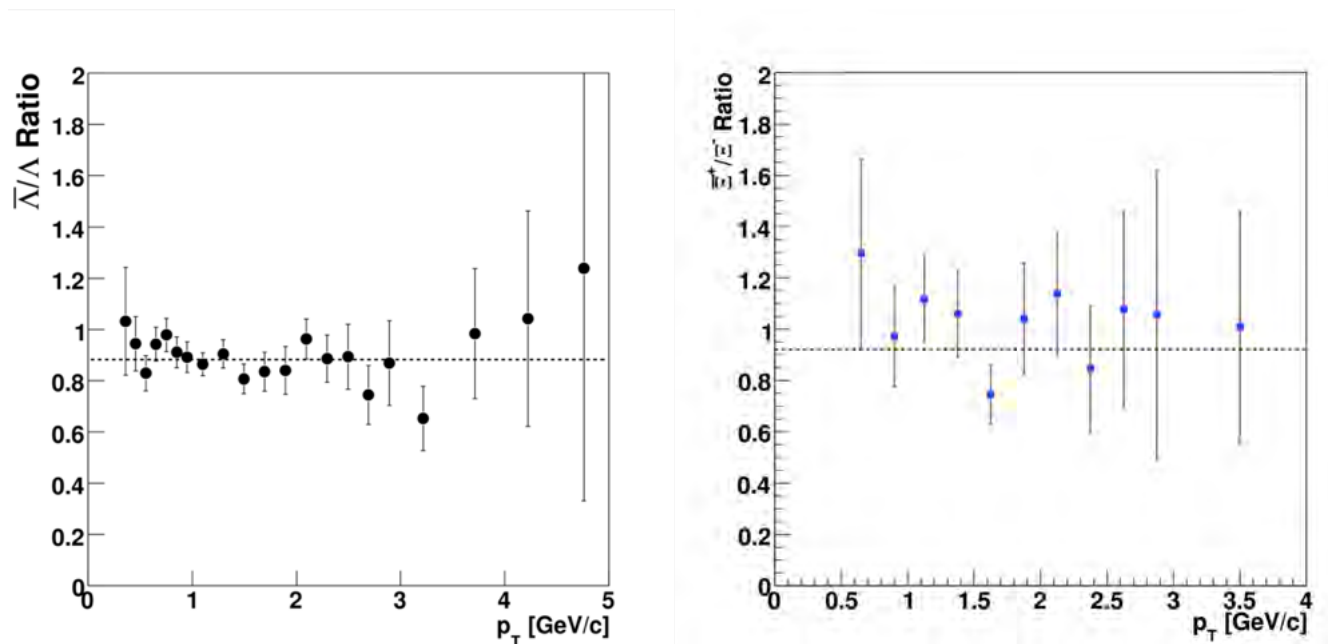
Figure 3.5.1: $\frac{\overline{\Lambda}}{\Lambda}$ (left) and $\frac{\overline{\Xi}^+}{\Xi^-}$ (right) relationship between ratio and transverse momentum p_T measurement of the STAR experiment at $\sqrt{s}$=200GeV (38).

Chapter 4

Analysis and Results

Anti-baryon to baryon ratios ($\frac{\bar{p}}{p}$, $\frac{\bar{\Lambda}}{\Lambda}$, $\frac{\overline{\Xi^+}}{\Xi^-}$) in pp collisions at $\sqrt{s}$ = 0.9, 2.76, 7 TeV from DPMJET-III, Pythia8, EPOS1.99, and EPOS-LHC model simulations are shown in this chapter as the excitation function. Model simulations provide ratios that are then compared to the ALICE experiment data.

4.1 Methodology

The Monte Carlo method will be used for physics analysis at high energies. Detailed instructions on how to accomplish our goal are given below.

4.1.1 Monte Carlo Simulations

A Monte Carlo simulation is a method of calculating the outcome of an event by using multiple probability simulations. It is normally used in simulations that use probabilistic methods to create new arrangements of interest. A Monte Carlo simulation must be based on a random plan. It has the advantage of not requiring equations to be solved, this allows for brilliance to be displayed in the arrangement of trial arrangements in the statistical mechanics ensemble. Monte Carlo simulations are based on probability functions and are a means of analyzing likely outcomes by switching a set of values - a probability distribution for any factor with inherent uncertainty. Using a different set of random values each time, it repeats the process [39].

4.1.2 How We Can Generate the Random Numbers

In almost all standard statistical methods, random numbers are generated. Computers are usually used to perform random sampling in most analyses. Using Monte Carlo methods,

Bayesian analysis can be performed. There are a variety of methods for generating random numbers. Monte Carlo methods, which rely on millions of random numbers, use physical processes as sources of random numbers. Rather than "random" numbers, most applications use pseudorandom numbers, which are deterministic but appear random[40].

4.2   Monte Carlo Events Generators

Different types of Monte Carlo Event generators are used for high energy / heavy ion collision. We used **Pythia8** for this purpose.

Lund Monte Carlo began with the JETSET, which was developed by the Lund theory group in 1978. Many programs were based on it, including PYTHIA. PYTHIA 6.4 was released as the main version a few years later. For the first time, PYTHIA 6.4 was based on FORTRON 77. PYTHIA was rewritten completely in C++ in 2004, and in 2007, PYTHIA 8.1, which was completely written in C++, was published. During the first run of the LHC, the experimental sector relied on PYTHIA 6.4. However, its development was halted in 2012. Pythia 8.2 was released in 2014, and Pythia 8.3 was released in 2019. In both versions, there are a number of new features. The PYTHIA8 program is widely used to generate high energy collision processes, consisting of coherent sets of physical models that describe the progression from a few- body hard process to numerous nal state particles. The analysis in PYTHIA is performed at the quark and gluon level, and is based on the internal leading order (LO) framework as shown in Figure 4.2.1. Hadronic collisions are covered by PYTHIA, including elastic, inelastic, dispersive, and non-dispersive events. The concept of multiparton interaction (MPI) is used in PYTHIA8. A number of libraries of physical phenomena are included in it [41].
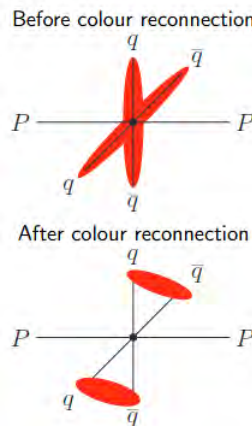
Figure 4.2.1: Colour reconnection mode of PYTHIA8.

The Monash tune is a particular set of settings used with the Pythia8 event generator to mimic the hadronization and decays of particles created in high energy particle collisions. Hadronization is the process by which quarks and gluons form bound states known as hadrons. Monash Tune was used in the current research work.

4.3 Cosmic Ray Monte Carlo Software (CRMC)

This monte carlo simulation of cosmic rays that provides a user interface to various event generators to simulate both cosmic and noncosmic ray phenomena. In CRMC, an event generator can be accessed through a standard interface. The system models the creation of secondary charged particles during hadronic collisions. In CRMC, outputs are stored as root or HepMC events. CRMC supported models are discussed below.

4.3.1 EPOS-LHC

EPOS-LHC is another Monte Carlo cosmic ray event generator based on Regge's theory. Energy saving quantum mechanical technique based on partons is known as EPOS [42]. Pomeron exchanges are used in EPOS to explain beam particle interactions as shown in Figure 4.3.1. In addition to their softness, semi-hardness, and hardness, these Pomerons may also be semi-hard. Phenomenologically speaking, two Quark-Gluon ladders connected to remnants by two colour singlets (legs) from the parton sea constitute a soft Pomeron. When two strings split apart, hadrons are created. The tastes of the string ends need to be balanced out by the leftovers. Particularly with EPOS 1.99, EPOS has evolved into a core-corona model.

Figure 4.3.1: : Description of energy sharing in EPOS-LHC.

Hadronization is handled collectively for sections with a higher density of string segments than the critical density, whereas it is not managed collectively for regions that have different weights of string segments.

4.3.2 EPOS.199

In high-energy scenarios, the combined cross-section for interactions between hadrons is determined by convoluting the two parton distribution functions (PDFs). This calculation is based on perturbative Quantum Chromodynamics (pQCD) principles and utilizes PDFs obtained from experiments involving deep inelastic scattering. In general, they are fragmented into hadrons. Parton ladders are parameterized in Regge pole fashion [43]. It is also necessary to consider remnants that are usually colorless excited quark-antiquarks. Consequently, The hadron-hadron interaction in the EPOS model consists of two components: the outside contribution (from the remnants) and the interior contribution (from the parton ladder).

EPOS 1.99 [44], released in 2009, was specifically designed to analyze LHC data in depth. The version was called EPOS-LHC [45]. There are different hadronic interactions that can be reproduced by EPOS-LHC, including pp, pN, and N N interactions, where N can be between one and 210 nucleons in a range of energy between 40 GeV and 1000 TeV in the center-of-mass frame. In the EPOS-LHC, radial flow algorithms are used to resolve the collective hadronization in pp collisions due to the very high density matter at the LHC energies.

4.3.3 DPMJET-III

A DPMJET-III incorporates all the features of a DPMJET-II. Simulations of hadron-nuclei (hN) are based on Gribov-Glauber's multiple scattering formalism. A several interactions can be studied ranging from the interaction of hadron-hadron (hh),photon-hadron (γh), nucleus-nucleus (NN),photon-nucleus(γN), as well as photons with photons($\gamma\gamma$) interactions. Based on the Dual Parton Model (DPM), DPMJET characterises soft and multi-partonic interactions in high-energy interactions. DPMJET is capable of doing entire (quasi) elastic computations and calculating cross-sections for a variety of colliding systems. Model DPMJET-III incorporates a new feature that uses enhanced graph cuts for inelastic non-diffractive collisions in hN and NN. Additional information on the DPMJET-III model is available in Ref [46].

4.3.4 ROOT Data Analysis Framework

ROOT is a free, object oriented data analysis framework written in the C++ programming language. . Switzerland has developed this technique since its inception CERN near Geneva. To help the high-energy physics community overcome the difficulty of analyzing vast amounts of complex data, this programme was developed. Computational physics aims to correlate experimental data with multiple theoretical models as a basis. A model is a function that

predicts measurable data, which is based on parameters. ROOT, a highly competitive software for research and computational modeling, analyzes and visualizes the model's results. As a center of high energy physics, ROOT offers scientists an optimal work environment. Data analysis is performed using ROOT by thousands of professionals everyday. The ROOT application allows users to save, read, mine, and display data, as well as to run interactively. Simulating data is also an important aspect of data analysis. Also, simulations are used to see how generalisation affects results.
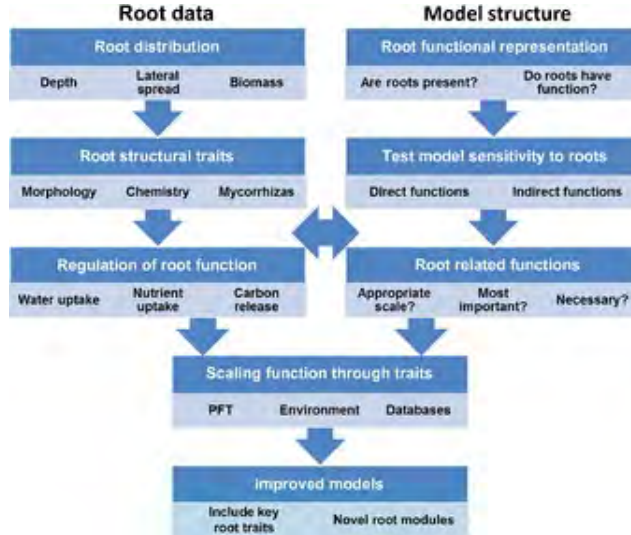
Figure 4.3.2: Framework for assessment of ROOT data.

This data might be stored as a ROOT file in the ROOT framework. Whenever the source source program describing the data is not accessible, we can process the results from ROOT code. There are many ways to access data saved in a root directory, whether it is on a computer, the web, or in a large distribution system as shown in Figure 4.3.2.

4.4   Data Set

The DPMJET-III, Pythia 8, EPOS 1.99, and EPOS-LHC models were used to simulate 5 million events for pp collisions at $\sqrt{s} = 0.2$, 0.9, 2.76, and 7 TeV for each model in order to analyze the data. The final state hyperons were taken into consideration in the rapidity window $|y| < 0.8$ and $|y| < 0.5$ was taken in case of $\frac{\bar{p}}{p}$, which is motivated by the intrinsic limits of the present ALICE experiment[49]. Because they can be followed in the detector, particles with lifetimes $c\tau > 10$ mm are regarded as final state particles. Table 4.4.1 lists the cuts that were used in this investigation to determine the transverse momentum (p_T) and rapidity (y) distributions.

$\sqrt{s}(TeV)$	$\frac{\overline{p}}{p}$		$\frac{\overline{\Lambda}}{\Lambda}$		$\frac{\overline{\Xi}^{+}}{\Xi^{-}}$	
	$\boldsymbol{p_T}$	$\lvert y \rvert$	$\boldsymbol{p_T}$	$\lvert y \rvert$	$\boldsymbol{p_T}$	$\lvert y \rvert$
0.9	]0.45 , 1.05[	< 0.5	]0.5 , 4.0[	< 0.8	]0.5 , 3.5[	< 0.8
2.26	]0.45 , 1.05[	< 0.5	]0.5 , 4.5[	< 0.8	]0.5 , 4.5[	< 0.8
7	]0.45 , 1.05[	< 0.5	]0.5 , 10.5[	< 0.8	]0.5 , 5.5[	< 0.8
13	]0.45 , 1.05[	< 0.5	]0.5 , 10..5[	< 0.8	]0.5 , 5.5[	< 0.8

Table 4.4.1: p_T and y cuts used to study $\frac{\overline{B}}{B}$ ratios at LHC energies.

4.5 Results

As a function of p_T and y at LHC energies, we provide the $\frac{\overline{B}}{B}$ ($\frac{\overline{p}}{p}$, $\frac{\overline{\Lambda}}{\Lambda}$, and $\frac{\overline{\Xi}^{+}}{\Xi^{-}}$) ratios obtained using the different model simulations outlined in section 4.3. It is significant to note that the $\frac{\overline{\Omega}^{+}}{\Omega^{-}}$ ratio was not examined in this research owing to insufficient statistics. A detailed summary of the outcomes for each $\frac{\overline{B}}{B}$ ratio is provided.

4.6 Rapidity and transverse momentum dependence

4.6.1 $\frac{\overline{p}}{p}$

The analysis of p_T as a function of the ratio $\frac{\overline{p}}{p}$ at different collision energies ($\sqrt{s}$) is a valuable tool in the study of high-energy particle physics. It provides insights into the energy dependence of particle production and contributes to our understanding of the fundamental interactions of particles at the highest collision energies achievable in accelerators like the LHC. Figures 4.6.1 to 4.6.5 show the distribution for $\sqrt{s} = 0.9$ TeV, 2.76 TeV, 7 TeV, 13 TeV and 200 GeV. Following that, the simulation output from the DPMJET-III, Pythia8, EPOS 1.99, and EPOS-LHC models is compared to the experimental data from ALICE [50].
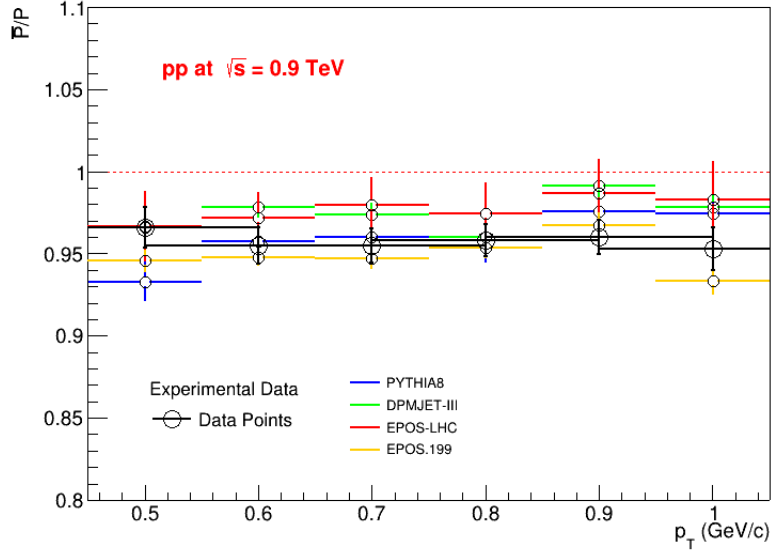
Figure 4.6.1: Ratio $\frac{\bar{p}}{p}$ as a function of transversal momentum p_T at $\sqrt{s}$=0.9 TeV. Comparison of experimental data to several monte carlo forecasts.

Figure 4.6.1 depicts the $\frac{\bar{p}}{p}$ ratio versus p_T in pp collisions at $\sqrt{s} = 0.9$ TeV. Following that, the simulation output from the **DPMJET-III**, **Pythia8**, **EPOS1.99**, and **EPOS-LHC** models is compared to the experimental data from ALICE [47],[48]. The ALICE data exhibits no p_T dependency, and the $\frac{\bar{p}}{p}$ ratio is almost constant at 0.95 across all p_T bins. In contrast, the **DPMJET-III**, **Pythia8,** and **EPOS1.99** models do not exhibit any p_T dependency while correctly reproducing the data patterns. The ratio, however, is somewhat overpredicted by the **EPOS-LHC** model for larger p_T bins ($p_T > 0.7$ GeV/c).

Figure 4.6.2 presents the comparison of the differential ratio of $\frac{\bar{p}}{p}$ at $\sqrt{s} = 2.76$ TeV as a function of p_T. In comparison to the experimental data, EPOS1.99, EPOS-LHC, DPMJET, and Pythia8 agree well with the experimental data. Figure 4.6.3 also presents good agreement with experimental data at $\sqrt{s} = 7$ TeV.
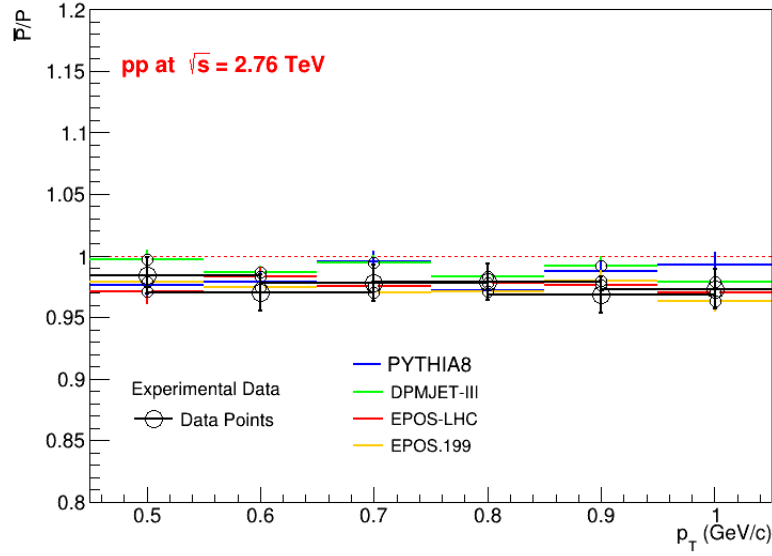
Figure 4.6.2: Ratio $\frac{\bar{p}}{p}$ as a function of transversal momentum p_T at $\sqrt{s}$=2.76 TeV. Comparison of experimental data to several monte carlo forecasts.
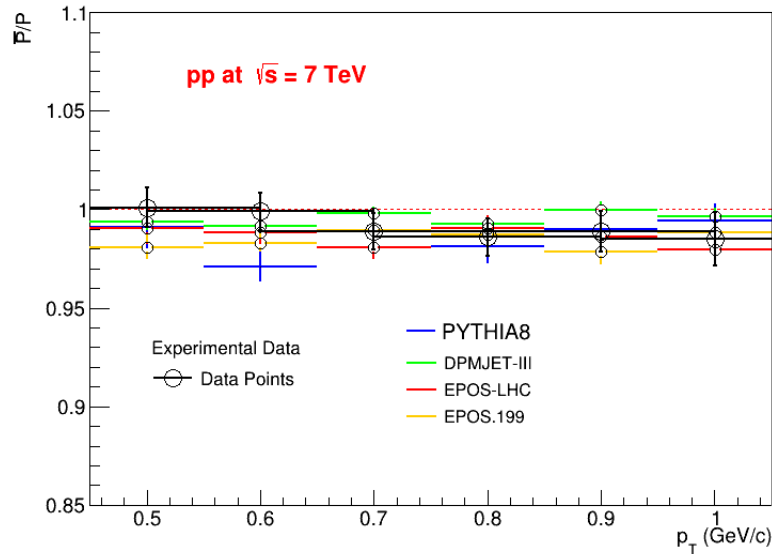
Figure 4.6.3: Ratio $\frac{\bar{p}}{p}$ as a function of transversal momentum p_T at $\sqrt{s}$=7 TeV. Comparison of experimental data to several monte carlo forecasts.

Figures 4.6.4 and 4.6.5 present the comparison of the differential ratio of $\frac{\bar{p}}{p}$ at $\sqrt{s}$=13 TeV and $\sqrt{s} = 200$ GeV as a function of p_T. The various models, including EPOS1.99, EPOS-LHC, DPMJET, and Pythia8, have been evaluated. These models show expected trends whenever experimental data is available .
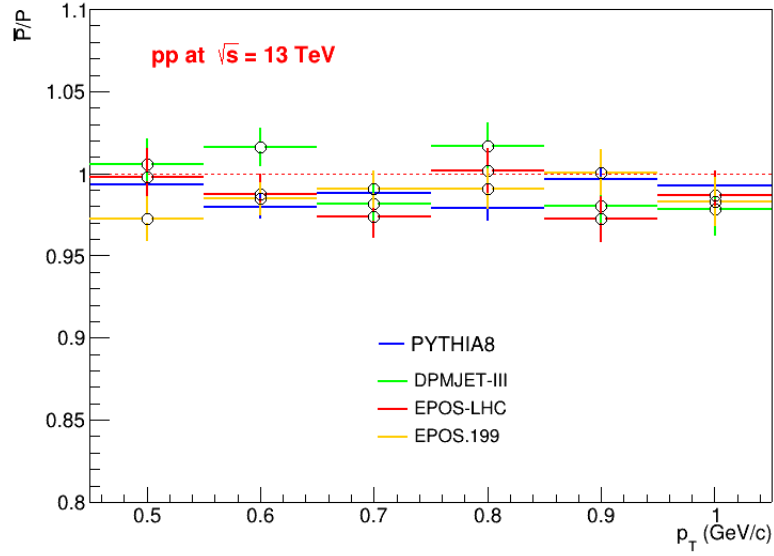
Figure 4.6.4: Ratio $\frac{\overline{p}}{p}$ as a function of transversal momentum p_T at $\sqrt{s} = 13$ TeV as predicted by simulation.
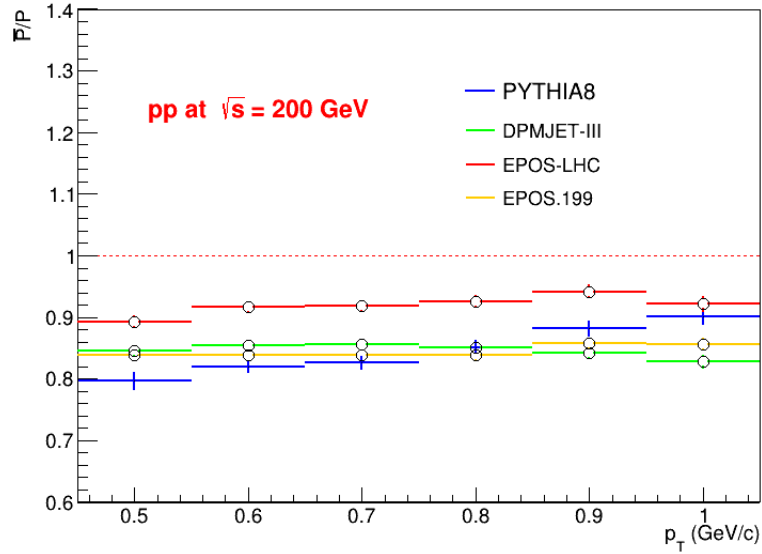
Figure 4.6.5: Ratio $\frac{\overline{p}}{p}$ as a function of transversal momentum p_T at $\sqrt{s} = 200$ GeV as predicted by simulation.

4.6.2 $\frac{\overline{\Lambda}}{\Lambda}$

The $\frac{\overline{\Lambda}}{\Lambda}$ ratio as a function of p_T and y at $\sqrt{s} = 0.9$ TeV, 2.76 TeV, 7 TeV, 13 TeV and 200 GeV are shown in Figures 4.6.6 to 4.6.15. The horizontal bars provide the width of the y

or p_T bin, while the vertical bars show the statistical uncertainty. Figure 4.6.6 shows the predicted results by different models at $\sqrt{s} = 200$ GeV for different y values.
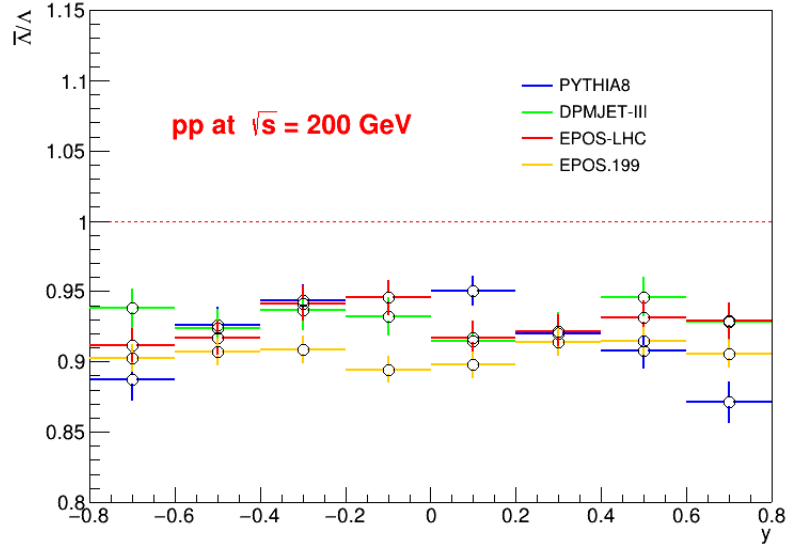
Figure 4.6.6: Ratio $\frac{\overline{\Lambda}}{\Lambda}$ as a function of rapidity y at $\sqrt{s} = 200$ GeV.

Figure 4.6.7 presents the comparison of the differential ratio $\frac{\overline{\Lambda}}{\Lambda}$ as a function of p_T at $\sqrt{s} = 200$ GeV. Compared to the STAR experiment, it is evident that all models show a greater deviation, but EPOSE-LHC and Pythia8 provide good agreement.
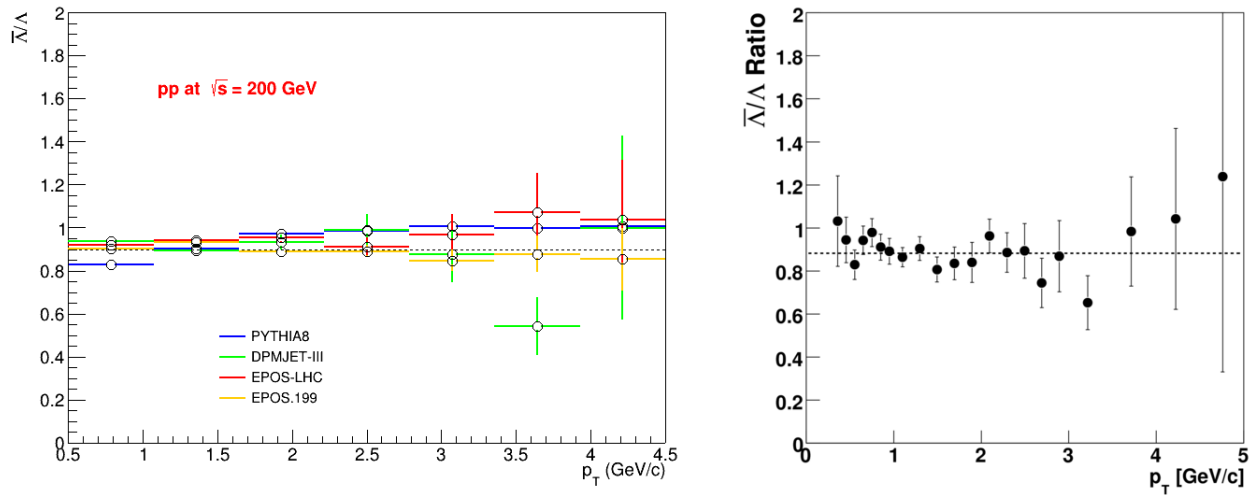
Figure 4.6.7: **(a)**Ratio $\frac{\overline{\Lambda}}{\Lambda}$ as a function of transversal momentum p_T at $\sqrt{s} = 200$ GeV **(b)** Results from STAR experiment[38].

Figure 4.6.8 shows the comparison of the differentail ratio $\frac{\overline{\Lambda}}{\Lambda}$ as a function of y at $\sqrt{s}$=0.9 TeV with experimental data from ALICE experiment. Overall, the EPOS-LHC, EPOS1.99, Pythia8, DPMJET models provide better agreement with experimental data.
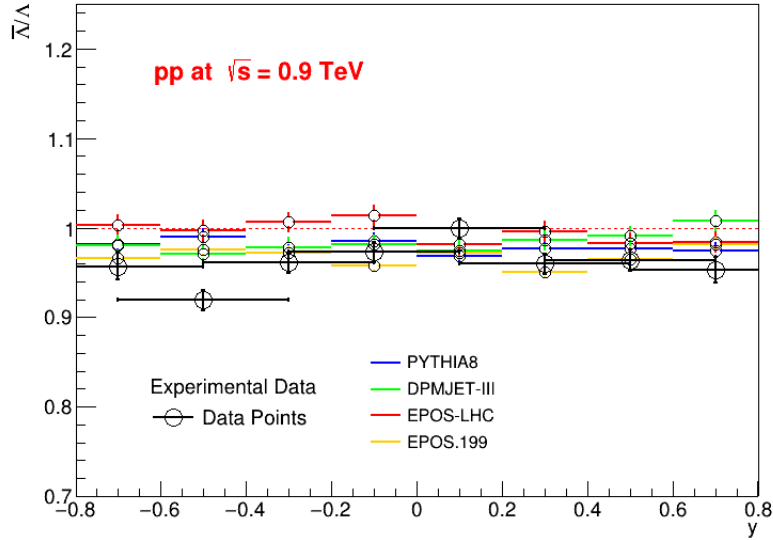
Figure 4.6.8: Ratio $\frac{\overline{\Lambda}}{\Lambda}$ as a function of rapidity y at $\sqrt{s}$= 900 GeV from experimental data and different monte carlo forecasts.

Figure 4.6.9 shows ratio $\frac{\overline{\Lambda}}{\Lambda}$ as a function of transversal momentum p_T at $\sqrt{s} = 900$ GeV. The EPOS-LHC, EPOS-1.99, and Pythia-8 show good agreement with experimental data. On the other hand, the DPMJET model does not agree with experimental data. Figure 4.6.10 shows the ratio $\frac{\overline{\Lambda}}{\Lambda}$ as a function of rapidity y at $\sqrt{s} = 2.76$ TeV. Overall, the EPOSE-LHC, EPOS1.99, Pythia8 provide good agreement with experimental data but DPMJET does not agree. In Figure 4.6.11, the EPOS1.99 and Pythia8 show a better agreement. On the other hand, the EPOS-LHC and DPMJET models do not agree.
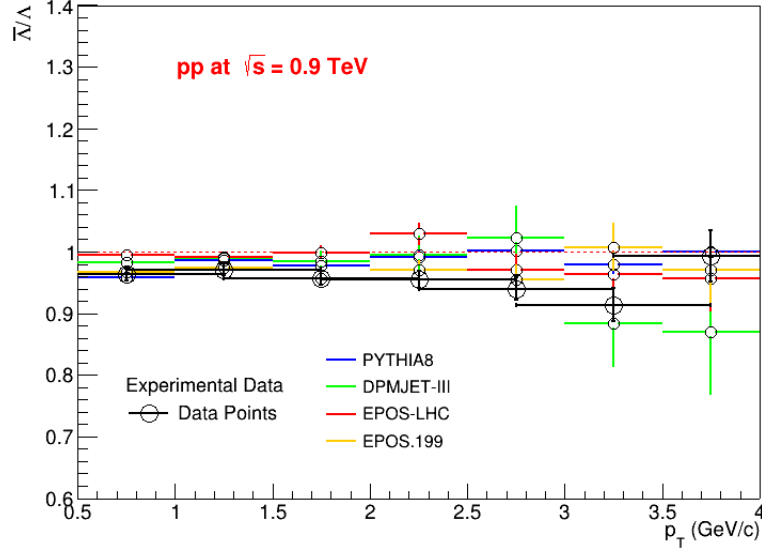
Figure 4.6.9: Ratio $\frac{\overline{\Lambda}}{\Lambda}$ as a function of transversal momentum p_T at $\sqrt{s}$ =0.9 TeV from experimental data and different monte carlo forecasts.
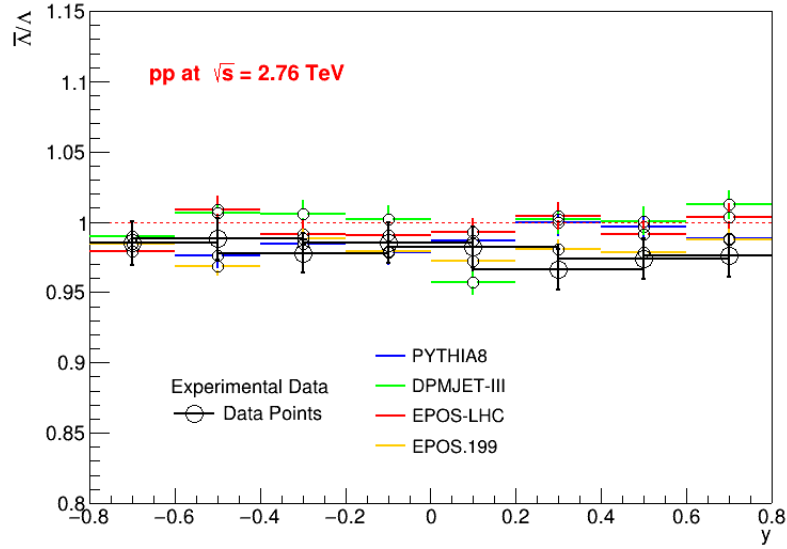
Figure 4.6.10: Ratio $\frac{\overline{\Lambda}}{\Lambda}$ as a function of rapidity y at $\sqrt{s}$ =2.76 TeV from experimental data and different monte carlo forecasts.

The comparison of the differential ratio as a function of y at $\sqrt{s}$ =7 TeV and p_T at $\sqrt{s}$ = 7 TeV. In Figure 4.6.12, the EPOS-LHC, EPOS1.99, DPMJET models provide good agreement with experimental data but Pythia8 slightly overestimates the experimental data. In Figure

4.6.13, the DPMJET and Pythia8 models agree with experimental data. On the other hand, the EPOS-LHC and EPOS-1.99 models do not agree when compared to experimental data.
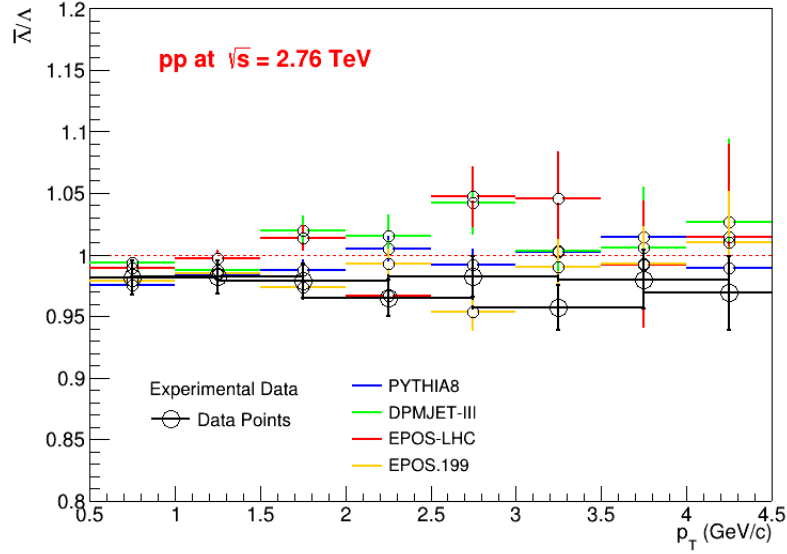
Figure 4.6.11: Ratio $\frac{\overline{\Lambda}}{\Lambda}$ as a function of transversal momentum p_T at $\sqrt{s}$ =2.76 TeV from experimental data and different monte carlo forecasts.
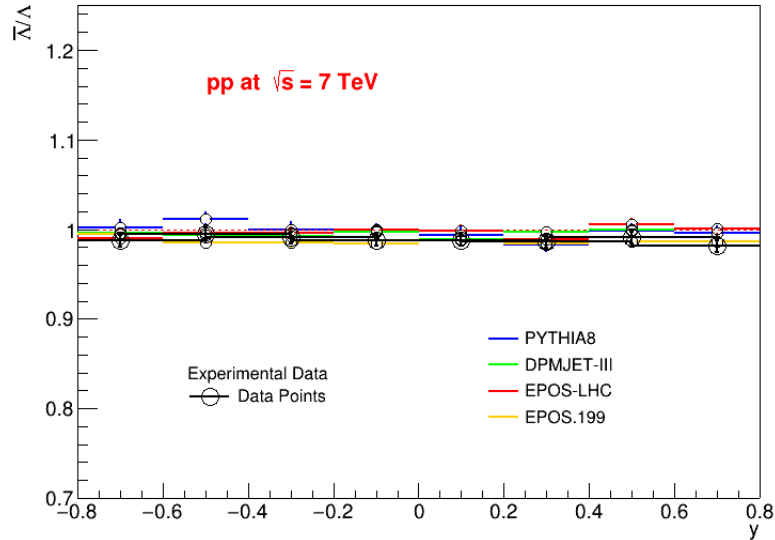
Figure 4.6.12: Ratio $\frac{\overline{\Lambda}}{\Lambda}$ as a function of rapidity y at $\sqrt{s}$ =7 TeV from experimental data and different monte carlo forecasts.
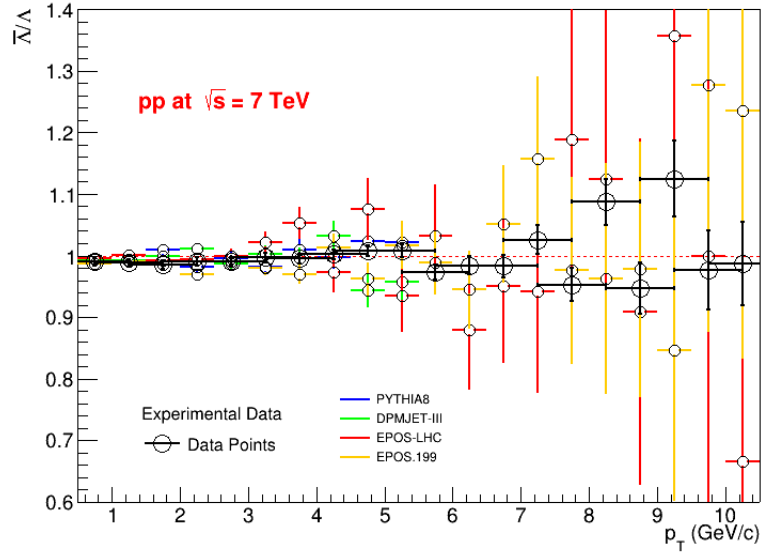
Figure 4.6.13: Ratio $\frac{\overline{\Lambda}}{\Lambda}$ as a function of transversal momentum p_T at $\sqrt{s}$ =7 TeV from experimental data and different monte carlo forecasts.

The results of the differential ratio $\frac{\overline{\Lambda}}{\Lambda}$ at $\sqrt{s}$=13 TeV as a function of y and p_T using all the models are shown in Figure 4.6.14 and 4.6.15.
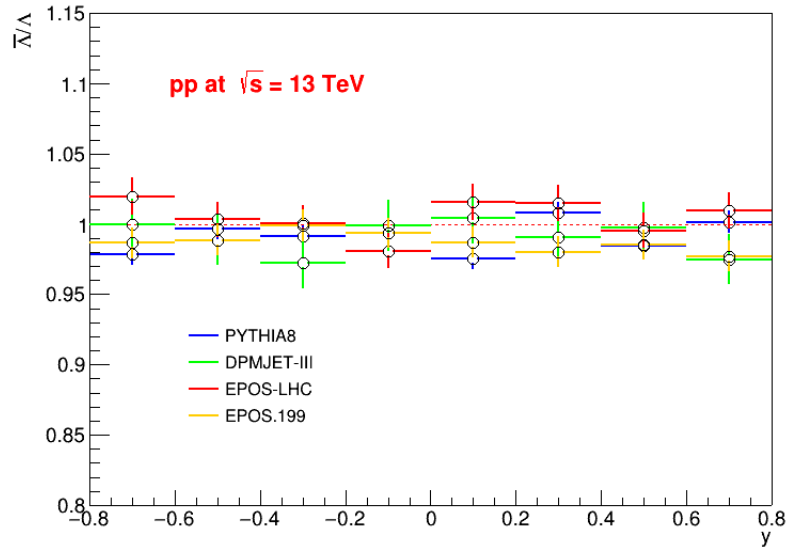
Figure 4.6.14: Ratio $\frac{\overline{\Lambda}}{\Lambda}$ as a function of rapidity y at $\sqrt{s}$ =13 TeV.
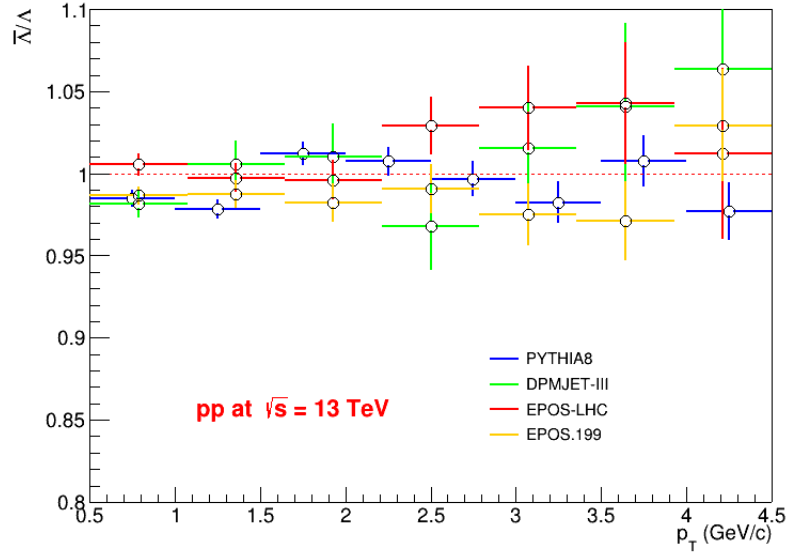
Figure 4.6.15: Ratio $\frac{\overline{\Lambda}}{\Lambda}$ as a function of transversal momentum p_T at $\sqrt{s}$ =13 TeV.

4.6.3 $\frac{\overline{\Xi^+}}{\Xi^-}$

The $\frac{\overline{\Xi^+}}{\Xi^-}$ ratio is predicted across various energies at $\sqrt{s}=$ 0.9 TeV, 2.76 TeV and 7 TeV as a function of p_T, the results are shown in Figures 4.6.16 to 4.6.19. Comparison of the EPOS-LHC EPOS1.99 and Pythia8 model with experimental values show good agreement but DPMJET does not show good agreement with the STAR data.

Figure 4.6.16 presents a comparison as a function of p_T of the differential ratio $\frac{\overline{\Xi^+}}{\Xi^-}$ at $\sqrt{s}=$200 GeV. The EPOSE-LHC, DPMJET and Pythia models provide a good agreement with the STAR experiment. On the other hand, The behavior of the EPOS1.99 is not good.
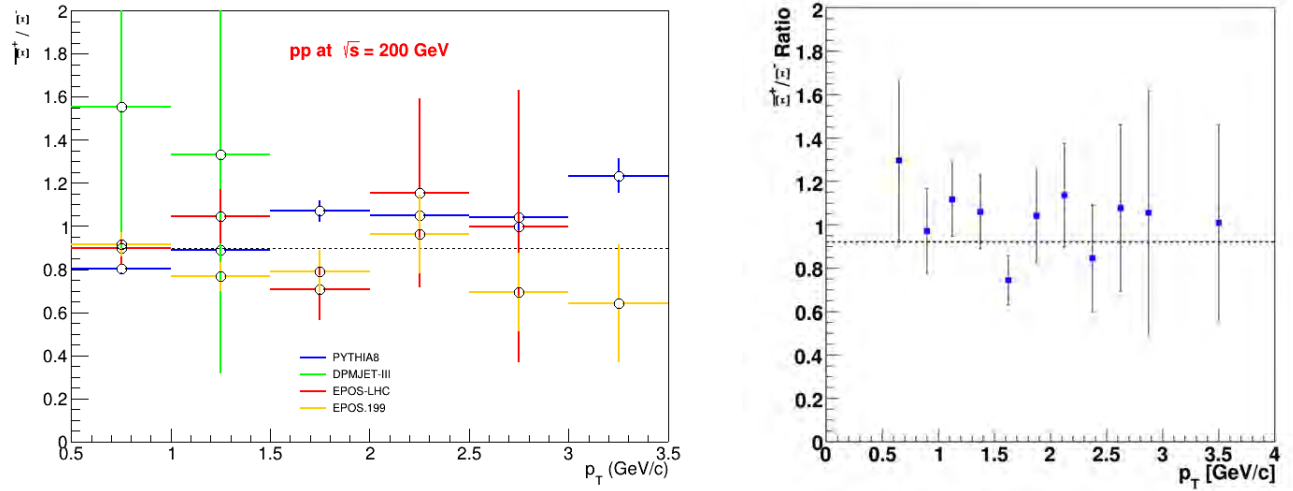
Figure 4.6.16: **(a)** Ratio $\frac{\overline{\Xi^+}}{\Xi^-}$ as a function of transversal momentum p_T at $\sqrt{s}$ =200 GeV. **(b)** Experimental results from STAR experiment at $\sqrt{s} = 200 GeV$ [38].

The comparison of ratio $\frac{\overline{\Xi^+}}{\Xi^-}$ as a function of p_T at $\sqrt{s}$ =0.9 TeV. In comparison to the experimental data, it is evident that all models show good agreement, but the DPMJET model overestimates, as shown in Figure 4.6.17.
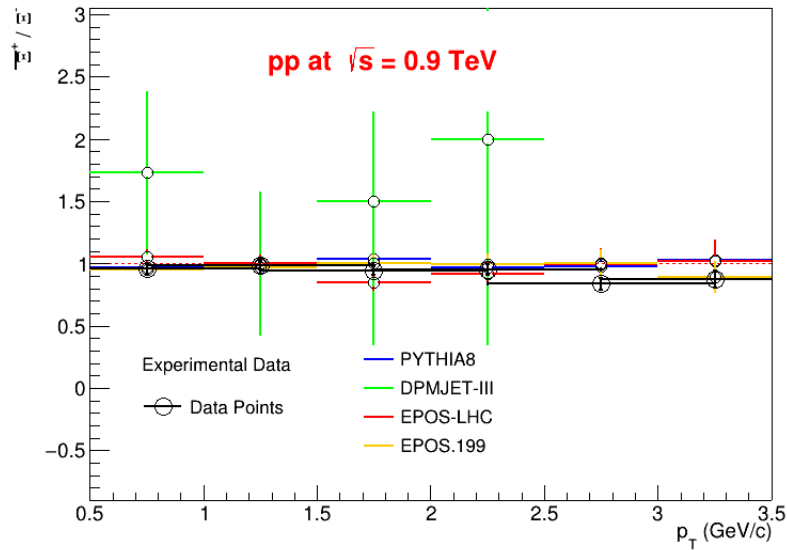
Figure 4.6.17: Ratio $\frac{\overline{\Xi^+}}{\Xi^-}$ as a function of transversal momentum p_T at $\sqrt{s}$ =0.9 TeV. Comparison of experimental data to several monte carlo forecasts.

Figure 4.6.18 shows ratio $\frac{\overline{\Xi^+}}{\Xi^-}$ as a function of p_T at $\sqrt{s}$ =2.76 TeV. Compared to the experimental data, EPOS1.99 and Pythia8 models show good agreement with the experimental

data. However, EPOS-LHC and DPMJET models do not show good agreement. In Figure 4.6.19, all models show better comparison with experimental data, but the DPMJET model does not agree.
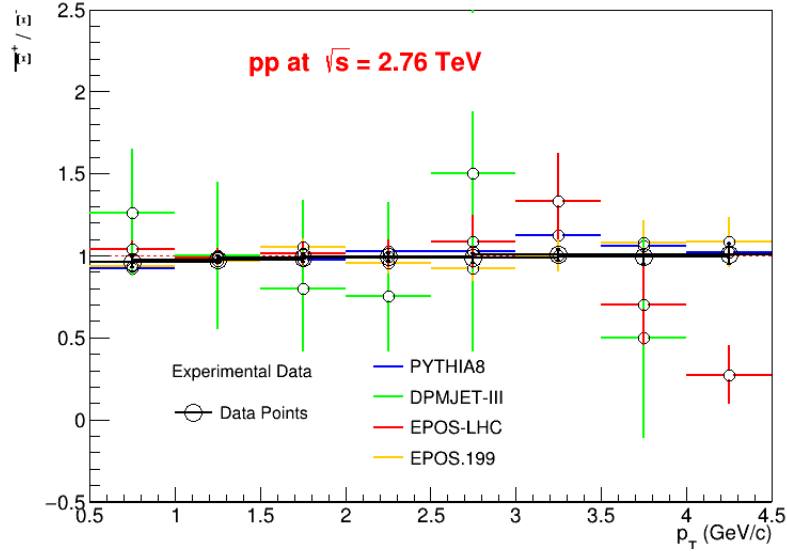
Figure 4.6.18: Ratio $\frac{\overline{\Xi^+}}{\overline{\Xi^-}}$ as a function of transversal momentum p_T at $\sqrt{s} =$2.76 TeV. Comparison of experimental data to several monte carlo forecasts.
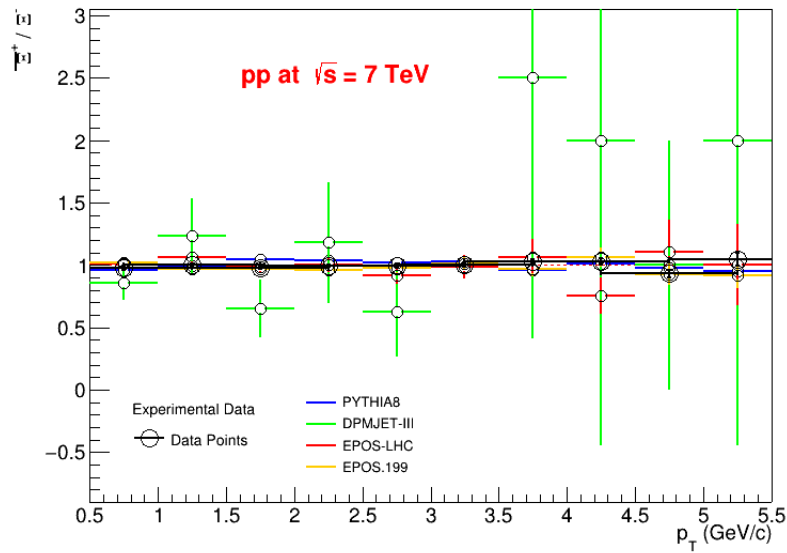
Figure 4.6.19: Ratio $\frac{\overline{\Xi^+}}{\overline{\Xi^-}}$ as a function of transversal momentum p_T at $\sqrt{s} =$7 TeV. Comparison of experimental data to several monte carlo forecasts.

4.6.4 $\quad \frac{\overline{B}}{B}$

In this study, the $\frac{\overline{p}}{p}$, $\frac{\overline{\Lambda}}{\Lambda}$ and $\frac{\overline{\Xi}^+}{\Xi^-}$ ratio are calculated using simulations of the DPMJET-III, Pythia8, EPOS1.99, and EPOS-LHC models at pp collision energies of 0.9, 2.76, 7, and 13 TeV. Combined results for p, Λ, and Ξ are shown in Figure 4.6.20. All model simulations conducted at lower energy levels, show a consistent observation of an excess of baryons compared to anti-baryons. This excess is directly linked to the transfer of baryon number from the incoming particle beam. However, this pattern changes at higher energy levels, where the creation of baryon-anti-baryon pairs leads to nearly equal production of both types. Notably, in the DPMJET-III model, the introduction of new diquark breaking diagrams slightly reverse this trend.
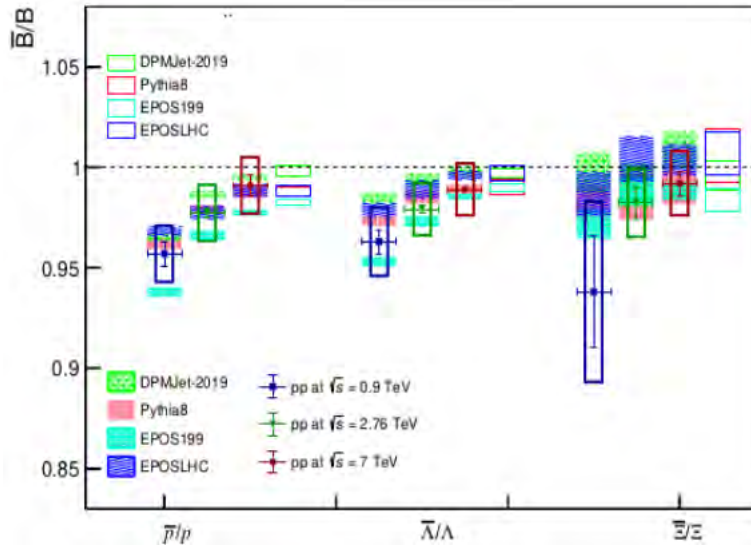
Figure 4.6.20: Comparing the $\frac{\overline{B}}{B}$ ratio with the DPMJET-III, Pythia 8, EPOS 1.99, and EPOS-LHC models at $\sqrt{s} = 0.9$, 2.76, and 7 TeV. Several models predict open squares of varying colors at $\sqrt{s}$= 13 TeV.

The $\frac{\overline{B}}{B}$ ratio may be nearing unity due to saturation of pair creation at higher energies, according to the model simulations. Additionally, comparable spectra for baryons and anti-baryons in pp collisions are predicted by model simulations for both variables p_T and y. We do not have published results for 13 TeV, but we will be able to compare them with published results once they become available.

Chapter 5

LHC and CMS Experiments

We will talk about the concepts and objectives of high energy experiments in this chapter of our thesis. In the first section, we'll quickly discuss the concepts behind why it's important to construct machines and technologies that can accelerate particles to relativistic levels and crash with each other. We will talk about the concepts of electric and magnetic fields in the second section, which are used to accelerate, divert and concentrate charged particle beams. The historical advancements of particle accelerators will be briefly discussed in the third portion of this chapter. We will also examine the large hadron collider (LHC) in some depth, as well as its several detector experiments, particularly the compact muon solenoid CMS, ALICE, ATLAS, which is the subject of our principal investigation.

5.1   Utilisation of Accelerators

One of the core fields of physics study is elementary particle physics, sometimes known as high energy physics. The study of matter's fundamental building blocks and their relationships with one another. High spatial resolution is required to explore these building pieces since their structure is considerably smaller than that of a nucleus. Visible light with a wavelength of λ= 500 nm is incapable of performing this duty, however high energy photons and other electromagnetic particle beams have shown to be useful instruments for this purpose [15]. If the electromagnetic radiation's wavelength is smaller than or equal to the size of the tiny objects being observed, they can be investigated. Therefore, in such experiments radiation with a wavelength between 10 and 15 nm is necessary. This range of wavelengths (10 to 15 nm) is used for observing tiny objects in high-energy physics experiments. The associated photon energy for this wavelength range is calculated as,

$$E_\gamma = h\nu = \frac{hc}{\lambda}$$

$$= 2 \times 10^{-10} \cong 1.25 \times 10^{9} eV$$

whereas $1eV = 1.602 \times 10^{-19}J$ is the kinetic energy gained by a free electron when it gets accelerated through a potential difference of 1 V. Kinetic energies of 1 MeV or higher are necessary for particles to smash into the nucleons to probe their structure or to ignite nuclear disintegration. In the collision of accelerated particles with matter at energies of 150 MeV, mesons are created whereas at energy of 1 GeV, other particles such as anti-protons, hyperons etc are created.

The purpose of particle accelerators is to provide charged particles from atoms and molecules, such as protons, electrons, and ions, with high kinetic energies. Particle accelerators, in a larger sense are electrical devices that accelerate charged particles with energies greater than 1 MeV. The electron and ion cannons are examples of particle accelerators along with X rays machines, cathode ray tubes etc. Nowadays there are more than 30,000 particle accelerators operational around the world.

5.2 Acceleration Principle for Particles

The energy of particles is similar to the speed of light in high energy tests. Their energy is provided by the relativistically invariant form given by,

$$E = \sqrt{m_o c^2 + p^2 c^2} \tag{5.2.1}$$

In the relation above m_o and c are constants, the only free parameter that can affect the particles energy is the relativistic momentum of the particles defined by

$$p = m\nu = \gamma m_o \nu \tag{5.2.2}$$

where $\gamma = \frac{1}{\sqrt{1-\left(\frac{\nu^2}{c^2}\right)}}$ is the Lorentz factor and m_o is the rest mass of the particle. The particle's increased energy is related to its increased momentum p. Whereas, according to Newton's second law of motion, the change in momentum is the result of a net force F acting on the particle.

$$\frac{dp}{dt} = F \tag{5.2.3}$$

In order to produce high energy particle beams, a sufficiently strong force must be exerted on the beam for a sufficient interval of time. We have four fundamental forces in nature i.e

the gravitational, the electromagnetic, the strong, and the weak force. The strong and weak forces have sufficiently small ranges ($\leq 10^{-15}m$). Hence are excluded from the race. The gravitational force is also too weak to perform this job (relative strength is 6×10^{-39}). The only choice we are left with is the electromagnetic force F_{EM}[15].

A charged particle with electric charge e moving with velocity ν in a volume with electric field E and magnetic field B held perpendicular to each other is acted upon by a Lorentz force F_L.

$$F_L = e\big(E + \nu \times B\big) \tag{5.2.4}$$

The change in kinetic energy of the particle as a result of this force when the particle moves from point r_1 and r_2 is given by,

$$\triangle E = \int_{r^1}^{r^2} F_L.dr = e \int_{r^1}^{r^2} \big(E + \nu \times B\big).dr \tag{5.2.5}$$

During this process the path element dr of the particle is along the velocity of the particle and thus $\big(\nu \times B\big)$ is perpendicular to the path element $\big(\nu \times B\big).dr= 0$. Hence the only agent responsible for the acceleration involving an increase in kinetic energy of the particle is the electric field E and the change in kinetic energy of the particle is thus

$$\triangle E_{kin} = \int_{r^1}^{r^2} E.dr = eV \tag{5.2.6}$$

where V is the voltage that causes the electric field E. Although the magnetic field does not change the kinetic energy of the particle, it has an important role in changing the path of the particle i.e it is responsible for steering, bending and focusing the particle beams. Accelerator physics involves the struggle for both accelerating and steering the particle beams upto maximum possible levels and the duty is performed by electromagnetic force, F_{EM} only [16].

5.3   The Large Hadron Collider (LHC)

The Large Hadron Collider or LHC is governed by the European Organization for Nuclear research, CERN is a huge scientific instrument that spans the Franco-Swiss border near Geneva, Switzerland (shown in Figure 5.3.1). It is the world's largest and most powerful particle accelerator. It involves almost 10000 physicists from more than 80 countries to search for particles and events that existed in the universe a fraction of second after the Big Bang [17]. It took almost 20 years and 3.6 billions euros in cost to design and construct

the LHC. It consists of 27 km long and 3.8 m wide tunnel that is stationed 100 m under the ground in the shape of a closed circular ring as shown in Figure 5.3.1 The LHC at this level enjoys a stable operating environment and any particle from within the tunnel cannot escape, also the particles from the outer environment are prevented to get in. Until 2000 the tunnel was the home of the Large Electron-Positron (LEP) storage ring, which was developed in 1989. The LEP experiment involved the acceleration and collision of electrons and their anti-particles positrons [17].
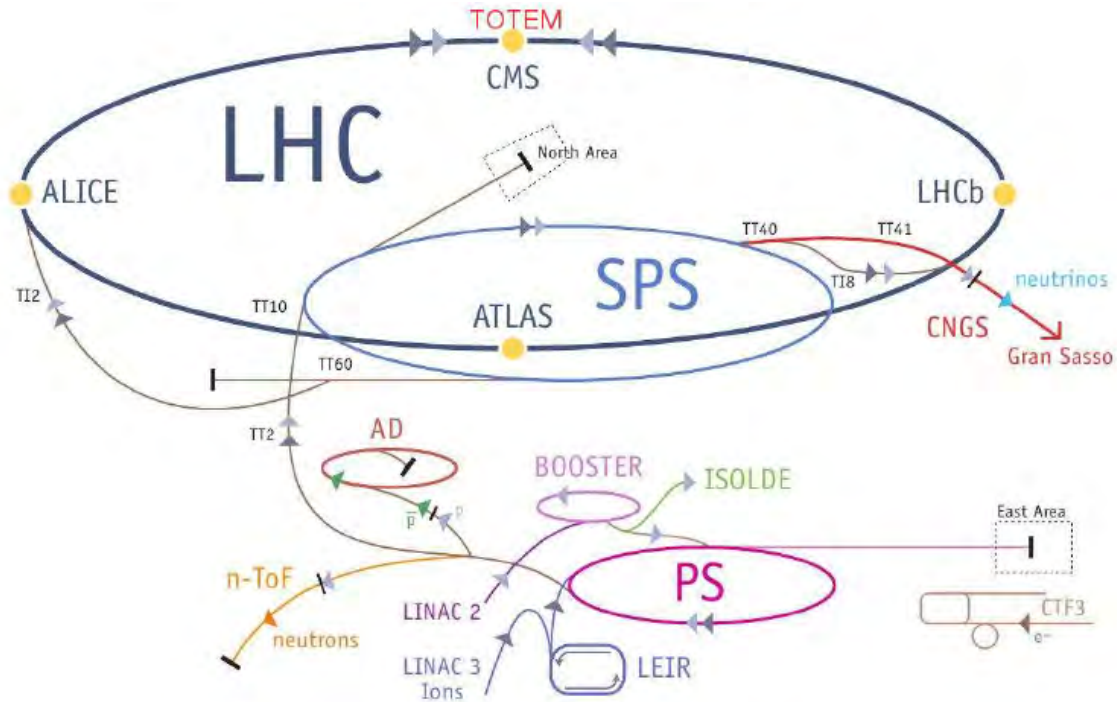
Figure 5.3.1: Layout of LHC at CERN[17]

5.3.1 The LHC and Physics

A collider experiment where two beams circulating in the LHC tunnel collide at one of its main detectors, possess a vast amount of information about how the fundamental forces of the universe act among the elementary particles of matter and has opened the doors for the discoveries of new particles and understanding their properties. Knowing the fact that new particles are produced whenever the particle energies cross certain threshold levels, physicists have been continuously trying to improve the energy and intensity frontiers of particle accelerators and have succeeded in developing extremely accurate and sensitive detectors and data acquisition system that can record several PB of data per year. The race which started with the development of Cockroft-Walton accelerator in the early 1930s came to an end

through today's colliding proton beams at the LHC at CERN. Next we will discuss the basic concepts used in colliding experiments such as particles flux, interaction rate, cross-section and luminosity.

- **Particles flux** (ϕ)

The flux of particles denoted by ϕ is defined as the number of beam particles N_b passing with velocity ν_b through a target area A_t lying perpendicular to the direction of the beam. It is given by,

$$\phi = A_t N_b \nu_b \tag{5.3.1}$$

The unit of measurement is number per second .

- **Intraction Rate (R)**

The interaction rate, reaction rate or event rate denoted by R is defined as the number of particles interactions per unit time. It is given by,

$$R = \frac{dN}{dt} = f N_1 N_2 \tag{5.3.2}$$

where f is the frequency of interaction, N_1 is the number of particles in the first beam (projectiles) and N_2 is in the second beam (target). If the particle beams have a Gaussian profile then the interaction rate is given by,

$$R = f \frac{N_1 N_2}{4\pi \sigma_x \sigma_y} \tag{5.3.3}$$

where σ_x and σ_y are the Gaussian horizontal and vertical widths of the beam which characterize the rms transverse beam sizes in the horizontal and vertical directions respectively. The interaction rate is measured in number of interactions per second.

- **Cross Section** (A^*)

Probability of an interaction can be expressed in terms of effective area known as cross-section which is used to describe total yields of the interactions regardless of energies or spatial distributions of emitted particles. The cross section or interaction cross-section A^* of an event is defined as the effective area around the target surface where the probability of interaction is maximum. It is given by

$$A^* = 4\pi \sigma_x \sigma_y \tag{5.3.4}$$

In collider physics terminology, cross-section is measured in barn (bn) where,

$$1bn = 10^{-24}cm^2 = 10^{-27}m^2$$

- **Luminosity ($\mathcal{L}$)**

The most important parameter in collider physics is the available energy for new particle production. This can only be provided by the colliding beam experiments because all of the energy is available and a little or no energy is lost in the motion of the centre of mass. The important machine parameter that measures the ability of a particle accelerator to produce the required number of interactions is called Luminosity$\mathcal{L}$[18] and is the proportionality factor between the interaction rate R and cross-section A^* as,

$$R = \mathcal{L}A^* \tag{5.3.5}$$

which can be shown to be

$$\mathcal{L} = \frac{R}{A^*}$$

The units of luminosity are $cm^{-2}sec^{-1}$. The designed luminosity of LHC is $10^{34}cm^{-2}sec^{-1}$. It is measured by observing the interaction rate of a process which is theoretically well understood. For example the well understood process,

$$\pi^+ \longrightarrow \mu^+ + \nu_\mu$$

has cross-section of about 20 $nb = 20 \times 10^{-33}cm^2$. Knowing the designed luminosity of LHC to be $10^{-34}cm^{-2}sec^{-1}$ we can expect about 200 such events to be observed per second.

- **LHC Cordinate System**

Most of the LHC detectors have cylindrical geometries therefore cylindrical coordinate system is the convenient choice. The coordinate system of LHC is a right handed coordinate system with x-axis towards the centre of the LHC ring. The z-axis is chosen along the beam line and y-axis towards the ceiling of the tunnel (upward). θ is the polar angle of the particle direction with respect to the +z-axis and ϕ is the azimuthal angle measured in the xy plane from +x-axis in the counter-clockwise direction (shown in Figure 5.4). The angular dependence is often expressed in terms of pseudorapidity η which is given by

$$\eta = -ln\left(tan(\frac{\theta}{2})\right)$$

and an event is represented by a point in the $\eta - \phi$ space.
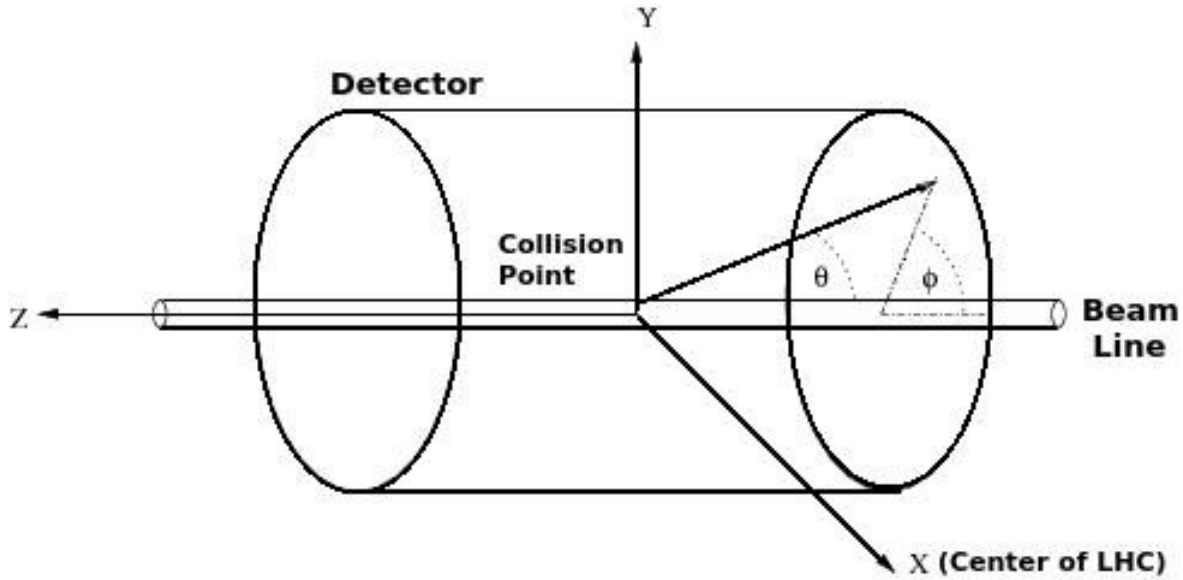
Figure 5.3.2: The geometry and coordinates of LHC detectors.

5.4   The Major LHC Experiments

To exploit the full physics opportunities provided by the LHC, specific experiments are designed around the LHC main tunnel. These include General or multi-purpose experiments which include CMS and ATLAS that are designed to study the full spectrum of events. Dedicated or special purpose experiments which include ALICE, LHCb, TOTEM, LHCf etc which are designed to study the specific channel of events. The TOTEM and LHCf share their interaction points with CMS and ATLAS respectively and are considered to be add ons to them.

5.4.1   LHC Detectors' Magnet System

The resulting particles after collisions in the LHC detectors are studied by measuring the energy deposition in the materials of the detectors and their paths which are followed by them in the presence of strong magnetic field provided by the detectors. The magnet system of the detectors is designed by wrapping superconducting wire coils in specific shapes. When electric current passes through these superconducting coils they generate a strong magnetic field which deviates the particles in different directions. The two most commonly used coil designing pattern to build magnet system in LHC detectors are;

- **Solenoidal Pattern**

A solenoidal coil is built when the metal wires are wrapped around the outer surface of a cylinder in the form of a spring or slinky. The magnetic field generated by a solenoid bends the particle beam in a plane perpendicular to the beam (clockwise or anti-clockwise)

- **Toroidal Pattern**

A Toroidal coil is built when the metal wires are wrapped in the shape of a bagel. The magnetic field generated by such coil deviates the particles beam in a plane parallel to the beam (forward or backward).

5.4.2 The ALICE Experiment

The second large detector at LHC that lies at Point 2 (P2) along the LHC main ring is the ALICE (A Large Ion Collider Experiment) detector. It is a 16 m tall, 16 m wide and 26 m long detector [19]. Unlike all other LHC detectors which are designed to study the outcomes of pp collisions. ALICE is dedicated to study the collision of lead (Pb) nuclei. In the collision of lead nuclei about 416 protons and neutrons are smashed with one another thus forming a condition in which quarks and gluons behave as free particles. This peculiar state of matter is known as the quark-gluon plasma. Scientists believe that quark-gluon plasma is the initial state of matter in our universe just after the Big-Bang [19]. The ALICE detectors consists of several layers of sub-detectors each of which uses different detection technology. The detectors around the IP are a series of cylindrical layers designed to record the particles exiting the collision i.e hadrons, photons and electron. These detector cylinders are of four types which are,

1. The silicon trackers.

2. The time projection chambers (TPCs).

3. A transmission radiation detector.

4. . A time of flight detector [19].

Next to these detectors sit two detectors which partially cover these cylinders. These are,

- Lead imaging Cherenkov counter.

- Lead tungstate crystal.
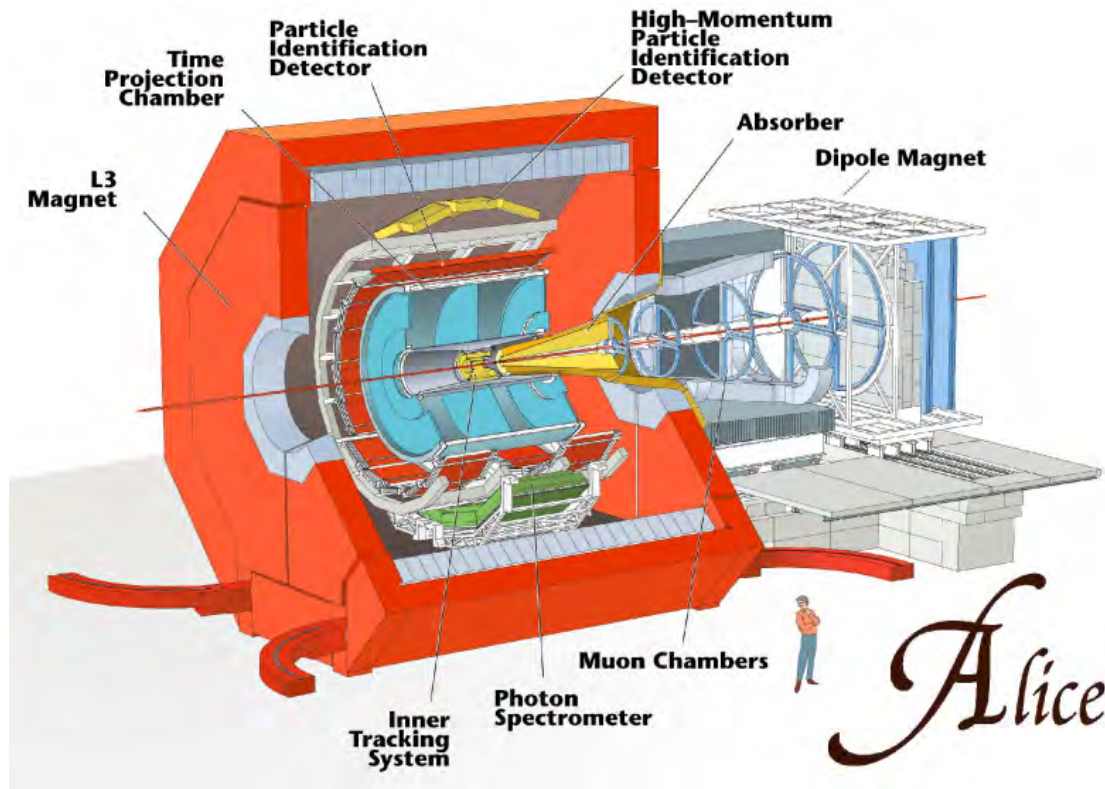
Figure 5.4.1: Computer model of the ALICE detector at LHC [19].

The lead tungstate is electromagnetic calorimeter and there is no hadronic calorimeter at all in the ALICE. These two detectors are surrounded by a huge solenoid magnet. At the ends of the ALICE main detector there sit conical style detectors specialized for muon detection [19]. The ALICE experiment shown in Figure 5.4.1, involves over 1000 scientists and engineers from more than 100 institutes in 30 countries around the world.

5.4.3 The CMS Experiment

The third main LHC detector and one of the two general purpose detectors is the CMS (Compact Muon Solenoid) shown in Figure 5.4.2 and is stationed at the LHC P5 around the main LHC ring, near Cessy, France. It takes the name because,

- 1. It is more compact than the ATLAS (ATLAS: 46 m long 25 m wide, CMS: 29 m long 15 m wide).

- 2. It is designed to detect muons much more efficiently.

- 3. It utilizes solenoid electromagnet to bend the charged particles [20].
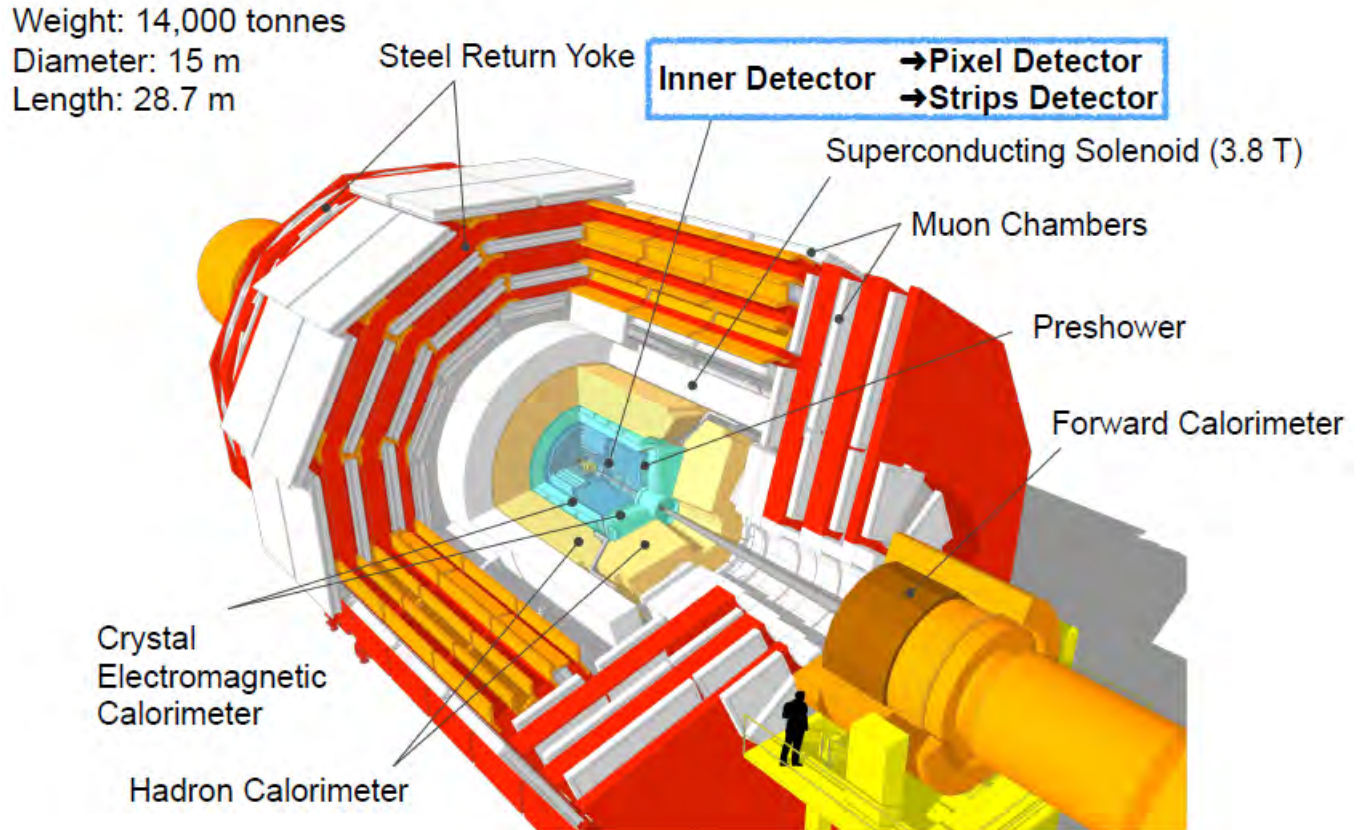
Figure 5.4.2: Computer model of the CMS detector at LHC [20].

Measurements for the CMS are as follows: length is 28.7 m and width is 15 m height and has a total weight of about 14, 000 tonnes [20]. It is a multi-layer detection system where different types of sub-detectors lie within one another. The detector layers are cylindrical in shape. It consists of six distinct layers of sub-detectors in the barrel region and five in the end-cap regions. In the barrel region these include two different types of silicon detectors, an electromagnetic calorimeter (ECAL), a hadronic calorimeter (HCAL), a magnet system and a muon detection system. The end-cap regions have the same layers except without the magnet system . In order to study the full pp collision spectrum, the CMS detector must be able to identify and distinguish among muons, electrons, and photons. Along with these particles, jets of particles are also produced which arise due to the hadronization of scattered quarks and gluons. Neutrinos and other weakly interacting particles escape the detectors without leaving any traces (shown in Figure 5.4.3). They are measured by determining the missing transverse momentum and energy. For this purpose the CMS detector is designed in such a way as to cover as much of the solid angle as possible [20].

The CMS detector is designed with such a technology so that it can with stand many challenges
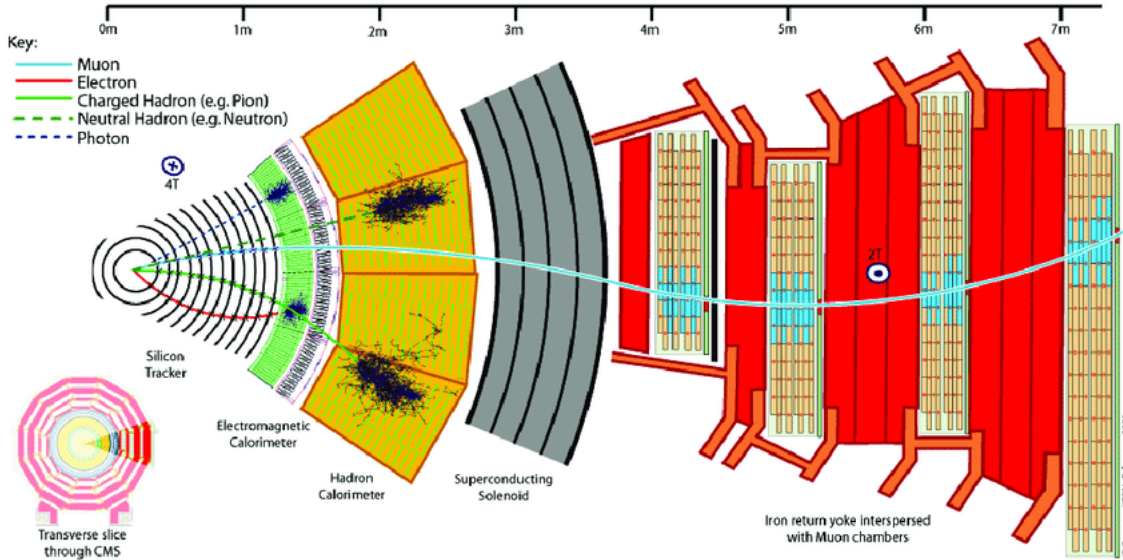
Figure 5.4.3: Transverse slice of the CMS at LHC in the barrel region [20].

that often reign at it. For example the extreme level radiations e.g 10^6 Gy per year and neutron flux of about 10^{15} per cm^2 in some parts of the detector [20]. Since CMS is our main focus of research, lets study its different components in detail.

- **Silicon Pixel Detector**

The CMS pixel detector sits closest to and around the LHC beam pipe. It has a cylindrical shape and consists of three layers of high granularity pixel detectors in the barrel region and four forward discs, two on each end of the cylinder. The three layers of the pixels in the barrel region lie at a radii of 4.4 cm, 7.3 cm and 10.2 cm and the forward discs lie at ±34.5 cm and ±46.5 cm from the interaction point (IP). The barrel region contains 115020 silicon chips with 48 million 100 μm × 150 μm silicon pixels whereas the end cap regions consist of 4320 silicon chips with 18 million pixels. The chips are contained in modules which are mechanical support structures with analogue readout optohybrid. To provide better particle capture, the modules are tilted by an angle of 20 degree. This arrangement of the barrel layers and forward discs on each side provides three tracking points coverage over the full η-range [21].
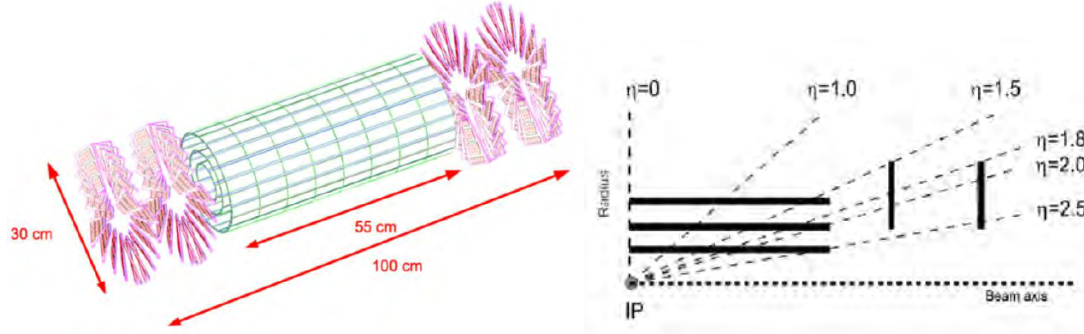
(a) CMS Pixel detector[21].

(b) η coverage range of CMS Pixel Detector[21]

Figure 5.4.4: Layout of CMS pixel detector and its pseudorapidity coverage range.

The pixel detector gives high resolution, three dimensional space points pattern. Their main purpose is To rebuild the initial and subsequent vertices originating from the decays of b's and τ 's. The first layer needs to be regularly replaced after one or two years of operations while the other layers can survive for a longer period. The sensors of the pixels are bump-bonded to about 4160 readout chips. Each chip amplifies the charge generated by a charged particle which causes ionization in the pixel, and delivers the analogue signals through optical links to the front end drivers in the underground control room situated at a distance of 100 m from the experimental cavern. The drivers upon receiving the signal convert them, digitize them and after formatting, send them to the data acquisition centre [21].

- **Silicon Strips Detector**

The silicon strip tracker shown in Figure 5.4.5 is the world s largest detector of this kind. Around 210 m^2 of silicon strips make up its active area which are chopped into 15148 microchip modules. Each module consists of one or two sensors. A single sensor is 320 µm thick (thin sensor), while a doublet sensor is 500 µm thick (thick sensor). There are about 6, 136 thin and 9, 096 thick sensors. Various tracker sub-parts need different module geometries. The sensors have 512 or 768 silicon strips which are read out by radiation resistant voltage (APV) chips. About 4-6 APV chips read out each sensor. An APV has a feature of 128 readout channels and in total there are 9.6 million such readout channels. These channels convey the electrical signals generated by the traversing particles to the front-end drivers for subsequent digitization and processing [22]. The pixel detector and silicon strip tracker combinedly constitute the CMS inner tracker whose main purpose is to trace the precise trajectories of electrically charged particles. It is constructed with such a design so that it can efficiently reconstruct high transverse momenta (p_T) muons as well as isolated electrons in the region $|\eta| < 2.5$ [22].

- **Electromagnetic Calorimeter (ECAL)**

Next to the inner tracker of the CMS there sits the electromagnetic calorimeter or ECAL. It measures the energies of electrically charged particles. Electrons, positrons, photons dissipate their energies by showering in the ECAL.
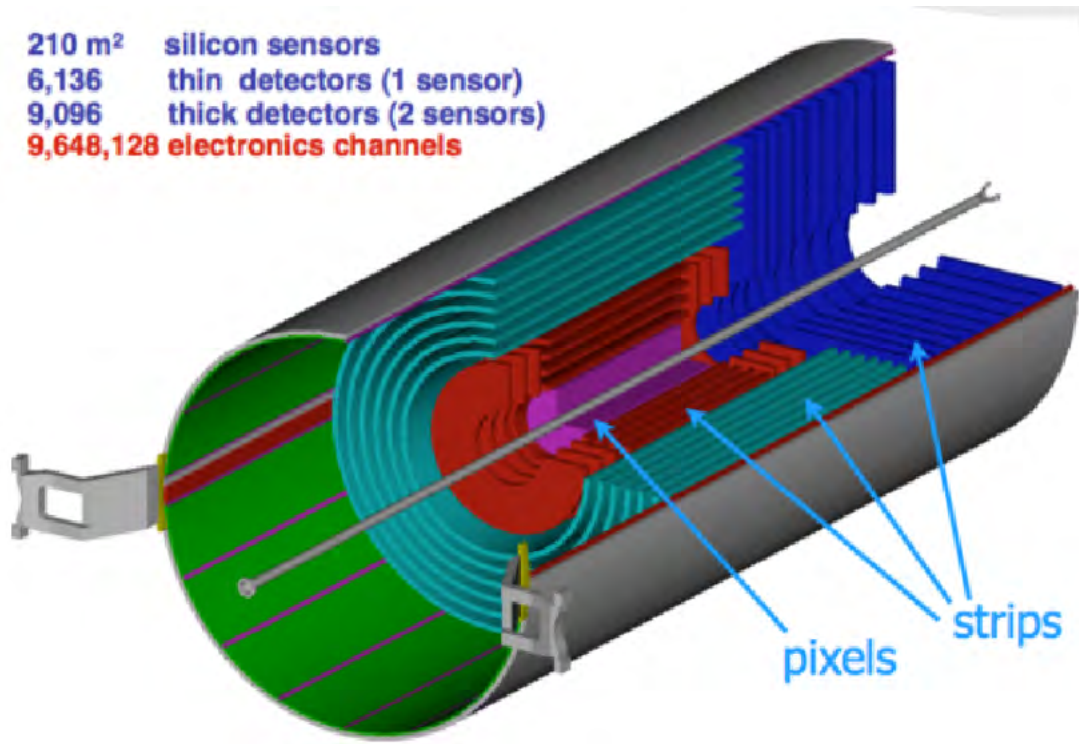
Figure 5.4.5: The layout of CMS silicon strips tracker with the pixels in the middle [22].

The CMS ECAL shown in Figure 5.4.5 is made up of lead-tungstate ($PbwO_4$) crystals where the electrons and photons interact mainly through bremsstrahlung and electron-positron pair production. This was motivated by the diphoton decay of Higgs boson which has a mass of around 125 $\frac{GeV}{c^2}$. The Higgs bosons are mostly detected at the central region of the detector ($\eta = 0$). To distinguish the diphoton decay of π^0 the endcap region is provided with pre-shower detectors. In order to withstand the radiation damage and magnetic field (4 T), photodetectors have been selected to readout the signals. In ECAL barrel region (EB) silicon avalanche photodiodes (APDs) are used whereas vacuum photodiodes (VPDs) are used in the end-cap (EE) regions [20].
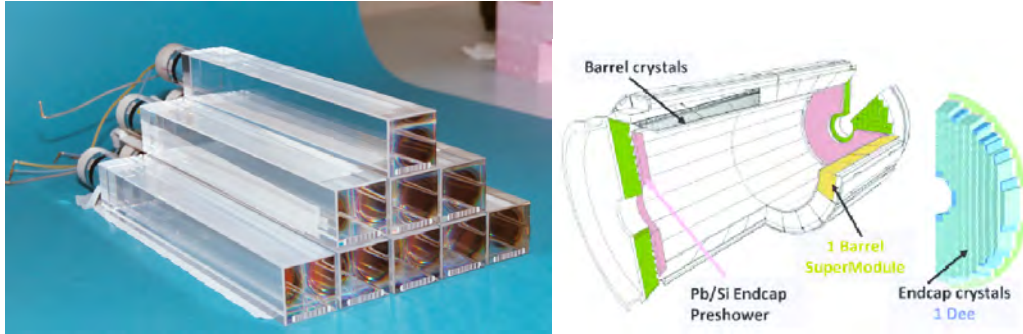
Figure 5.4.6: (a) $PbWO_4$ crystals used in CMS ECAL and (b) layout of CMS ECAL [20].

They are glued to the back of the $PbwO_4$ crystals. The signals are shaped, amplified and digitized by connecting groups of five crystals to electronic boards. The EB is made up of 61200 (5×2) $PbwO_4$ crystals contained in sub-modules which are then contained in modules as shown in Figure 3.4.6. About 4 such modules make up a super module which has a weight of 3.5 t. The EE is made up of superrystals where each supercrystal is a matrix of 5×5 individual crystals. The EE is closed by about 7324 $PbwO_4$ crystals on each side. Each of the two EEs is made up of 312 super-crystals (A half EE is also known as the Dee and is made up of 156 supercrystals) [20]. A preshower detector is located in front of both EEs. They are made of two orthogonal layers of silicon strip detectors lying behind two planes of lead absorbers. The Si sensors have thickness of 320 µm and a pitch of 1.9 mm. The sensors are fitted in micro-modules and each micro-module holds 32 Si strip sensors. The micromodules are connected to a hybrid which contains a pre-amplifier, a shaper and deep analog pipeline memory to store readout data [20].

- **The Hadronic calorimeter (HCAL)**

The next layer of the CMS sub-detector is the Hadronic calorimeter or HCAL. As the name suggests it measures the energies of neutral and charged hadrons e.g neutrons, protons, pions, kaons etc. Like the ECAL, the barrel (HB) and endcap (HE) sections of the CMS HCAL are arranged in a cylindrical form. It is a brass scintillator sampling calorimeter which covers the region upto $|\eta| = 3.0$. A sampling calorimeter uses layers of metal (brass, steel) interleaved with layers of material in which the ionization energy of the traversing particles is measured, the scintillator. This low density scintillator converts the ionization energy to light signals. The scintillation light is then converted via wavelength-shifting (WLS) fibers which are embedded in the scintillator tiles and are connected via channels of clear fibers. The light signals are then detected by hybrid photodiodes (HPDs) which convert these into electrical signals. Most of the HCAL layers are surrounded by the solenoid magnet while some layers also lie outside it, to detect and measure particles from high energy showers.

The scintillator is a type of plastic, most similar in appearance to plexiglass whose 0.3 cm thick layers are interleaved with 5-8 cm thick layers of brass. Like ECAL, the HCAL also has both barrel and endcap components which consist of blocks containing stacks of metal and scintillator. There are 2,592 blocks in the HB and 2,592 in the HEs. The HEs can cover the region upto $|\eta| = 5.0$ [21].

- **The Superconducting magnet**

At the heart of the CMS detector there sits a 13m long having inner diameter of 5.9 m, weighing 12, 000 tonnes and 4T superconducting solenoid which gives the CMS its name in parts. It is made of 40 km (25 miles) long superconducting wire wrapped almost 2,168 times in loops. It passes electric current of 19, 500 A, which in turn generates such huge magnetic field (4T) which is 80,000 times the earth's magnetic field and can store 2.7 GJ of energy. This energy when liberated can melt 18 t of gold. To make the wire superconducting and prevent it from melting under the onslaught of
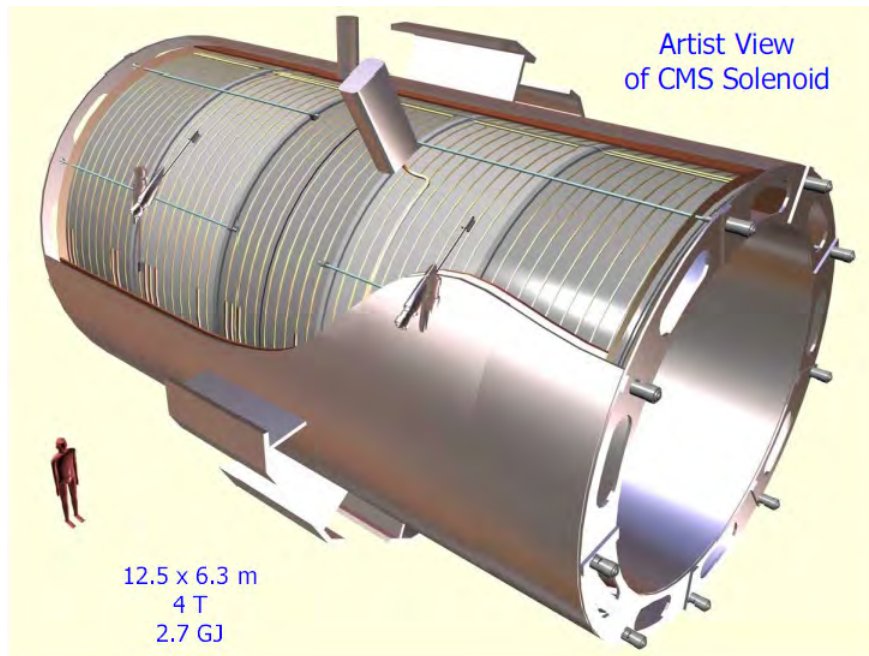
Figure 5.4.7: The CMS superconducting solenoid [21].

such huge amount of electric current and energy, it is cooled to about $-269\ ^{\circ}C$ [21]. The inner tracker records the trajectories of electrically charged particles and in the presence of this magnetic field these charged particles execute curved paths. A typical charged particle moving in a magnetic field B with momentum p has radius of curvature R given to be

$$R = \frac{p}{0.3B} \qquad (5.4.1)$$

The flux of the solenoid is returned by a 1.8 m thick and 10,000 t heavy saturated iron yoke as shown in Figure 5.4.7. Composed of 11 large elements, 5 barrel wheels and 6 endcap discs, the iron yoke is the largest and heaviest component of the CMS detector. It has an important additional role of providing the principal support structure for the calorimeter inside the solenoid and muon detector system outside the solenoid.

- **The Muon Detector**

The final and outermost layer of CMS's sub detectors is the muon detector. It is the CMS largest subdetector and occupies both the barrel and endcap regions. The barrel region consists of three layers which range in radii from 3.5 to 7 m and each layer is 6 m long while the endcap regions have two discs on each side which are 5.5 to 10 m long and have radii of 1.4 to 6.7 m [21].

The muon identification and reconstruction is believed to provide clean signatures for a wide range of physics phenomena as they appear in many important physics processes such as Higgs boson and other predicted new particles. This requires a rich and vigorous muon detection system over the full range of the CMS and the high background rate expected at the LHC experiments. Since the muons have long life-time and high transverse momenta (p_T), they can easily escape most of the inner detectors and can penetrate upto several meters into material, that is why muon detectors are positioned at the outermost surface of the LHC general purpose experiments where muons are the only particles expected to register signals.

The muon detection system consists of three cylindrical layers of muon sub-detectors in the barrel region and two planar endcaps containing 8, 30,000 individual sub-detectors with an effective area of 25,000 m^2 . These sub-detectors are of three types namely

1. Drift Tubes (DT).
2. Cathode Strip Chambers (CSC).
3. Resistive Plate Chambers (RSC).

The return iron yoke has five layers in the barrel region and three in the endcap regions. In the endcaps the CSCs and RPCs are arranged in four discs interleaved with the iron yoke discs. These are ME1, ME2, ME3 and ME4. In the barrel region the RPCs and DTs are arrange in four sub-layers interleaved with iron yoke layers in the form of cocentric cylinders.

5.4.4 The ATLAS Experiment

The Large Hadron Collider (LHC) has two general-purpose detectors, ATLAS being one of them. It examines a wide spectrum of physics, including the Higgs boson, additional dimensions, and particles that could be responsible for dark matter. Although it employs different technological approaches and a different magnet system architecture from the CMS

experiment, it nonetheless pursues the same scientific objectives. Particle beams from the LHC smash at the center of the ATLAS detector, creating collision debris in the form of new particles that shoot out from the collision point in all directions. The trajectories, velocity, and energy of the colliding particles are recorded by six distinct detecting subsystems layered around the collision site, enabling the identification of each particle individually. Charged particles' pathways are bent by a powerful magnet system, enabling the momenta of the particles to be calculated. Figure 5.4.8 shows a computer model of the ATLAS.
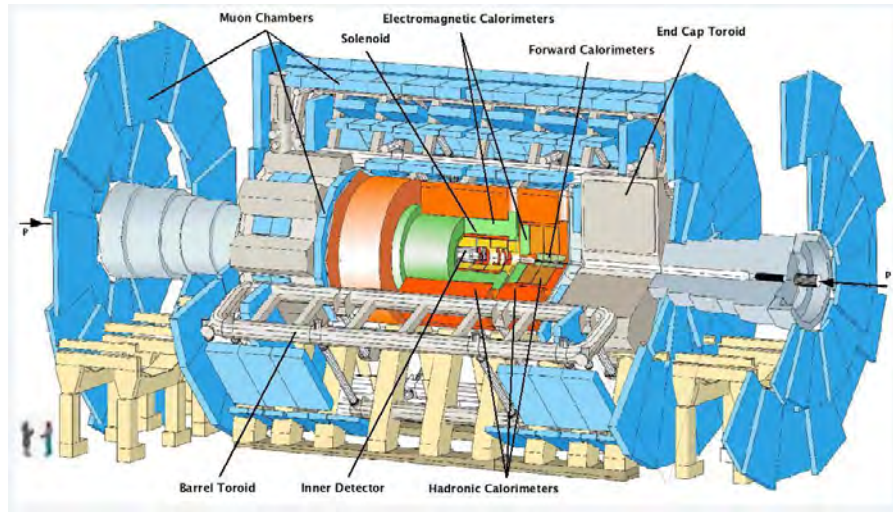

Figure 5.4.8: Computer model of the ATLAS detector at LHC [23].

Chapter 6

CMS Phase-2 Upgrade for Outer Tracker

This chapter primarily focuses on the Phase-2 of the CMS outer tracker upgrade subsystem. It explores various aspects related to the outer tracker modules, including components such as PS modules, the 2S modules, silicon strip sensors, AlCF-bridges, HV pigtails, HV Kapton strips, front-end hybrids, and service hybrids. The chapter provides valuable insights into the crucial upgrades and components essential for the CMS experiment to meet its objectives in the high-luminosity environment of the LHC.

6.1 Luminosity Upgrade Plan for LHC

The search for beyond the Standard Model Physics mainly depends on acquiring large amount of statistical data to find rare processes. It is often not feasible to simply prolong the duration of LHC operation. However, it can become possible by increasing the instantaneous luminosity of LHC. The LHC will undergo considerable improvements to increase the luminosity into a new phase known as the High Luminosity LHC (HL-LHC) in 2026. The HL-LHC project calls for a number of upgrades, including magnets and crab cavities.

The HL-LHC is expected to begin its operations in 2026. The instantaneous luminosity will be 5×10^{34} cm^{-2} s^{-1}, which is a fivefold increase to the original LHC design luminosity. CERN has committed to run the HL-LHC until at least 2037, which will result in the collection of about 3000 fb^{-1} of data over the period of ten year of its operation. The schedule of HL-LHC is shown in Figure 4.1.1.
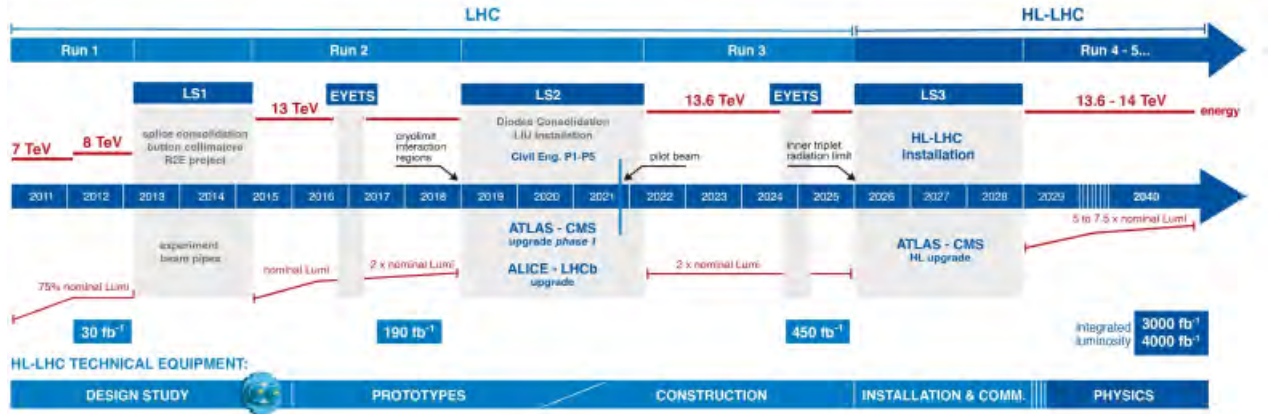
Figure 6.1.1: Schedule of HL-LHC Project.

6.2 The CMS Phase-2 Tracker Upgrade

Due to increase in radiation, the existing tracker cannot cope with the radiation level of HL-LHC. As a result, the existing tracker needs to be replaced by a newer tracker system that should be able to handle the radiation environment of the HL-LHC. The CMS tracker will be upgraded entirely by 2026. Tracker is geometrically distributed in different systems as shown in Figure 6.2.1.

The combination of micro strips, macro pixels, and micro pixels in the inner tracker, particularly in the radial region of less than 200 mm, is crucial for efficient track seeding. It enables precise tracking up to $\eta \approx 4$, along with optimizing the performance of the inner tracker to fully Utilise the capabilities of the HL-LHC experiments.
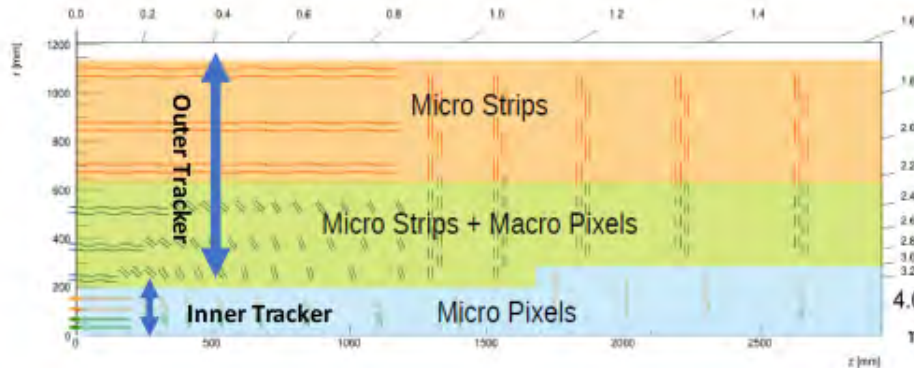
Figure 6.2.1: CMS Outer Tracker layout after upgradation.

In the given Figure 5.2.2. OT is geometrically divided into three parts, the tracker barrel with 2S modules (TB2S), with PS modules (TBPS) and (TEDD)[25].

64

The outer tracker layers, consisting of Pixel-Strip Modules in the radial region of 200 to 600 mm. Strip Modules in the radial region of 600 to 1200 mm, serve a critical role by providing a lever arm for accurate momentum measurement and facilitating the extrapolation of tracks to the calorimeters. It enhances the overall performance and precision of particle tracking and energy measurement in high-energy physics experiments.

The barrel part is made up of six layers, while the end caps are each made up of four discs. In order to lower the material budget, the tracker is almostly made up of light-weight carbon fibre.
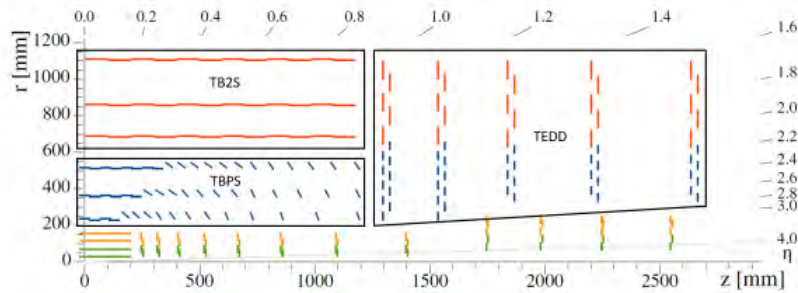
Figure 6.2.2: Outer Tracker layout[26].

6.2.1 Detection Principle

The schematic of a silicon microstrip detector is shown in Figure 6.2.3. The bulk material is p-type, and the implant is n-type material, which forms the PN junction. The p-type implants are capacitively coupled to the readout strip. The voltage is applied across the PN junction by means of a power supply in reverse bias mode. As a result, the PN junction grows until the full volume of the sensor is covered or in other words, the sensor is fully depleted. An ionizing particle penetrates through a fully depleted silicon n-doped slice and generates electron-hole pairs. They then travel towards the respective electrodes as set by the external power supply. The holes drift along the electric field created by the bias voltage to the p^+ doped strips and induce signals on the readout strips, while the electrons drift to the n^+ backplane. The signal is then collected by the readout electronics.
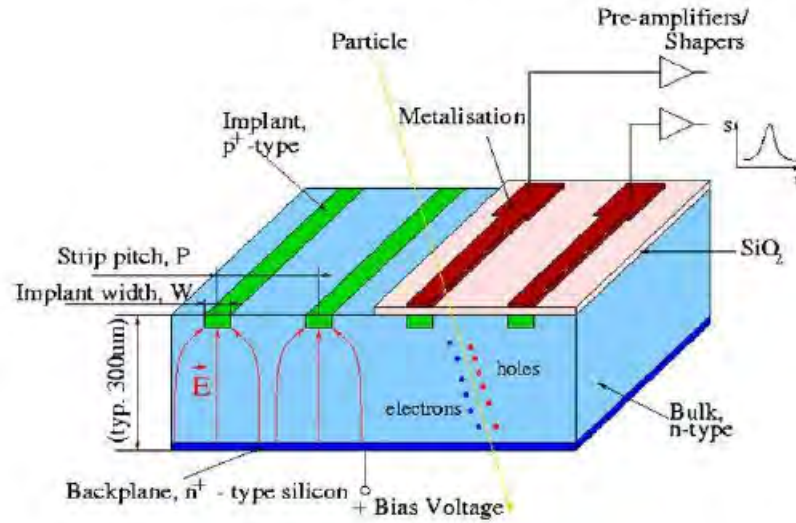
Figure 6.2.3: Exploded view of silicon sensor.

6.3 Outer Tracker Modules

There are two types of modules that make up the outer tracker (OT). One is called PS Module and other is 2S Module. The PS module is composed of a "strip" sensor and a "macro pixel" sensor while the 2S module is composed of two strip sensors. The PS module is the inner component of the OT whereas the 2S modules are placed in the outer section. The PS module has higher resolution than the 2S module. The PS and 2S modules of the OT of the CMS are shown in Figure 6.3.1[34].
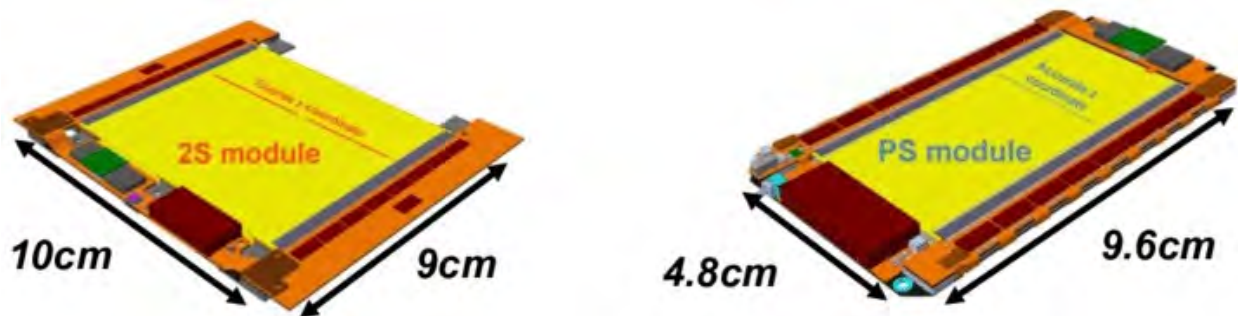
Figure 6.3.1: A sketch of both PS module(right) and 2S module(left).

These two types of modules are known as p_T modules, which are distinguished by their capacity to differentiate high p_T (more than 2 GeV) tracks, greater radiation hardness, im-

proved granularity and track separation, compatibility with higher data rates, and supplying tracking information to level 1 triggers.

Specification	2S Module	PS Module
Sensors	Two Strip sensors	One Strip sensor, one Macro-Pixel
Sensor spacing	1.8 or 4.0 mm	1.6, 2.6, or 4.0 mm
Sensor size	$10 \times 10 \; cm^2$	$5 \times 10 \; cm^2$
Strip size	5 cm $\times$ 90 µm	2.5 cm $\times$ 100 µm
Macro Pixels	0	1.5 mm $\times$ 100 µm
Readout Channels	4064	32128

Table 6.3.1: Specification of 2S and PS Modules.

6.3.1 PS Module

The PS module consists of a silicon micro-strip-sensor divided into two columns of 960 strips and a macro-pixel sensor having 32 x 960 pixels . The PS module has 32128 readout channels built using two types of readout chips. The bottom sensor is pixelated which is read by the Macro Pixel ASIC (MPA) chip. For the top strip sensor, the Short Strip ASIC (SSA) chip reads it through 25 micron wire which is bonded between strips of the sensors and pads of the Front-End Hybrid (FEH). Both PS and 2S modules have a Concentrator-Integrated Circuit (CIC) that collects information from CBCs or MPAs on each FEH. A low-power Gigabit Transceiver (LpGBT) chip transmits this data to the service hybrid. Through the Versatile Transceiver+ (VTRx+), the electrical signal is converted into an optical signal which is then sent to the back-end electronics. The scheme of PS module with FEH hybrid is shown in Figure 6.3.2.
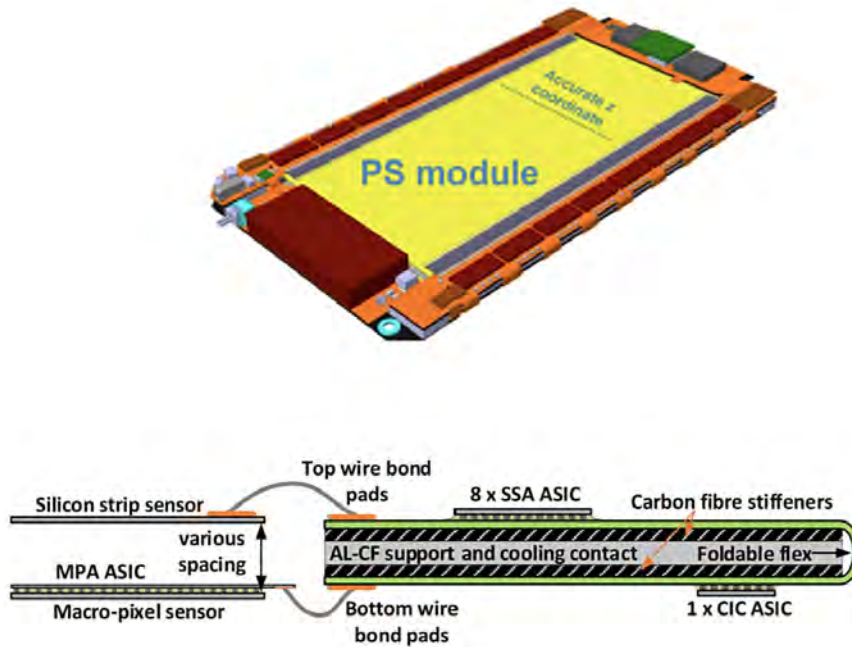
Figure 6.3.2: PS Module with front-end hybrid (FEH).

6.3.2 2S Module

The CMS silicon tracker consists of two tracking devices that operate in a high radiation environment provided by the protons collisions at the LHC. Particle tracking involves reconstructing the path (or track) of charged particles using a tracker. The CMS tracker traces the path of charged particles by measuring their position. In the CMS outer tracker, the silicon strip sensor is one of the two tracking detectors. The 2S module consists of two silicon microstrip sensors separated by a few millimeter distance. The CMS Binary Chip (CBC) is responsible for reading the microstrip sensors. They are fabricated using 130nm CMOS technology. The chip reads two hundred and fifty four strips (127 from the top sensor strip and 127 from the bottom sensor strip). The FEH has 8 CBC chips which read 2032 channels of the module. The 2S modules has 2 FEH which read total of 4064 readout channels. Track stubs are created in a pre-defined time window by matching hits on the top and bottom sensors of the module produced due to the incident particle. Readout data is shared between the CBC and its neighbour chips so that stub detection can be performed across chips. The CBC data is collected by the CIC chip, which is designed in 65nm CMOS technology. In the CIC, the track stub data is evaluated at 40 MHz. The main components of 2S modules are as follow[49] and exploded view is shown in Figure 6.3.3.

- Silicon strip sensor

68

- AlCF bridges

- HV tails

- HV Kapton strips

- Front-end hybrid

- Service hybrid

6.3.3 Silicon Strip Sensor

The 2S module consists of two silicon strip sensors. There are two halves of the silicon sensor comprising of total 2032 strips. Each half of the sensor is segmented with 1016 strips where each strip is 5 cm in length. The strips have a minimum pitch of $90\mu m$ and a minimum width of $22.5\mu m$. The sensor's minimum thickness is $320\mu m$. For the tracker upgrade, it is n-in-p type sensor, i.e., p-type is bulk with n-type implants as shown in Figure 6.3.3. Depending on the sensor width, the depletion voltage for unirradiated sensors varies between 150 V to 300 V. For the silicon strip sensor
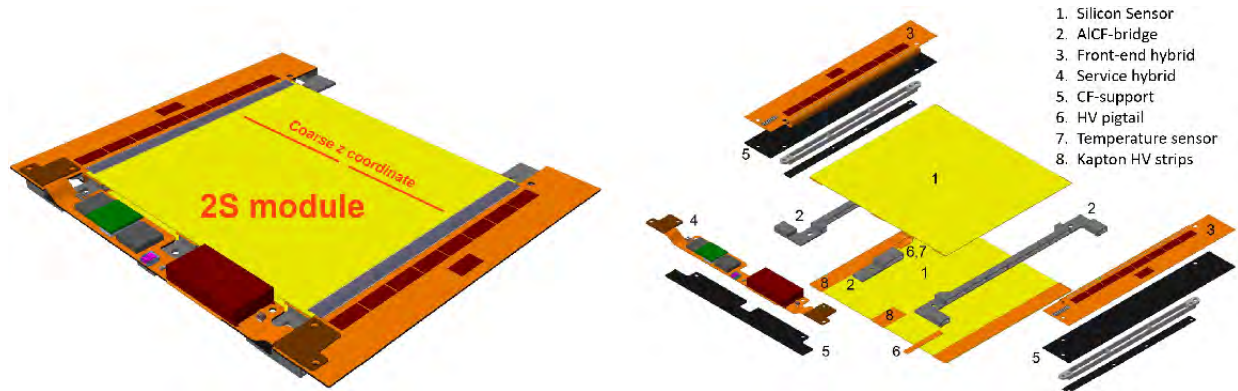
Figure 6.3.3: Assemble 2s module (left), exploded view of 2S Module(right).

to function properly in the HL-LHC environment, specific radiation hardness standards must be met. As a result of phase-2 high luminosity, n-in-p doped silicon is being used as a sensor material because its charge collection efficiency is not as poor after irradiation as p-in-n doped silicon used previously had. Additionally, the strip area is surrounded by three rings. In the silicon sensor, the inner and outer rings are the bias ring and the edge ring, while the centre ring is the guard ring. A potential is provided to the n-doped strip implants by the innermost bias ring, which is connected to the polysilicon resistor[27].

6.3.4 AlCF-Bridges

Each module requires three bridges to keep top and bottom sensors apart with uniform distance. The side bridges are longer in length while the central bridge is smaller in size which is known as the stump bridge. These bridges not only provide the mechanical stability but also serve as vital cooling contacts for dissipation of heat generated by the sensors and electronics during operation. There are two different thickness of the bridges to be used for the 2S module assembly. One are 1.8 mm thick bridges and other are 4 mm thick bridges as shown in the Figure 6.3.4 [27]. Apart from spacing, ALCF-bridges also provide following additional functions.

Figure 6.3.4: Sets of bridges for modules, 4 mm (left) and 1.8 mm (right).

• these bridges serve as the structural support for the rest of the modules.

• Secondly, they contain holes in which the module can be attached to the tracker cooling and support structures and these holes are used during the assembly of the module to position precisely.

The bridges are made of Aluminum Carbon Fiber (ALCF) composite materials which have exceptional thermal conductivity and a low coefficient of thermal expansion (CTE). Silicon sensors have 2.6×10^{-6} CTE [28]. A material's coefficient of thermal expansion (CTE) reduces mechanical stress caused by significant temperature differences between its operating temperature (-30 °C) and assembly temperature (20 °C)[29].

6.3.5 HV Tails

On the backside of sensors, small flexible circuits known as HV tails provide up to 600 volts of depletion voltage to the sensor. The backside of the sensor is coated with aluminum to make a conducting plane. In Figure 6.4.4, the HV tails are illustrated beside the sensor, with the right hand tail pointing to the bottom sensor and the left hand tail pointing to the top sensor. The HV tails are connected to the rear of the sensor using Polytec EP 601 LV epoxy

glue. Then the electrical connection of HV tail is done through wire bonds between the gold pad (a thick piece of soft material) of the tails and the aluminium coated sensor backside. A thermistor is also installed in the HV tail to measure the sensor temperature.

6.3.6   HV Kapton Strips

In order to isolate the sensors from the Al-CF bridges, Polyimide or kapton strips are glued on the backside of the sensors. They are 25-micron thin strips with 0.2 kV/m of dielectric strength, which provides significant insulation. Three kapton strips are used according to the three AlCF bridges on each sensor. The strips are shown in Figure 6.3.5 on the right side.

6.3.7   Front-End Hybrid

The information generated by sensors is processed by front-end hybrids (FEHs). Two front-end hybrids are used in each module. Each FEH is glued to the long AlCF bridge on both sides of the sensor using alignment holes.

Figure 6.3.5: A set of Kapton strips (right) and HV tails for the top and bottom sensor (left).

FEH is connected to the sensor bond pads through wire bonds on both sides of the module for electrical connections [30]. The wire bonds are encapsulated to protect them from damage and resonance vibrations in the CMS magnetic field. There are eight CBCs (CMS Binary Chips) in each front-end hybrid. The CBCs are not just for detecting hits, but also for identifying stubs by matching hits between the bottom and top sensors. In each CBC, there

are 254 channels used to read out 127 strips for the top sensor and 127 strips for the bottom sensor. A bit of hit information and five bits of stub information are transmitted to the Concentrator Integrated Circuit (CIC) from eight CBCs. In each front end hybrid, there is one Concentrator Integrated Circuit (CIC) that integrates the data from the eight CBCs into packets and sends it to the Service Hybrid[31]. The top and bottom side of FEH is shown in Figure 6.3.6.
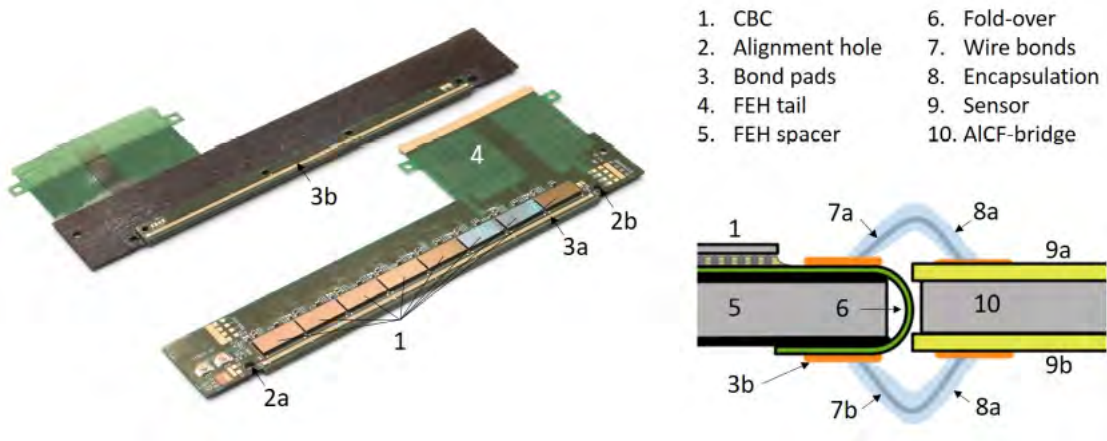
Figure 6.3.6: Top and bottom sides of FEH (left), and cross sectional representation of fold-over area (right).

6.3.8 Service Hybrid

In each module, there is a service hybrid (SEH) that supplies power and transmits data to the back end electronics. It is made from a 4-layer flexible polyimide circuit laminated to a CF stiffener. For data transmission, the service hybrid (SEH) uses a LpGBT (Low-power Gigabit Transceiver), which aggregates the data from the two CICs and serializes it [32]. Versatile Transceiver plus (VTRx+) is also incorporated into the service hybrid (SEH), which transmits data from electrical signals to optical signals. To transfer optical signals to the back-end, an optical fibre is used. In order to minimize power losses, the SEH utilizes two step-down DC converters.

Figure 6.3.7: Top and bottom sides of service hybrid (SEH).

Chapter 7

Assembly of 2S module

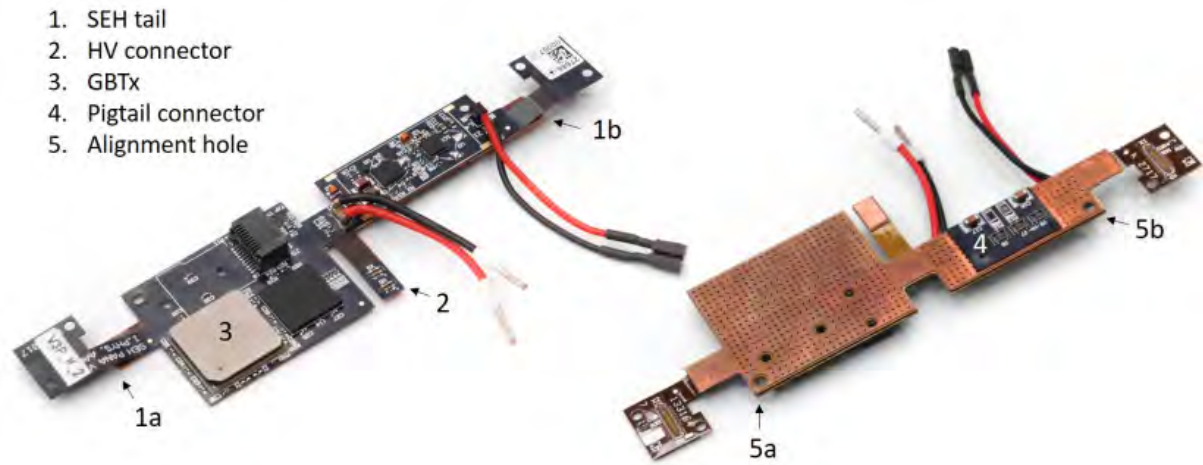In this chapter, the procedure of 2S module assembly and relevant required equipments are described. The results at various stages of the assembly are also discussed.

7.1 Assembly Prerequisites

The assembly of 2S module is done in the clean room with controlled environment. The temperature should be 23 °C and relative humidity should be around 42%. The performance of silicon sensors is directly affected by temperature and relative humidity.

7.1.1 Clean Room

It is crucial to have a cleanroom large enough to construct the 2S module . To work in the clearoom, the workers all obliged to use the items like jackets, masks, gloves and hairnets. The Temperature, humidity and the particle counts must all be regularly measured and recorded in a cleanroom. Following are the main items required for module assembly.

- **Sensor Storage Cabinet:** A specialized cabinet used to maintain a controlled environment while storing sensors or sensor components to protect them from enviromental effects.

- **Glue Mixer (SmartMix X2):** During the assembly process, adhesives and glues are mixed using the SmartMix X2 machine.

- **Glueing Robot:** A robot that automatically and accurately positions the adhesive to the necessary components for accurate and reliable glueing.

- **Dispenser:** Machine that controls the required amount of dispensing adhesive or glues .

- **DP Probe Station:** The bare sensors are tested using probe station. It supports the automatized testing of various parameters of the sensors.

- **PC:** A computer is used to interface with variuos eqiupments such as robot ,dispenser or probe station system .

- **Wire Bonding Machine:** This machine establishes the electrical connections between silicon sensor strips and front-end hybrid using 25 micron thin wire made of aluminium-silicon alloy.

- **Jigs:** Different types of jigs are used for each assembly step of the 2S module. These are structures which are prepared through machining of metallic pieces. They are used to assist in achieving precision and repeatability of assembly steps like positioning and guiding of module components.

The NCP cleanroom is shown in Figure 7.1.1.

Figure 7.1.1: NCP clean room.

7.2 Tracker 2S Module Assembly Step

The construction of the 2S module as illustrated in Figure 7.2.1, involves several stages. In the first step, the sensor dicing and IV is measured. Then the Kapton strips are glued to the back plane of the sensor. The HV tails are then glued and wire-bonded. The HV tail wire-bonds are protected with Sylgard 186 adhesive. In the bare module assembly, sensors and Al-CF bridges are placed and glued to make sandwich. Then the SEH and FEHs are glued to the bare module. The 4064 wire-bonds are employed using wire bonding machine

to connect sensor readout strips to the FEH channels. The wire bonds are encapsulated by Sylgard 186 glue at the end.
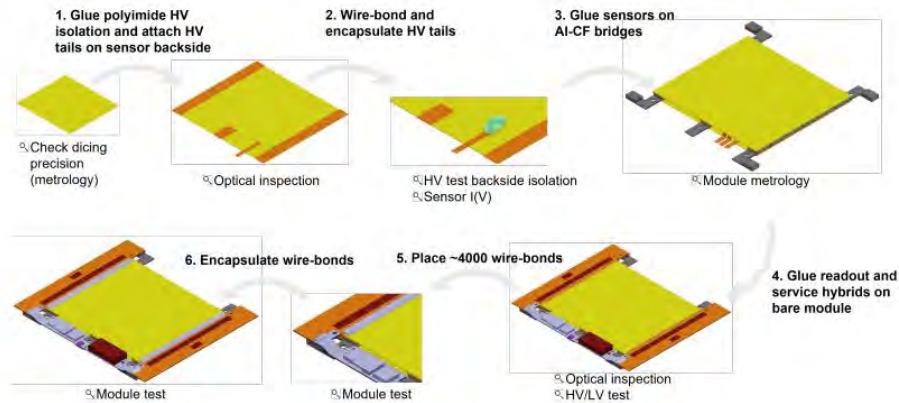

Figure 7.2.1: Tracker 2S module assembly steps.

7.2.1 Bare Module Assembly

The various steps of 2S module assembly stages at NCP is shown in Figure 7.2.2. First of all the silicon sensor dicing accuracy is checked by using microscope of the metrology station. Then kapton strips are glued with Polytec EP 601 LV adhesive by using a dispensing comprised of a 3-axis robot and volumetric dispenser. The resin-hardener ratio of the glue is set to 100:35 by weight and cures after 4 hours at room temperature. The robot sets the coordinates of the dispensing gun on the sensor. An electric motor is coupled to a plunger of the dispensing gun which drives the piston to push the glue inside the syringe. The pressure inside the syringe containg glue is increased until the glue is finally ejected. The various components of gluing are shown in the Figure 7.2.3
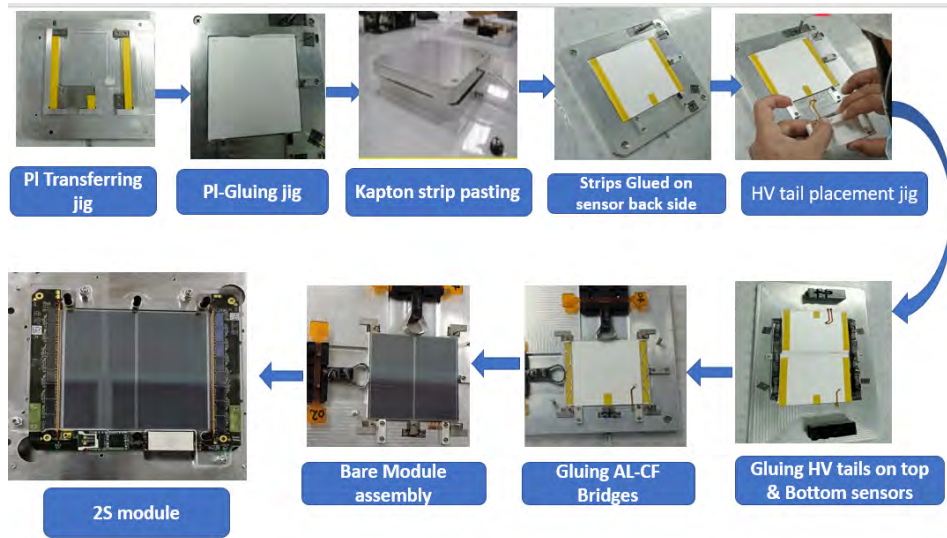
Figure 7.2.2: 2S module assembly steps.
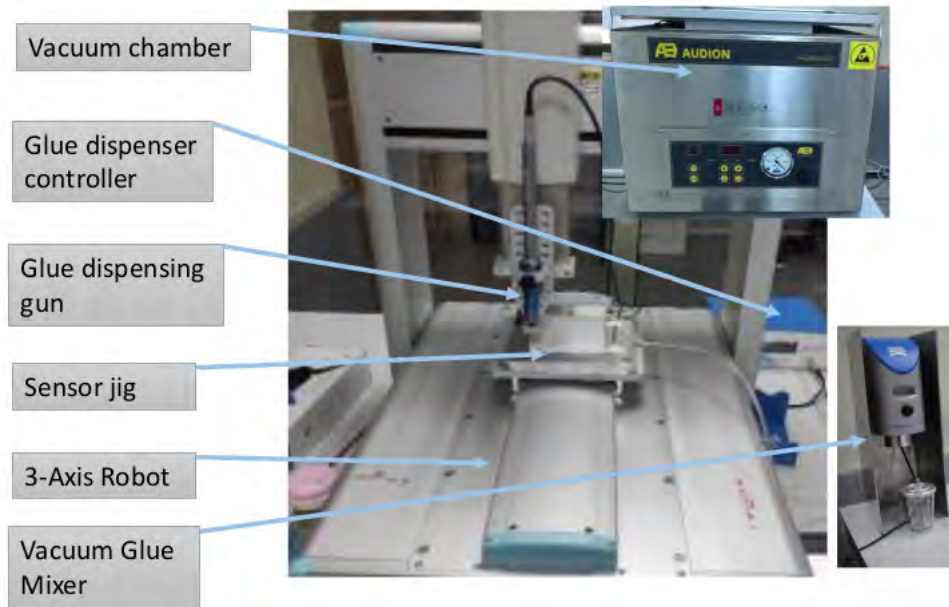
Figure 7.2.3: Various compnents of glueing setup.

Once the glue is dispensed on the sensor backplane then the kapton strips are placed using kapton gluing jig. At the same time, HV tail is glued on the backside of the sensor. Once the glue is cured after 24 hours, the HV tail is wirebonded and encapsulated. After this the sensors are sandwiched to make bare module by using sensor gluing jig. The space between the sensors is maintained by the Aluminum Carbon Fiber (Al-CF) spacers. On the sensor gluing jig, the first sensor is mounted face down. The Al-CF bridges are visually inspected

and painted with glue by using glue transfer jig. For this purpose, Polytec TC437 with a resin-hardener ratio of 100:10 is used. The glue cures in 2 hours after the application at room temperature. After curing of the glue, the bare module is checked for top and bottom sensor alignment.

7.3   Metrology of the Bare Module

The main objective of metrology is to check the sensors alignment. It is important to align top and bottom sensors strip-to-strip during assembly to maintain its function to work properly as a p_T module. The concept of p_T-trigger modules is to discriminate the low and high momentum particles, which breaks down if sensors are misaligned by more than 400 µrad in rotation. In addition, the relative displacement of top and bottom sensors along the strips and perpendicular to the strips must be less than 100 µm and 50 µm, respectively.

7.3.1   Needle Method

In the needle method, the bare module is placed on the module carriage jig and four needles are firmly attached to the module carrier jig near sensor corner, where they are visible from both sides (top and bottom) in the microscope as shown in Figure 7.3.1. The coordinates of the needle top and bottom sensors alignment along the strips are Δy and those perpendicular to the strips are Δx . The relative displacement and angle of rotation ($\Delta\theta$) is calculated for top and bottom sensors from the needle frame of reference. The rotation ($\Delta\theta$) is -31.32 μrad and the displacement Δx and Δy are -0.759 µm -9.433 µm respectivley .The results are within the required specification.
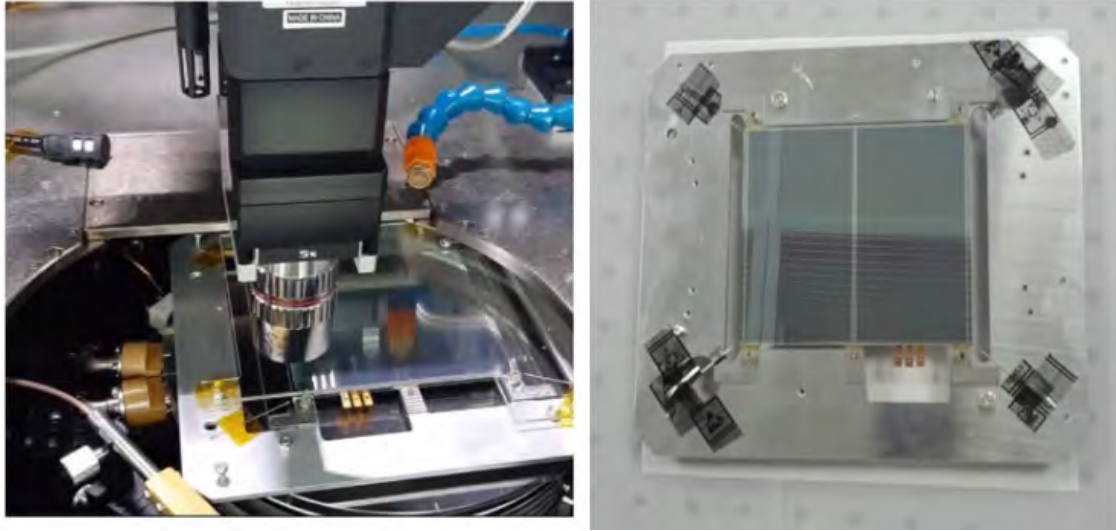
Figure 7.3.1: (Left) Probe Station (MPI TS2000-DP) with bare module (Right) bare modul carrier jig with reference of four needles.

7.3.2 Hybrid Assembly

Hybrids are multi layers printed circuit board carrying readouts chips, power chips, resistor, capacitor, and connecter. The FEH hybrids carry binary chips used to readout the signal from the sensors. The service hybrid (SEH) is used to power up the sensors and FEH. It is also used to transfer data from FEH to backend electronics. The assembly of hybrids to the bare module involves critical steps to ensure precise pad to pad alignment. In the initial stage, the hybrids are linked together to form the skeleton of SEH and FEH. This skeleton is connected to the bare module by ensuring accurate positioning under the microscope and using aligmnent pin of the hybrid assembly jig. In order to align the sensor and hybrid components properly, these alignment pins serve as reference points. The hybrids skeleton is glued to the bare module by using a specialized adhesive known as Polytec TC 437 glue. The skeleton assembly process requires a specific spacing of 100 micrometers between the sensor and the hybrid. This spacing is critical for optimal performance and also to prevent electrical issues between the two components during assembly as shown in Figure 7.3.2.
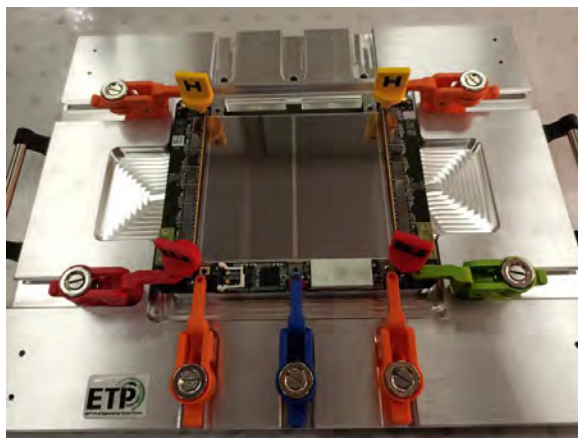
Figure 7.3.2: Assembly of hybrid.

7.3.3 Wire Bonding and Encapsulation

The wire bonds are made by using Delvotec G5 64000 wire bonding machine. The wire bond with a height of < 500 μm is made between HV tail bond pad and sensor backside for biasing of the sensor. This machine can achieve a speed of 2 to 3 wires per second (depending on the application) using fine wire with a diameter of 25 μm. The two FEH left and right HYBRID are conneted to the sensor by making 4064 wire bonds per module. For each HV tail, 14 wire bonds are made as shown in Figure 7.3.3.
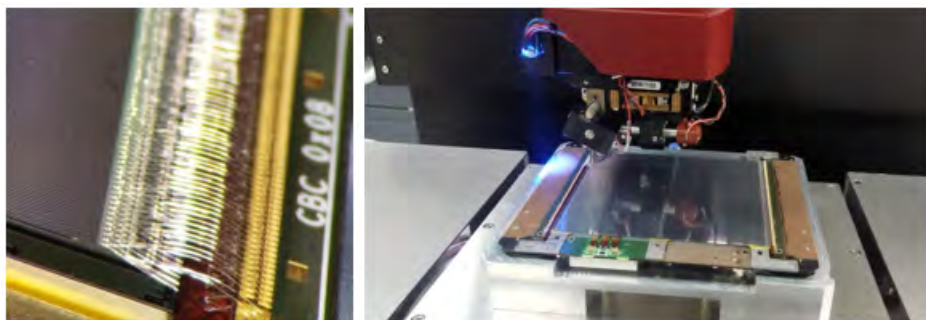
Figure 7.3.3: (Left) Wire bonds between sensor and hybrid (Right) module on wire bonding machine.

To safeguard the wire bonds, a protective encapsulation is employed, utilizing Sylgard 186 elastomer, which forms a spiral with six lines positioned 1 mm above the sensor, with an application of 0.55 g of silicone elastomer per wire-bond row as shown in Figure 7.3.4. The fully assembled 2S functional module is shown in the Figure 7.3.5.
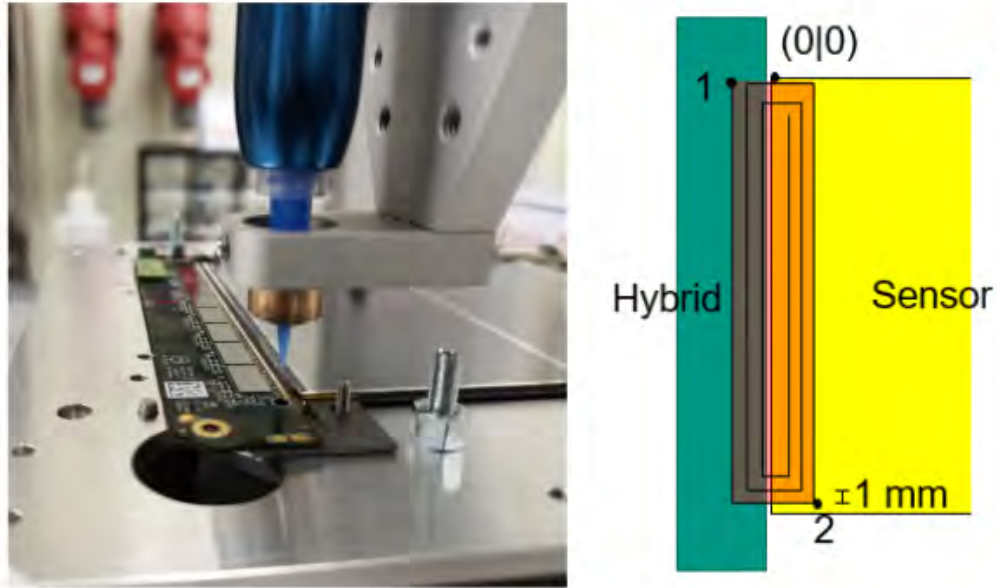
Figure 7.3.4: Encapsulation of wire bonds.

Figure 7.3.5: 2S Silicon functional module.

7.3.4 Positioning Measurement of Kapton Strips

The kapton strips are glued to the back side of the sensors. These strips are 25 micron thin and used to electrically isolate the sensor from the Al-CF bridges. Hence, their positioning on the sensors are important and is checked measured after their placement. These strips have also good thermal conductivity ($\lambda \approx 0.75$ W $m^{-1}k^{-1}$) to take away heat from the sensors. Due to three Al-CF bridges, each sensor utilizes three kapton strips as shown in Figure 5.3.6.
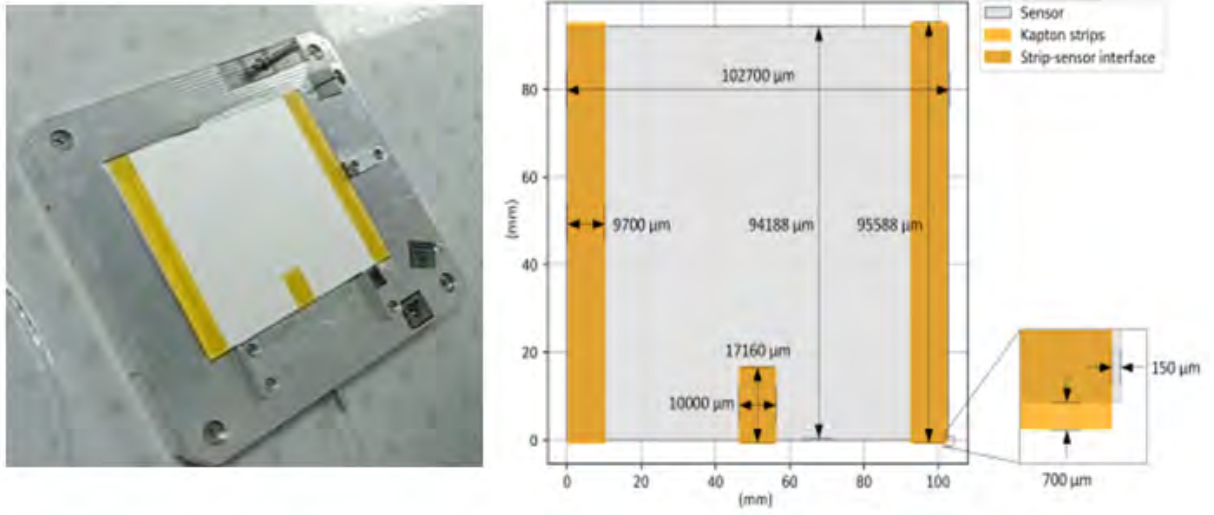
Figure 7.3.6: **(left)** Kapton strips glued to the sensor backside . **(Right)** Strip position with respect to sensor.

The left and right kapton strips are 95.68 mm long and 9.8 mm wide. The size of the silicon sensor is 94.183 mm in length and 102.700 mm in width. The middle short strips are 17.26 mm long and 10.1 mm wide. It is important to place the strips accurately on the sensors so that the AL-CF bridges are properly insulated from the sensors.

7.3.5 Measurment Results of the Positioning of Kapton strips

The distance between the sensor's edge and the Kapton strips is measure using the microscope. The measurement is done at five points for the top and bottom sensors as shown in the Figure 7.3.7.

Figure 7.3.7: Kapton strips position with respect to the sensor edge [33].

The limits along the x and y-axes values of the kapton strips from the sensor edges are 150 ± 150 µm and 700 ± 200 µm, respectively. In table 7.3.1, the measured values are shown which meet the requirement.
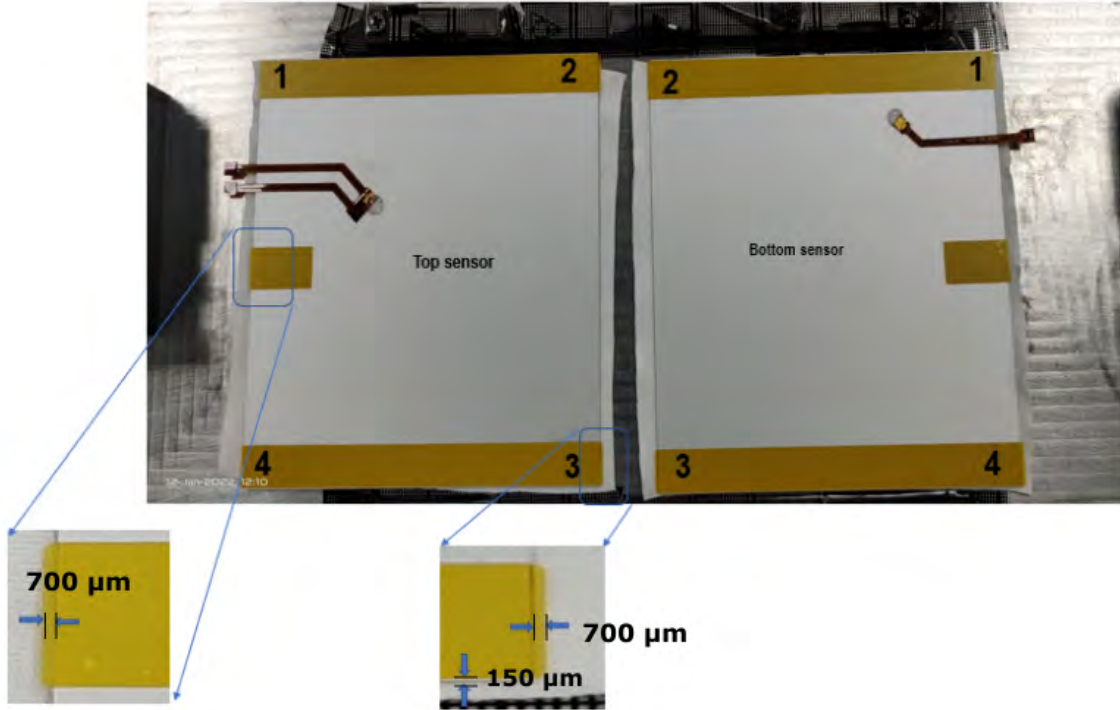
Ref.point(a)	X(µm)	Y(µm)	R.point(b)	X(µm)	Y(µm)
1	109	691	1	200	800
2	127	782	2	184	691
3	145	727	3	164	745
4	218	745	4	109	745
5	//	711	5	//	691
Required values	150 ± 150	700 ± 200	Required values	150 ± 150	700 ± 200

Table 7.3.1: **(a)** Results of the positioning measurement of kapton strips for top sensor and **(b)** for bottom sensor.

The blue lines reflect the necessary limit of kapton strip separation from sensor edge along the y-axis, which is 500 µm to 900 µm. Along the x-axis, the limit is 0 to 300 µm. All the values related to the positioning of kapton strips are within the required range. The top and bottom sensor strips position from the sensor edge along the y-axis and x-axis, respectively as shown in Figures 7.3.8 and 7.3.9.
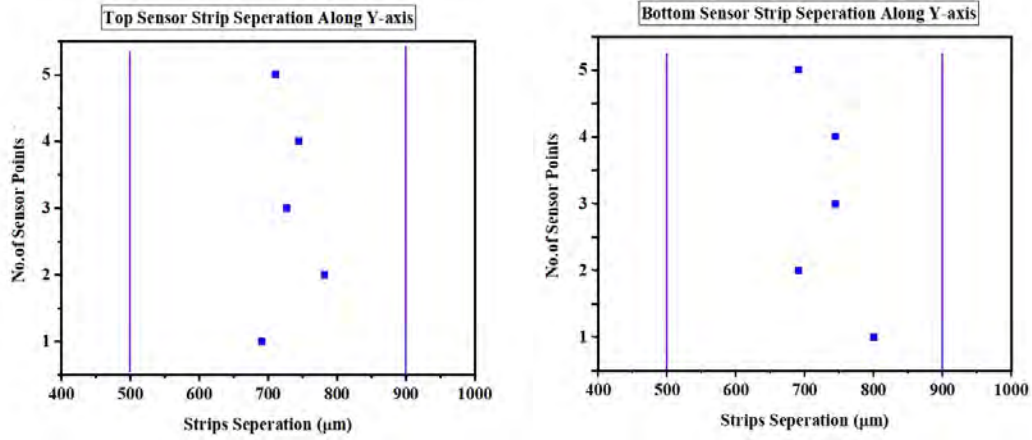
Figure 7.3.8: Top and bottom sensors strips position along y-axis.
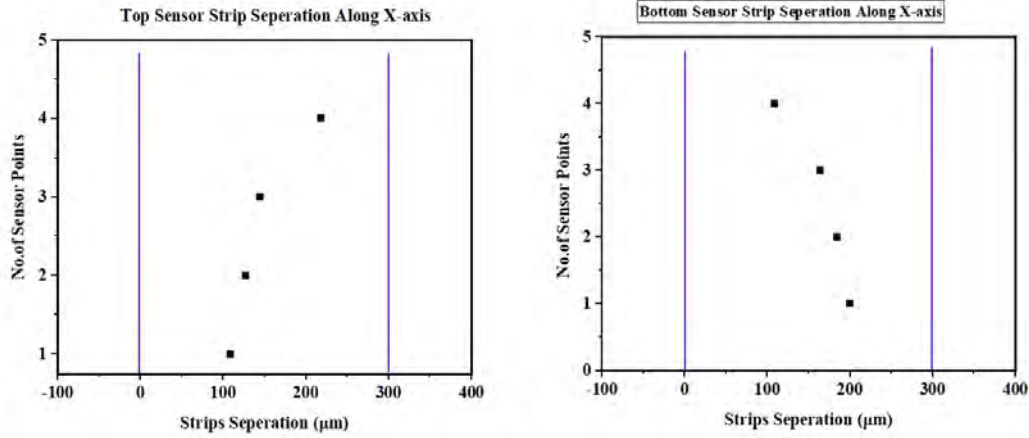
Figure 7.3.9: Top and bottom sensors strips position along x-axis.

7.3.6   Positioning Measurement of HV Tails

During the assembly, the HV tails are attached to the sensor's backplane and must be positioned precisely so that it can be connected to the service hybrid (SEH). Along the x and y-axes, the top sensor should be at 25.955 mm and 33.62 mm as shown in Figure 5.3.10. The HV tail position values for the bottom sensor along the x and y-axes should be 21.155 mm and 28.06 mm respectivelys. The measured value are shown in the Table 7.3.2. They are all very close to the required value.

Measured value	26.255	33.510	Measured value	21.51	28.25
Required values	25.955	33.62	Required values	21.155	28.06

Table 7.3.2: (left) Results for top sensor (Right) results for bottom sensor.

84
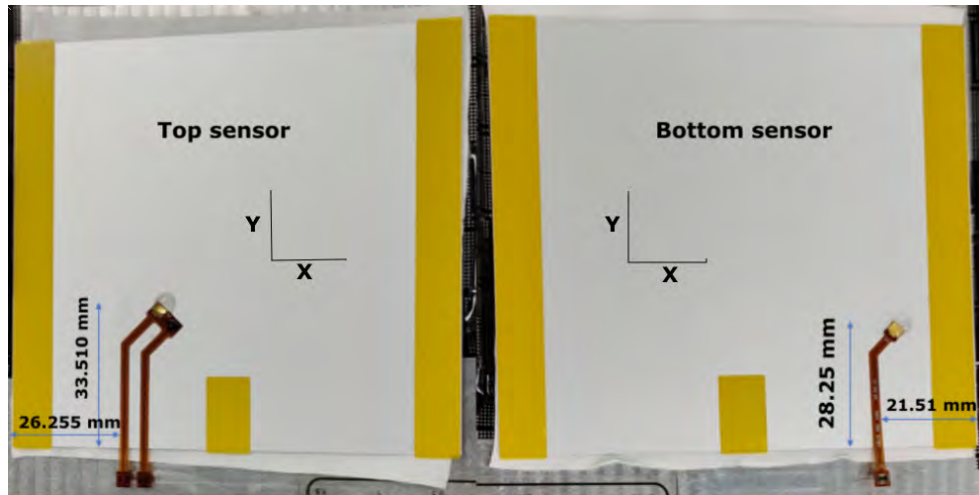
Figure 7.3.10: The actual position and dimensions of HV tails with respect to a sensor edge.

7.3.7 Sensors IV Measurements during Assembly

The voltage current characterisitics of the sensors must be checked at different assembly steps to ensure the quality of the sensors. In order to measure IV, the sensors are made reverse biased by applying negative potential to the sensor backplane and the bias ring is kept at ground voltage. The leakage curent is then recorded by increasing the volts. The IV curves measured for bare sensors, after kapton and HV tail gluing and after bare module assembly are shown in the Figure 7.3.11 and 7.3.12 for botton and top sensors respectively. The results shown no abnormal behaviour which confirm no damage to the sensors during assembly.

Figure 7.3.11: IV measurements of bottom sensor during assembly are taken to validate the assembly steps.

Figure 7.3.12: IV measurements of top sensor after each assembly step are taken to validate the assembly steps.

Chapter 8

Conclusion
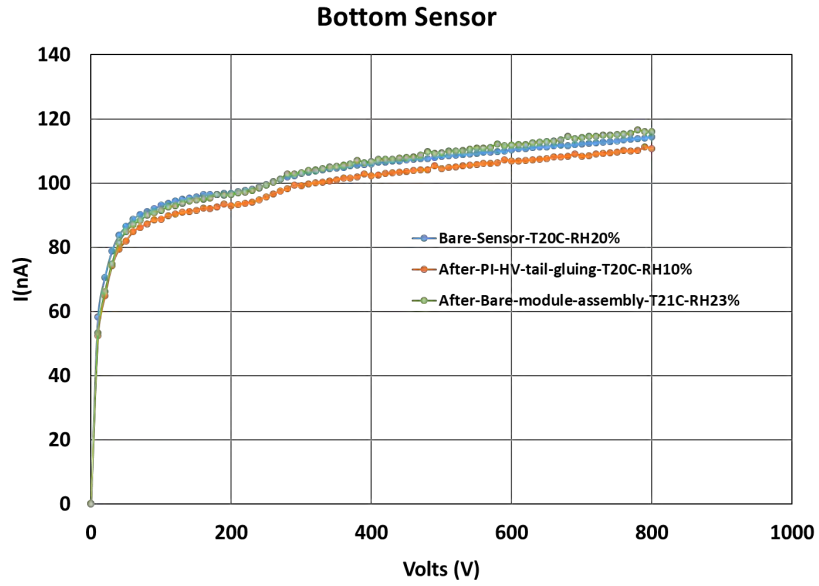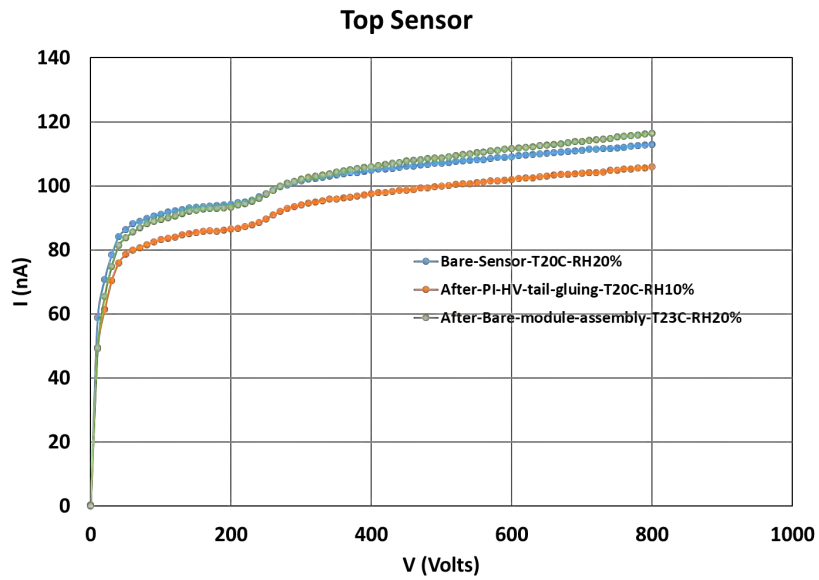
The results of the ALICE experiment, which measured the antibaryon-to-baryon ratio in proton-proton collisions, were presented in the last chapter.

Three different LHC energies $\sqrt{s}=$ 900 GeV, 2.76 TeV, 7 TeV, and 13 Tev were used to analyse data from proton-proton collisions. Emphasis is placed on how the antibaryon-to-baryon ratio depends on the charged particle multiplicity, transverse momentum, and rapidity. Additionally, the rapidity interval dependency were examined. A number of Monte Carlo forecasts were compared with the experimental data.

As a function of p_T and y at the LHC energies, the $\overline{B}/B$ ($\overline{p}/p$, $\overline{\Lambda}/\Lambda$, and $\overline{\Xi}^+/\Xi^-$) ratios are provided that were obtained using the different model simulations outlined in section 7.3. The ALICE data exhibits no p_T dependency, and the $\overline{p}/p$ ratio is almost constant at 0.95 across all p_T bins. In contrast, the DPMJET-III, Pythia8, and EPOS1.99 models do not exhibit any p_T dependency while correctly reproducing the data patterns. However, for larger p_T bins ($p_T > 0.7$ GeV/c), the EPOS-LHC model somewhat overpredicts the ratio.

Starting in 2026, the HL-LHC will operate at luminosities five times higher than the LHC's design luminosity (L = 1×10^{34} $cm^{-2}s^{-1}$). This will result in higher particle rates inside the experiments. To adapt to the new HL-LHC environment, the CMS detector will need to undergo major changes. In the Phase 2 Upgrade, which will be done for the HL-LHC, the current CMS silicon tracker will be entirely replaced. The new tracker will have inner and exterior trackers as its two components. Two silicon strip sensors will be housed in a 2S-module that makes up the exterior tracker. The inside tracker will be made up of a PS-module loaded with silicon strip- and macro-pixel sensors. The module's purpose is to provide tracking data to the CMS L1 trigger. Each Outer Tracker module for level-1 trigger needs to separates passing charged particles based on their transverse momentum ($>$2GeV). For the new p_T trigger module concept during phase-2-upgrade of the CMS outer-tracker, 2 silicon sensors in each module are required that are closely distanced from one another. Because

the trajectories are less curved in the strong B (magnetic field) than the low "transverse-momentum" (p_T) charged particles, the particles with more transverse momentum (p_T) that is greater than 2 GeV will penetrate the two sensors layers in a straight path. The top and bottom sensors' strip to strip alignment is crucial for the proper operation of p_T- modules. If there is a sensor misalignment of greater than 400 μrad, the p_T-module idea fails. The x and y axes are translated by 100 μm and 50 μm, respectively. Therefore, metrology is carried out to verify the misalignment of bare modules using the needle method and a metrology station (MPI TS2000 Probe System). Kapton strips and HV tails' locations are measured with the aid of metrology. The efficient operation of this p_T mechanism depends on the module's flawless assembly. For electrical isolation between two sensors, Kapton strips are utilized. Kapton strip HV tail placement and measurement accuracy are essential. In order to establish an electrical connection between the HV tails and the sensor backside, the HV tails must be positioned precisely in relation to the service end hybrid (SEH). The real Kapton strip placement values along the x and y axes are 150±150. and, 700±200 respectively. The top sensor must have values of 25.955 mm and 33.62 mm along the x and y axes, respectively. Additionally, the x and y axes of the bottom sensor should be 21.155 mm and 28.06 mm, respectively. The results of the calculations show that each of these values complies with the requirements. The average values obtained using the needle approach are, respectively, -31.32 μrad for rotation, the displacement Δx and Δy are -0.759 µm -9.433 µm respectivley. All of these outcomes fall inside the given parameters. This study helps us figure out how to best use 2S modules in high-energy physics studies and learn more about them.

Bibliography

[1] ATLAS Collaboration. Technical proposal: A high-granularity timing detector for the ATLAS phase-ii upgrade. Technical report, 2018.

[2] François Englert and Peter W Higgs. The nobel prize in physics 2013. In spin, volume 1, page 2, 2013.

[3] Tom WB Kibble. The Standard model of particle physics. arXiv preprint arXiv:1412.4094, 2014.

[4] Brian R Martin and Graham Shaw. Nuclear and particle physics: an introduction. John Wiley & Sons, 2019.

[5] Kei-Ichi Kondo. Gauge-independent brout–englert–higgs mechanism and yang–mills theory with a gauge-invariant gluon mass term. The European Physical Journal C, 78(7):577, 2018.

[6] David Griffiths. Introduction to elementary particles. John Wiley & Sons, 2020.

[7] Niels Walet. The basic building blocks for qcd feynman diagrams, 2010. URL https://oer.physics.manchester.ac.uk.

[8] Alexander Belyaev and Douglas Ross. Weak Interactions, pages 267–282. Springer International Publishing, Cham, 2021.

[9] Th Kaluza. On the unification problem in physics. arXiv preprint arXiv:1803.08616, 2018.

[10] Yoichiro Nambu and Nobel Lecture. Spontaneous symmetry breaking in particle physics: a case of cross fertilization, 2008.

[11] Jeremy Bernstein. Spontaneous symmetry breaking, gauge theories, the higgs mechanism and all that. Rev. Mod. Phys., 46(1):7, 1974.

[12] M Concepción González-Garciá and Yosef Nir. "Neutrino masses and mixing: evidence and impli- cations". In: Reviews of Modern Physics 75.2 (2003), p. 345.

[13] Ed Daw. Lecture 7 rapidity and pseudorapidity. URL http://www. hep. shef. ac. uk/edaw/PHY206/Site/2012 course files/phy206rlec7. pdf, 2012.

[14] Fu-Hu Liu, Ya-Hui Chen, Ya-Qin Gao, and Er-Qin Wang. On current conversion between particle rapidity and pseudorapidity distributions in high energy collisions. Adv. High Energy Phys., 2013, 2013.

[15] Klaus Wille. The physics of particle accelerators: an introduction. Clarendon Press, 2000.

[16] Edmund Wilson, Edward JN Wilson, and EJN Wilson. An introduction to particle accelerators. Clarendon Press, 2001.

[17] Esma Mobs. The CERN accelerator complex-august 2018. Technical re- port, 2018.

[18] Frank Zimmermann. He-lhc overview, parameters and challenges. ICFA Beam Dyn. Newsl., 72:138–141, 2017.

[19] Kenneth Aamodt, A Abrahantes Quintana, R Achenbach, S Acou- nis, D Adamová, C Adler, M Aggarwal, F Agnese, G Aglieri Rinella, Z Ahammed, et al. The ALICE experiment at the cern lhc. J. Instrum, 3(08):S08002, 2008.

[20] CMS Collaboration, S Chatrchyan, G Hmayakyan, V Khachatryan, AM Sirunyan, W Adam, T Bauer, T Bergauer, H Bergauer, M Dragice- vic, et al. The CMS experiment at the CERN lhc, 2008.

[21] Serguei Chatrchyan, G Hmayakyan, V Khachatryan, CMS Collabora- tion, et al. The CMS experiment at the CERN LHC. J. Instrum, 3(8):S08004, 2008.

[22] Roman Adolphi et al. The CMS experiment at the CERN LHC. J. Instrum, 803:S08004, 2008.

[23] Georges Aad, JM Butterworth, J Thion, U Bratzler, PN Ratoff, RB Nickerson, JM Seixas, I Grabowska-Bold, F Meisel, S Lokwitz, et al. The ATLAS experiment at the CERN large hadron collider. J. Instrum, 3:S08003, 2008.

[24] Stella Orfanelli, CMS collaboration, et al. "The phase 2 upgrade of the CMS inner tracker". In: Nuclear Instruments and Methods in Physics Research Section A: Acceler- ators, Spectrometers, Detectors and Associated Equipment 980 (2020), p. 164396

[25] Antonio Cassese. "SISSA: Powering of the CMS Phase-2 Upgraded Tracker". In: PoS 370 (2020), p. 066.

[26] Kevin Connor Nash. The Phase-2 Upgrade of the CMS Outer Tracker. Tech. rep. 2021.

[27] Nicolas Maximilian Rowert. "Assembly and Characterization of a First Functional 2S Module for the CMS Phase-2 Upgrade at LHC". PhD thesis. Rheinisch Westfaelische Tech. Hoch.(DE), 2017.

[28] Stefan Maier. "Assembly and qualification procedures of 2S modules and high rate tests of the CMS Binary Chip for the Phase 2 Upgrade of the CMS Outer Tracker". In: (2019).

[29] Jeroen Guido Hegeman. The CMS Data Acquisition System for the Phase-2 Upgrade. Tech. rep. 2018.

[30] Jean-Marc André et al. "The CMS Data Acquisition System for the Phase-2 Upgrade". In: arXiv preprint arXiv:1806.08975 (2018).

[31] Benedetta Nodari et al. A 65 nm Data Concentration ASIC for the CMS Outer Tracker Detector Upgrade at HL-LHC. Tech. rep. 2018.

[32] Stefan Biereigel et al. "SISSA: The lpGBT PLL and CDR Architecture, Performance and SEE Robustness". In: PoS (2020), p. 034.

[33] Nicolas Maximilian Rowert. "Assembly and Characterization of a First Functional 2S Module for the CMS Phase-2 Upgrade at LHC". PhD thesis. Rheinisch Westfaelische Tech. Hoch.(DE), 2017.

[34] CMS collaboration et al. "The phase-2 upgrade of the CMS tracker". In: CMS-TDR-014 (2017).

[35] A. Casher, H. Neuberger and S. Nussinov, Phys. Rev. D20 (1980) 179.

[36] D. B. Lichtenberg and L. J. Tassie, Phys. Rev. 155, 1601 (1967).

[37] E. Gotsman and S. Nussinov, Phys. Rev. D 22 (1980) 624.

[38] B. I. Abelev et al. (STAR Collaboration), Phys. Rev. C 75 (2007) 64901.

[39] David J Earl and Michael W Deem. Monte carlo simulations. In Molecular modeling of proteins, pages 25–36. Springer, 2008.

[40] Robert L Harrison. Introduction to monte carlo simulation. In AIP conference proceedings, volume 1204, pages 17–21. American Institute of Physics, 2010.

[41] Torbjörn Sjöstrand, Stefan Ask, Jesper R Christiansen, Richard Corke, Nishita Desai, Philip Ilten, Stephen Mrenna, Stefan Prestel, Christine O Ras- mussen, and Peter Z Skands. An introduction to pythia 8.2. Computer physics communications, 191:159–177, 2015.

[42] Alexandru Cătălin Ene, JIPA Alexandru, and Lavinia-Elena Giubega. Study of monte carlo event generators for proton-proton collisions at lhc energies in the forward region. Chinese Physics C, 43(8):083001, 2019.

[43] H. J. Drescher, M. Hladik, S. Ostapchenko, T. Pierog and K. Werner, Phys. Rept. 350 (2001), 93-289 doi:10.1016/S0370-1573(00)00122-8 [arXiv:hep-ph/0007198 [hep-ph]].

[44] T. Pierog and K. Werner, Nucl. Phys. B Proc. doi:10.1016/j.nuclphysbps.2009.09.017 [arXiv:0905.1198 [hep-ph]]. 34 [41] S. Forte and S. Carrazza, [arXiv:2008.12305 [hep-ph]].

[45] T. Pierog, I. Karpenko, J. M. Katzy, E. Yatsenko and K. Werner, Phys. Rev. C 92 (2015) no.3, 034906 doi:10.1103/PhysRevC.92.034906 [arXiv:1306.0121 [hep-ph]].

[46] S. Roesler, R. Engel and J. Ranft, doi:10.1007/978-3-642-18211-2 166 [arXiv:hep-ph/0012252 [hep-ph]].

[47] E. Abbas et al. [ALICE], Eur. Phys. J. C 73, 2496 (2013) doi:10.1140/epjc/s10052-013-2496-5 [arXiv:1305.1562 [nucl-ex]].

[48] Ashraf, M.U., Tariq, J., Ikram, S., Khan, A.M., Butt, J. and Zain, S., 2023. Study of baryon number transport using model simulations in pp collisions at LHC energies. The European Physical Journal Plus, 138(7), pp.1-11.

[49] Jeroen Guido Hegeman. The CMS Data Acquisition System for the Phase-2 Upgrade. Tech. rep. 2018.

[50] Collaboration, A.L.I.C.E., 2013. Mid-rapidity anti-baryon to baryon ratios in pp collisions at√ s= 0.9, 2.76 and 7 TeV measured by ALICE. arXiv preprint arXiv:1305.1562.

[51] Quigg, C., Reno, M.H. and Walker, T.P., 1986. Interactions of ultrahigh-energy neutrinos. Physical review letters, 57(6), p.774.